INVESTIGATING DIFFERENTIAL ELECTROTAXIS OF GLIOBLASTOMA AND MEDULLOBLASTOMA SPHEROIDAL AGGREGATES

A Dissertation
Presented to
The Academic Faculty

by

Johnathan Gerald Lyon

In Partial Fulfillment
of the Requirements for the Degree
Doctor of Philosophy in the
Wallace H. Coulter Department of Biomedical Engineering

Georgia Institute of Technology
&
Emory University
December 2017

INVESTIGATING DIFFERENTIAL ELECTROTAXIS OF GLIOBLASTOMA AND MEDULLOBLASTOMA SPHEROIDAL AGGREGATES

Approved by:

Dr. Ravi Bellamkonda, Advisor
School of Engineering
Duke University

Dr. Robert Butera
Department of Biomedical Engineering
Georgia Institute of Technology

Dr. Tobey MacDonald
Department of Pediatrics
Emory University

Dr. Mark Prausnitz
School of Chemical & Biomolecular Engineering
Georgia Institute of Technology

Dr. Susan Thomas
School of Mechanical Engineering
Georgia Institute of Technology

Date Approved: October 13, 2017

for alli.

ACKNOWLEDGEMENTS

I have been humbled to receive financial support for my thesis from a few amazing organizations. Thank you to Phil, Cheryl, and Ian Yagoda and all the folks at the Ian's Friends Foundation for their continued support of our efforts to develop new tools for combatting brain tumors. Thank you to Andres Garcia and the faculty/staff of the NIH/NIGMS-sponsored Cell and Tissue Engineering Biotechnology Training Program (T32GM008433) for their support early in my graduate career at Georgia Tech. Also, another big thank you to the Wells family for their support of my research through the J. Norman & Rosalyn Wells fellowship.

The transcriptomic portion of this thesis would not be possible without the contributions of Sheridan Carroll, and Kristin Loomis, who gracefully accepted the many hours of pestering them with all my RNA quandaries and needs. I would also like to thank Shweta Biliya and Dalia Arafat, core scientists at the IBB High Throughput DNA Sequencing and GT Genomics Core, respectively, for their services, shared equipment and expertise.

I have been fortunate to be well led throughout my entire collegiate career. Thank you to all my friends and advisors from UW DXARTS, especially Juan Pampin, Noel Paul and Shawn Brixey. These three gentlemen were especially transformative in turning me into the inquisitive knowledge-sponge I am today. I would also like to thank Yoky Matsuoka for being the first person to take a chance on a young art student who wanted to dive into neuroscience. I would especially like to thank Rajesh Rao & Reinhold

Scherer for giving me my first real taste of biomedical research and enabling my first, albeit small, substantive contributions to the scientific community.

I also want to give thanks for all the behind the scenes work that Kelly Rockwell, Shannon Sullivan, Sean Meehan, Ketki Patil and all the other great GT BME staff have done to realize this thesis. I also want to thank the many undergrads and interns of the Bellamkonda lab for all they have done and continue to do, especially Alexus Clarke (and the amazing ENGAGES program for bringing such talented youth into the fold), and Ajit Vakharia.

I definitely must thank all Bellamkonda lab members, past & present. Especially Nassir Mokarram and Tarun Saxena for being my lab brothers for the entire trip, and Nalini Mehta and Balakrishna Pai for teaching me more about how to do proper science than they probably realize.

I wish to thank those special few who were daring enough to guide me through the last stages of my thesis, my esteemed committee members: Susan Thomas, Mark Prausnitz, Robert Butera, and Tobey MacDonald. I know time together was limited but they have nonetheless given me a lot. Their thoughtfulness and engagement with my research is much appreciated and their help in finally bringing this thesis into fruition is beyond words.

I especially must thank, oh so much, my amazing advisor, Ravi Bellamkonda. This man has put up with my strangeness and stubbornness with aplomb and has been nothing but supportive, insightful and a genuine article. This has been the most formative

experience of my life thus far and it for certain would not have been possible without him.

For their years of unconditional support, I want to thank all my friends back in Seattle (and some scattered abroad). Of particular note, Jared Friend, Vicky Peterson, Scott Carver, and the rest of the Universe of Discourse, have always been there when I was in serious need of a break—and boy, do they break with joy.

I would like to thank my family, who continues to treat me as the same little seven-year-old idiot who sneezed on all the cookies. They are the best family! They keep me feeling humbled, and full of love.

It may seem a bit uncouth, but I also have to thank my dog, Huck. He's done more to manage my thesis-feelings than he has the capacity to know—You're a very good boy.

Lastly, to Alli—the best partner a lad could dream for—I want give the utmost gratitude, for her unending patience, support, love, and for the joy I get in return.

TABLE OF CONTENTS

LIST OF TABLES

LIST OF FIGURES

LIST OF SYMBOLS AND ABBREVIATIONS

2D	Two-dimensional
3D	Three-dimensional
ANOVA	Analysis of variance
cAMP	Cyclic adenosine monophosphate
CCK8	Cell-counting kit 8
dcEF	Direct current electrical field
EGF	Epidermal growth factor
EGFR	Epidermal growth factor receptor
ERK	Extracellular-signal-regulated kinase
FDR	False discovery rate
GBM	Glioblastoma multiforme
GFP	Enhanced green fluorescent protein
GO	Gene ontology
GPCR	G-protein coupled receptor
GSEA	Gene set enrichment analysis
HGF	Hepatocyte growth factor
KEGG	Kyoto encyclopedia of genes and genomes
MAPK	Mitogen-activated protein kinase
MB	Medulloblastoma
MLL	MatLyLu
mRNA	Messenger ribonucleic acid
mTOR	Mechanistic target of rapamycin

NMDAR	N-methyl-D-aspartate receptor
NS	Not significant
PCR	Polymerase chain reaction
PDMS	Polydimethylsiloxane
PI3K	Phosphoinositide 3-kinase
qRT-PCR	Quantitative reverse transcription polymerase chain reaction
RNA	Ribonucleic acid
RNA-SEQ	Ribonucleic acid sequencing
SEM	Standard error of the mean
TGFB	Transforming growth factor beta

SUMMARY

Treatment of brain and nervous system cancers remains a daunting clinical challenge, with one of the most common brain malignancies, glioblastoma, incurring a mere 5% five-year survival rate. In the search for new therapeutic means—specifically, new ways to direct or curb the invasion of brain cancers—we investigate the directed invasion of brain cancer cellular aggregates by an electrical field. This property is known as electrotaxis (or galvanotaxis), and is known to be involved in a variety of endogenous phenomena including tissue development and wound healing, and is purported to be involved in cancer invasion and metastasis. In this study, we explore electrotaxis in the context of brain cancer, and provide new insights into the effect's underlying mechanisms.

Here, we have developed an electrotaxis assay that adapts existing cancer invasion assays and allows us to study electrotaxis on aggregated populations of cells. We characterize glioblastoma and medulloblastoma cell lines in these assays and report on their electrotactic properties. We then investigate the transcriptome for two cell lines that were found to have opposing electrotactic responses, followed by pharmacological inhibition studies to further validate some of our findings. Overall, the hypotheses explored in this work advance our understanding of the pathways that underlie electrotactic sensing and steering and may lead to new means for guiding or managing brain malignancies.

CHAPTER 1. INTRODUCTION

1.1 Brain malignancies remain a critical biomedical challenge

Primary brain and nervous system cancers represent only a small proportion (1.4%) of total cancer incidence, however, these cancers are involved in proportionally twice as many cancer mortalities (2.8%) [Howlader, 2017]. For any given cancer, the mortality rate is on average 38% of incidence and the median overall 5-year survival rate is 65%. For brain cancers these rates are much worse: the mortality rate is 67% overall and the survival rates are 36% for primary and metastic tumors—21% once spread to lymph nodes.

Neuroepithelial tumors represent the largest subcategory of malignant brain tumors, and are the most clinically pressing, as glioblastoma multiforme (GBM), the most common neuropithelial malignancy (46% of cases), bears a mere 5% five-year survival rate [Ostrom, 2015]. Along with mesotheleomia, the Cancer Genome Atlas data suggest that GBM is the least survivable cancer overall (Figure 1).

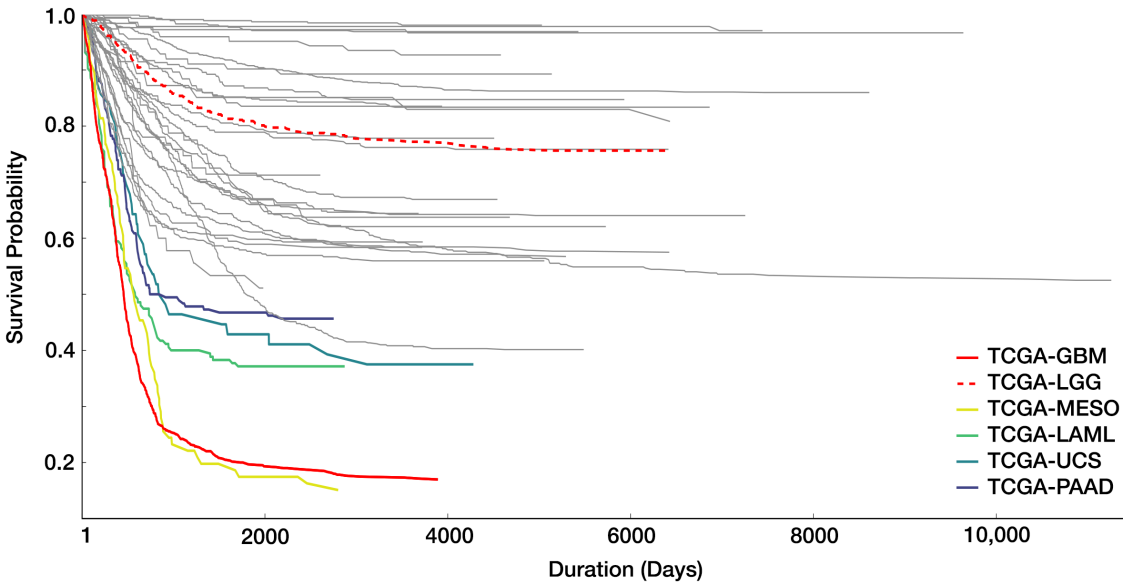

Figure 1. Survival probabilities of various cancer subtypes. Generated from the Cancer Genome Atlas (TCGA) clinical data, downloaded from the National Cancer Institute Genomic Data Commons (portal.gdc.cancer.gov) on September 17, 2017. Depicts survival probabilities including censored data and highlights the two brain cancer TCGA subtypes in red: glioblastoma multiforme (TCGA-GBM), and lower-grade glioma (TCGA-LGG). Also highlighted for comparison are the other lower survival rate cancers: mesothelioma (TCGA-MESO), acute myeloid leukemia (TCGA-LAML), uterine carcinosarcoma (TCGA-UCS), and pancreatic adenocarcinoma (TCGA-PAAD).

Brain tumors are also one of the most prevalent pediatric malignancies, the most common of which, medulloblastoma (MB), is associated with 5-year survival rates as low as 48% [Crawford, 2007; Khanna, 2017]. These dismal survival rates are in part due to a lack of available therapies for cancers in neural tissues, a fact even more daunting when considering that 9-17% of all cancer patients will develop brain metastases [Nayak, 2012].

The current clinical standard of care for brain malignancies is maximally-safe, surgical resection with concomitant fractionated radiotherapy, and chemotherapy

(typically oral Temozolomide and/or implantable Carmustine wafers) [Nabors, 2015]. The brain, however, is a particularly difficult organ to treat, as it is littered with eloquent, inoperable regions. These cancers often disseminate deep into neural tissue, making surgical resection not always possible when the tumor site corresponds to sensitive regions of the brain [Ricard, 2012; Wiesner, 2005]. Even if resection is possible, recurrence is common, due to an inability to completely eradicate all invasive fronts penetrating beyond the primary tumor core [Bernstein, 1995; Belail, 2004]. Systemic administration of chemotherapy is also challenging in the brain, as transport is restricted by physiological barriers to the blood stream and the resulting increased effective doses can be have undesirable effects on sensitive, healthy neural tissues, and can limit indication for geriatric or pediatric patients [Blakeley, 2008].

Even with all the continued advances in drug discovery and delivery that have substantially improved outcomes in systemic cancers, there has been disappointingly little impact on tumors of the brain. Thus, there is an urgent need to innovate new strategies to safely manage or treat brain cancers and therein a substantial need for a better understanding of how brain tumor growth can be limited or controlled—in this work, we will look to electrical fields and their influence on cellular behavior as a means to do so.

1.2 Electrotherapies for cancer

There already exist a variety of electrical means for the treatment of cancer. However, the majority of these techniques do not circumvent the challenges seen with

resection and chemotherapy when applied for the brain. Figure 2 maps out these therapeutic strategies in terms of the field strengths and frequencies used.

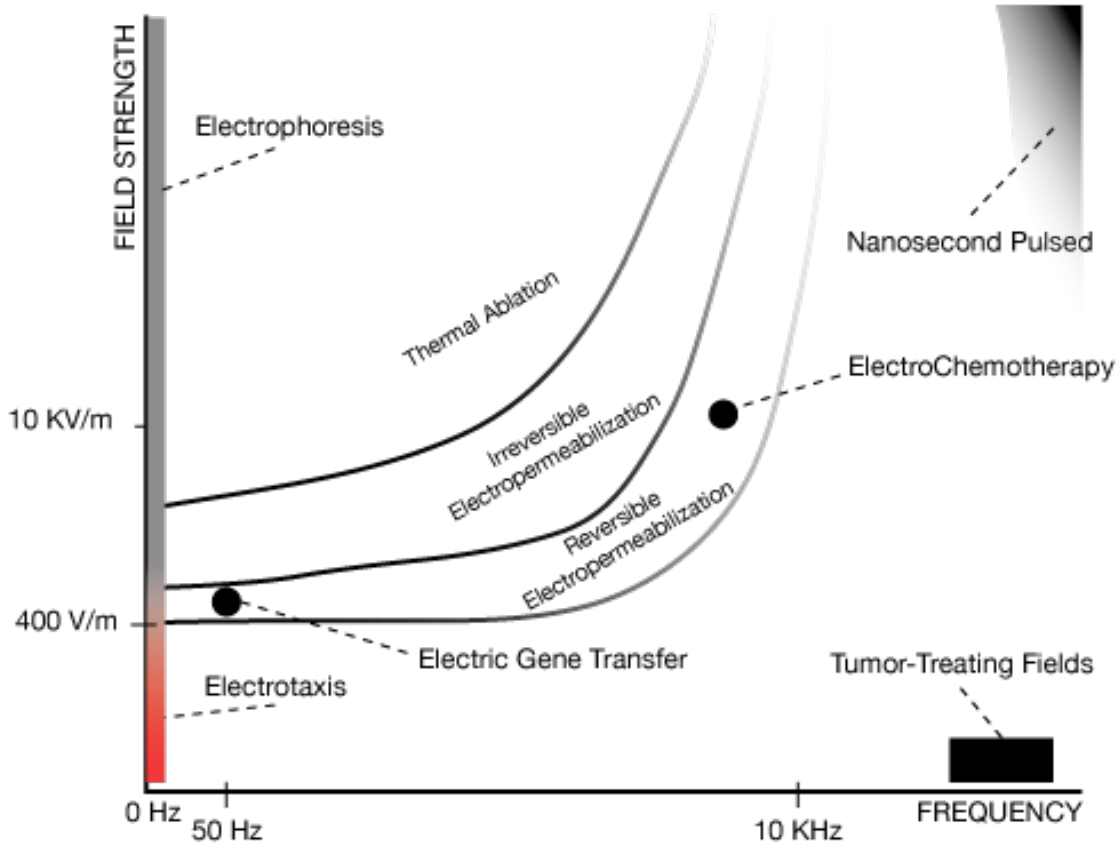

Figure 2. Regimes of electrotherapies for cancer. Adapted from [Marjanovič, 2011].

Thermal radiofrequency ablation works much like surgical resection in that it is used as a physical means of tumor de-bulking [Rossi, 1996]. Typically, two electrodes will be spaced across a tumor region and pulse trains provided with sufficient current to generate Joule heating. Tissue within the heated region is then indiscriminately ablated.

The technique can be applied non-invasively with the use of gold nanoparticles [Cardinal, 2008] yet is limited in the brain by drug delivery barriers and a lack of precision in localizing/imaging tumors non-invasively.

Nanosecond-pulsed electric fields [Nuccitelli, 2006] offer a similar strategy as thermal ablation, but without the thermal effect. Instead it is hypothesized that these fields are cell-penetrable and they create intracellular voltage gradients that disrupt organelle function. While this strategy has seen beneficial outcomes for melanoma, it is relatively unexplored for use in brain cancers, likely due to the same challenges encountered with thermal ablation.

Electropermeabilization (sometimes referenced as electroporation in certain cases) also has found use in cancer therapy. Irreversible electropermeabilization makes use of localized, short duration pulse trains that violently disrupt cell membranes such that the cell is lysed [Davalos, 2005; Gehl, 2003]. This method possesses similar limitations as surgical intervention or targeted radiotherapy in that local access is required, and it can have indiscriminate effects on all tissues between the electrodes. Reversible electropermeabilization also uses localized, short duration pulses that gently permeabilizes or opens pores in the lipid membranes of cells such that the cells are only reversibly permeable. Electrochemotherapy [Gothelf, 2003; Mali, 2013] and electric gene transfer [Cukjati, 2007] are two therapeutic strategies that make use of this reversible regime, wherein the cellular uptake of a therapeutic substrate is enhanced. While these strategies do aid in decreasing the required effective dose of a chemotherapeutic, the requirement that a therapeutic have systemic access to the cells remains, which limits its use for brain cancers.

The cell-electrophoretic range, where the force of the electrical field is large enough to move a cell electro-kinetically, has been recently applied as a means to sort circulating tumor cells for isolation and detection [Shields, 2015]. However, the use of this technique is still experimental for central nervous system malignancies [Adamczyk, 2015] and a therapeutic benefit has yet to be realized.

There exists one clinically available brain tumor electrotherapy, tumor-treating fields, which uses low-power oscillatory electrical fields. The proposed mechanism of action is anti-mitotic; in that the fields are able to penetrate actively dividing cells through the cleavage formed during division, and disrupt the polar molecules involved in spindle formation, thus triggering apoptosis [Kirson, 2007]. The commercial device, know as Optune (formerly NovoTTF-100A) is FDA-approved for use in treating recurrent and newly diagnosed GBM with tandem administration of temozolomide. In a recent phase-III clinical trial (EF-14), Optune was shown to improve median overall survival in newly diagnosed GBM by 2.8 months (to 19.4 mos.) relative to chemotherapy alone (16.6 mos) [Stupp, 2015; Stupp, 2017]. Though, the overall outcomes are still bleak, especially in recurrent GBM where median survival with the device is still only 9.6 mos [Stupp, 2012].

In the regime of low field-strength, non-oscillatory electrical fields, electrotaxis occurs, a regime largely unexplored for cancer therapy, and which is the primary regime focused on in this work.

1.3 Electrotaxis

Electrotaxis (sometimes referred to as galvanotaxis), is the phenomenon whereby application of a low voltage, direct current, electrical field (dcEF) acts as a cue to direct a cell to move of its own volition [Funk, 2006; McCaig, 2009]. The concept of a non-contact force being able to direct a cell's motility is potentially interesting for brain cancer therapy when you consider that controlling invasion (or possibility undoing it) could be a major boon to the management of brain tumors.

Electrotaxis has been observed as an endogenous response to physiologically-generated electric fields (3-500 V/m) occuring during wound healing, neural development, and cancer invasion, as part of the ensemble of simultaneous numerous chemical and physical cues in each process [Borgens, 1981; Mycielska, 2004; Song, 2004; Nuccitelli, 2011; Chernet, 2013].

Upon application of a dcEF, the phenomenon has been observed in myriad cell types, over a range of fields strengths, leading to a variety of cell-type specific responses that as of yet have no generalizeable, unifying mechanism [Cortese, 2014; Liu, 2014].

In cancer research, electrotaxis was first explored as a way to characterize the metastatic potential of cells. Djamgoz, et al., compared two different prostate carcinoma cells lines, confirming a hypothesis that the more metastatic MatLyLu cells would respond to the physiological range of electric fields more strongly than the weakly metastatic AT-2 cells [Djamgoz, 2001]. Presuming the observed cathodally-directed (following the direction of positively charged particles in the dcEF) migration was voltage-gated channel mediated, tetrodotoxin was evaluated for its ability to knockout the

effect, though interestingly, tetrodotoxin only affected the highly metastatic line—the AT-2 cells still moved toward the cathode.

The trend of more metastatic cells having stronger electrotactic response continued with work on metastatic breast cancers. The metatstatic MDA-MB-231 cell line displayed an anodal directionality (following the direction of negatively charged particles in the dcEF), compared with weakly metastatic MCF-7 cells that moved cathodally, albeit slower and with less sensitivity to the dcEF [Fraser, 2005]. This was surprising, as it was unexpected that cells of the same tissue type would have opposing directionality. It was later shown that the electrotactic response in breast cancers appears to correlate epidermal growth factor receptors (EGFR) expression [Pu, 2007]. In particular, with the MDA-MB-231 cells, the response has been linked to the polarization of EGFRs onto the anodal cell membrane, and an increase of intracellular Ca^{2+} [Wu, 2013]. Though it remains unclear what leads to either an anodal or cathodal asymmetry, as it was previously shown that in certain cathodally-electrotaxing cells, EGFR polarization also can occur on the cathodal side [Zhao, 2002].

Human lung cancer cells have also shown similar electrotactic potential in correlation with metastatic potential. Huang, et al., used an electrotactic-sorting microfluidic system to show that metastatic CL1-5 cells respond anodally to a dcEF up to 375 V/m, while the non-metastatic CL1-0 exhibited no electrotactic effect [Huang, 2009].

Primary brain cancer cell have only been used in a few electrotaxis studies, focusing mainly on mechanistic studies. U251 human GBM cells were shown to have a cathodal electrotactic response attributed to a voltage-gated potassium channel and

intracellular polyamines [Nakajima, 2015]. U251, U87mg (human GBM), and C6 (rat glioma) cell lines have also been found to electrotax toward the cathode and it was observed that this stimulated the production of hydrogen peroxide and superoxide [Li, 2013]. It was then shown that superoxide was acting as an upstream regulator of the extracellular-signal-regulated kinase (ERK) and AKT pathways, which is thought to enable the direction persistence in some electrotaxing cells.

Recently, Huang, et al., showed that the direction effect may be further altered by substrate or plating conditions. They tested 5 different brain-tumor-initiating cells plated on poly-L-lysine and laminin substrate, and found that under a dcEF, the cells all responded with a anodal preference, while fetal-derived neural progenitor cells responded cathodally [Huang, 2016]. When these same cells were plated in a 3-dimensional (3D) matrix of hyaluronic acid and collagen, the electrotactic response of the brain-tumor-initiating cells reversed toward the cathode, but the authors presented no further evidence as to why this had occurred.

It remains unclear, given any particular cell, whether it will be electrotactic, or in which direction it will move, and given the startling finding that substrate or plating conditions may dramatically alter the electrotactic response, there is a need for more studies that expand beyond the traditional, short-term, 2-dimensional (2D), single cell format.

CHAPTER 2. ELECTROTACTIC RESPONSES OF GLIOBLASTOMA AND MEDULLOBLASTOMA CELL SPHEROIDAL AGGREGATES

2.1 Introduction

Much of the previous work on electrotaxis has been focused on single-cell responses on 2D substrates, however, when cancerous tissues grow or invade in tissues, they may also do so as a collective or in 3D [Friedl, 2009].

There have been few studies of electrotaxis at population or tissue densities. Babona-Pilipos, et al. studied neurospheres of subependymal neural precursors plated on a 2D substrate, but only analysed cells that had migrated sufficiently far from the rest of the neurosphere cohort [Babona-Pilipos, 2015]. Cohen, et al., developed methods to track individual cells in epithelial sheets of arbitrary geometries, as a way to piece apart the varied electrotactic responses of leader and follow cells [Cohen, 2014]. Lalli & Asthagiri showed, using densely-packed, 2D cultures of mammary epithelial cells that collective migration was more sensitive to dcEF (responding to 50% weaker fields than dispersed cells), yet the resulting electrotactic alignment occurred with slower dynamics [Lalli, 2015].

One limitation to more population studies is that few cells truly form populations in 2D. 3D electrotaxis studies have thus far been limited due to the inherent technical difficulties, but there have been a couple attempts of note. Zhang, et al., showed that dispersed human induced-pluripotent stem cells that were typically stationary in a 3D

matrix, responded cathodally to a physiological-level dcEF [Zhang, 2011]. Zhao, et al., developed a clever, high-throughput method of assaying cells in arrays of 3D agarose droplets with Dictyostelium cells, though this method has yet to be attempted for mammaliam cell culture [Zhao, 2013]. Spheroids have also been used as a 3D format though the studies have not included a 3D substrate and the spheroids have not been assessed for collective migration [Sauer, 2002; Babona-Pilipos, 2015]. Most recently, the above-mentioned study by Huang, et al., on brain-tumor initiating cells that had differing electrotactic responses in 3D and 2D, highlights the need for more studies that take into account experiments more than just 2D, single cell assays.

In this chapter, we began with to study brain tumor cells undergoing electrotaxis in a population-level assay. We have attempted to marry the standard tumor invasion assay (e.g., [Vinci, 2015]) with previous work on standard electrotaxis assays [Song, 2007]. The design principles we chose to build for were: (i) flexible configuration, to allow many potential plating options; (ii) simplicity in fabrication; (iii) capability for long-term (>24h) experiments; and (iv) ability to analyze population-level changes without live-cell microscopy. We were able to develop for these requirements by fashioning systems out of standard 6-well tissue culture plates, with replaceable salt bridges, and simple dcEF sources to allow for constant incubation. Apart from the single-cell tracking experiments, we developed straightforward analytical methods to allow for analysis of population behavior without the need for live-cell imaging. We used these systems to determine how various brain tumor cell lines responded when plated as 3D spheroidal aggregates to dcEFs, as described below.

2.2 Materials & Methods

2.2.1 in vitro cell culture and cell lines

U87mg (human glioblastoma, ATCC HTB-14), DAOY (human medulloblastoma, ATCC HTB-186), and MatLyLu (rat prostate cancer, ATCC JHU-5) cells were obtained from ATCC. D283 Med (human medulloblastoma, ATCC HTB-185), D341 Med (human medulloblastoma, HTB-187), A-172 (human glioblastoma, ATCC CRL-1620), U373 (human glioblastoma, ATCC HTB-17), T98G (human glioblastoma, ATCC CRL-1690), and LN229 (human glioblastoma, ATCC CRL-2611) cells were obtained from the Duke University Cell Culture Facility, all originally sourced from ATCC. All cells were maintained at 37ºC with 5% CO_2 in Dulbecco's Modified Eagle Medium (cellgro 15-017CV) with 10% fetal bovine serum (Gemini 900-108), 1% L-Glutamine (Lonza 17-605F), 1% Non-essential amino acids (cellgro 25-025-CI), and 1% penicillin-streptomycin (Corning 30-001-CI). Cells were passaged before confluence using 0.25% Trypsin-EDTA (gibco 25200-056). As noted for some experiments, U87mg and MatLyLu cells were made to stably express enhanced green fluorescent protein (GFP), via transfection with an GFP-expression plasmid using the Effectene Transfection Reagent (Qiagen 301425) and further selection of stable transfectants with G418 Sulfate (Gemini 400-113).

2.2.2 Construction of electrotaxis chambers

Corning 6-well plates (3516) were used as the basis for the chambers (Figure 3). The center two wells served as the plating region and media reservoirs. The outer four wells served as buffer reservoirs and electrode-electrolyte transition wells. The three

wells of each row were coupled so that two assays could be performed on a single plate. Platinum electrodes (Omega Engineering SPPL-008) were used in an electrolyte bath of phosphate buffered solution (Corning 21-040-CV). Electrodes were held in place by stainless steel alligator clips, fastened into the well-plate lid with silicone sealant (Dow Corning 734) and used for external power-supply connection.

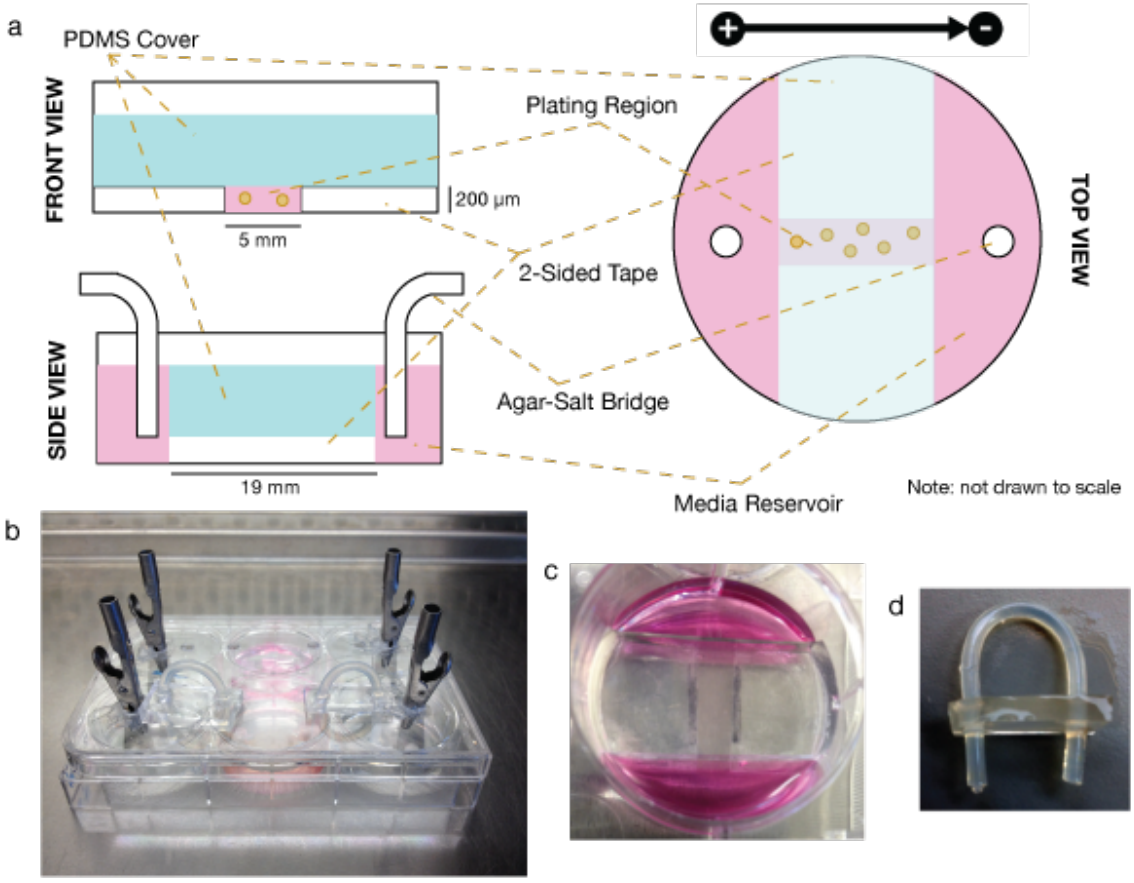

Figure 3. Custom electrotaxis well system. (a) Schematic of electrotaxis channel construction. (b) Completely assemble electrotaxis well system. (c) Photo detail of assembled reservoir and plating channel well. (d) Photo detail of removable agar-salt bridge.

Chambers were connected via agar-salt bridges (Figure 3d) to filter out potentially harmful electrode products. These bridges were comprised of 1/8" silicone tubing (McMaster-Carr 51135K11), filled with 5% autoclaved agar (BD Difco 214530), 1M KCl (VWR BDH0258), and 25 mM HEPES (Sigma, H4034). Polydimethylsiloxane (PDMS) "clips" were used to maintain tube curvature. Pre-fabricated tubes were stored in autoclaved deionized water with 100 mM KCl until use. 1/8" hole were drilled into the lid of the well-plate such that the bridges could be inserted to connect each electrolyte well to the nearest media reservoir.

The plating area was a channel constructed such that the height of the plating area was 202 μm high, 5 mm wide and 19 mm long. Walls of the plating area were built from two layers of double-sided solvent-resistant tape (polyethylene, McMaster-Carr 7602A56), cut to fit the curvature of the well-plate and centered so that there was sufficient space for media reservoir on either end of the plating area channel. The plating area was topped by PDMS (Sylgard 184) strips, made to match the curvature of the well-plate and cut to fit the width of the tape walls. These were made sufficiently high and sealed to the side of the well with autoclaved vacuum grease (Dow Corning, high-vacuum silicone grease) such that the electrical current could only travel through the plating area channel when applied. COMSOL Multiphysics 4.4 was used to simulate current density in the channel using electrolyte conductivity of 1.5 S/m.

2.2.3 Spot assays

5,000 GFP+ cells in 2 μL of media were dropped as 'spots' (Figure 4) into the plating channel and allowed to attach for 15 minutes before addition of PDMS covers and

the rest of the media. Spots were allowed to grow for 24h before application of dcEF. Spots were imaged periodically during dcEF application and images were aligned over multiple time points in Adobe Photoshop using either registration marks made with solvent-resistant markers on the underside of the well, or by unique patterns in the tape edges that line the stimulation channel. Control wells received no dcEF. Images of spots were then intensity-thresholded to a binary mask, and summed across rows and fit to a single-term Gaussian model in Matlab (version R2012b, Mathworks) (Figure 4a). These fits were then segmented across time based on the initial timepoint fit for mean (μ_0) into anodal and cathodal halves. The proportional change of cell area on the cathodal side minus the proportional change on the anodal side was defined as the cathodal shift (Figure 4b) used to express change in population shift over time relative to the alignment of the dcEF.

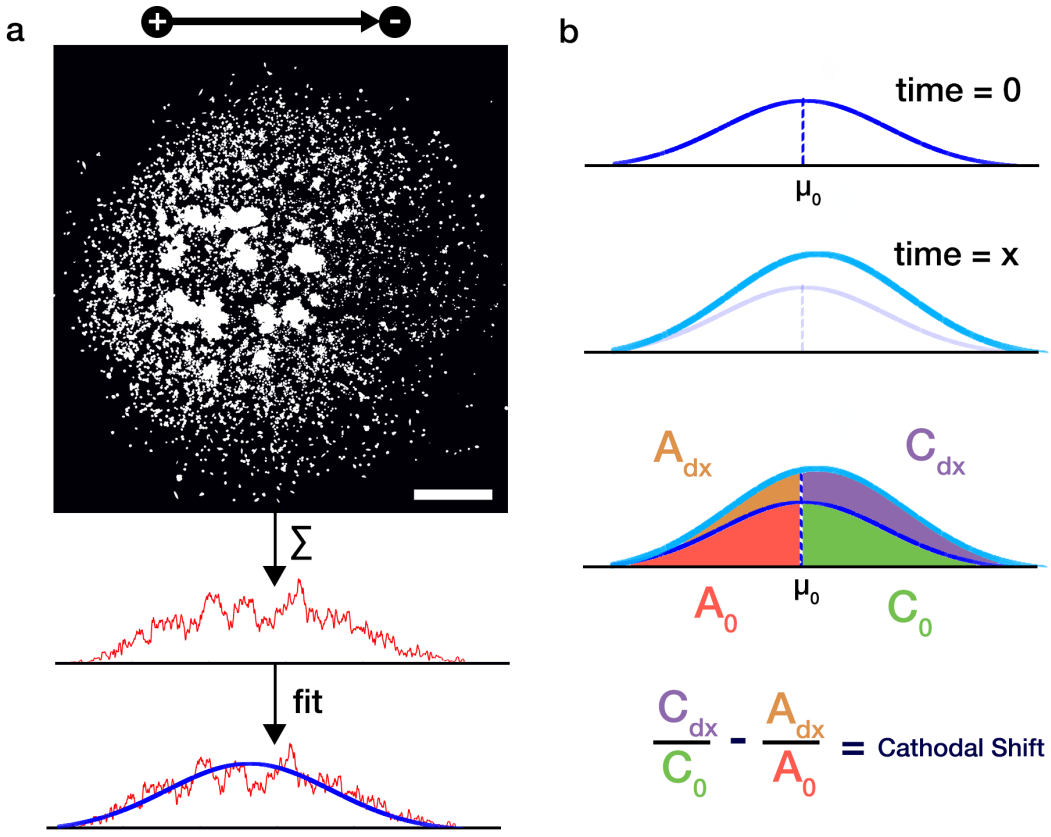

Figure 4. Spot assay analysis. (a) Thresholded, binary mask of GFP+ MatLyLu cells plated as a spot are summed across rows and then fit to a Gaussian curve. Scale: 200 μm. (b) Gaussian fits are then taken across time and segmented relative to the initial mean of the fit (μ_0) and these proportional changes in summed cell area on either side are used to determine the amount of cathodal shift.

2.2.4 Preparation of spheroidal cell aggregates

A microwell-based method was used for producing spheroidal aggregates. PDMS reverse molds were made from Aggrewell 400Ex (StemCell Technologies 27840). These were used to cast 3% autoclaved Agar (BD Difco 214530) versions of the original Aggrewells. The agar versions were placed in 6-well plates and sterilized under ultra-violet light before use. Cells were counted and diluted to either 700,000 or 1,400,000

cells per 3 mL—unless otherwise specified—and transferred in 3 mL volume to each well. Plates were centrifuged for 4 min at 280 x g and then transferred to 37ºC, 5% CO_2 and left for 24 hours to grow before experimental use.

Aggregates were aspirated from the plates and added to electraxis channels with a 1:1 ratio of aggregates/media to Growth-Factor-Reduced Matrigel (Corning #354230) in 30 μL total volume (note: Matrigel batches were kept consistent within each set of experiments). The solution was allowed to solidify for 30 minutes before media reservoirs were filled. Cells were given 24h to acclimate to 3D conditions before application of electrical fields.

2.2.5 Application of electrical fields

Electrical fields were applied to each of the alligator clips on the electrotaxis chambers via a simple series circuit of 27 V battery supply, and a 1MΩ potentiometer. Current through the system was measured with a digital multi-meter, as the potentiometer was adjusted in order to provide the desired field strength as calculated by Ohm's law in this form:

$$I_{set} = E * \sigma * A$$

Where: E is the desired field strength (in V/m); σ is the conductivity of the media (in S/m; set to 1.5 S/m for all included studies); A is the cross-sectional area of the electrotaxis channel, orthogonal to the flow of current (in m); and I_{set} is the set current measured by the multimeter (in A).

During ongoing stimulation, periodic checks are made: (i) to ensure set currents have remained consistent (note: in this study, we kept currents within ranges that would indicate a ±20 V/m per 4h drift in field strength)—experiments that do not meet this criteria are excluded from further analysis; (ii) to reset I_{set} to desired value; (iii) to replace media if any visually-detectable (by phenol red) pH shift gradient has formed; and (iv) to replace salt-bridges. The determination of this check period duration is done by small pilot studies for each experiment and depends mainly on the amount of current applied.

2.2.6 Microscopy

Images in sections 2.2-2.3.6 were taken with a Zeiss Axiovert 200 using Microlucida (v2.50.2a, MBF Bioscience) and for sections 2.3.7-2.3.8 we used a Leica DMi8 with Leica Application Suite X tile scan. Plates were all aligned in the microscope such that the anodal side (direction toward positive battery terminus) is to the left of the image. Z plane focus was set to the middle depth of the channel.

2.2.7 Single cell analysis

Single cell experiments were imaged under temperature control for up to 4h. Images were analysis using the manual-tracking tool in ImageJ (FIJI). Displacement toward the cathode was calculated by taking the scalar projection ($|A| \cos \theta$) of each segment length ($|A|$) where θ is the angle between cell's path vector (A) and the electrical field line aligned toward the cathode ($y=0$ for $x>0$). Displacement magnitudes are then normalized by the duration between the initial and final time points for each segment and reported as an average of all segments for a given cell.

2.2.8 Spheroidal analysis

Tiled images of plating channels containing spheroidal aggregates were taking before and during each experiment. Tiled imaged were re-aligned across multiple time points in Adobe Photoshop using either registration marks made with solvent-resistant markers on the underside of the well, or by unique patterns in the tape edges that line the stimulation channel. Control wells received no dcEF. Individual aggregrates were selected from the tiled images and cropped for further analysis. A conservative frontier-based method was used for determining the extent of each aggregrate (Figure 5) and demarcated for each of four directions relative to the alignment of the dcEF (Figure 5d). The absolute outward shift of each frontier over time is reported for each aggregate. Cathodal bias is defined as the outward shift of the cathodal frontier minus the outward shift of the anodal frontier. Similarly, the orthogonal bias is the outward shift of the orthogonal minus the orthogonal' frontiers.

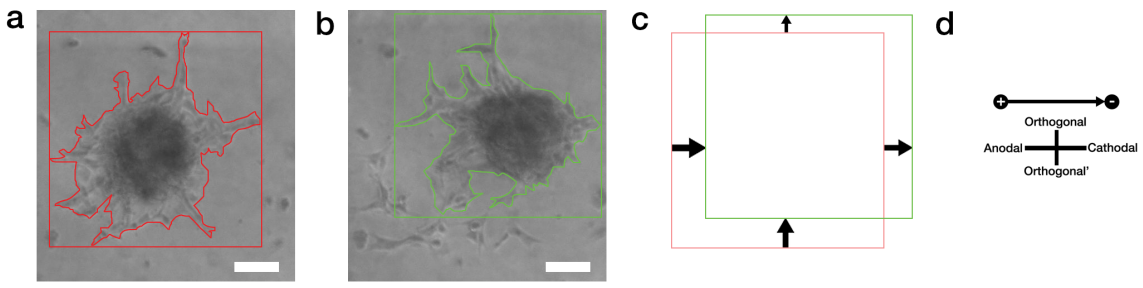

Figure 5. Definition of frontier bounding boxes. Frontiers are defined using the maximal extent of each spheroidal aggregate (a & b) in one of four directions as defined in (d). The signed magnitude of outward change (c) in frontier from one time point to the next is used to report change in the aggregates. Scale: 100 μm.

The bounding box formed from the frontiers is also used for reporting size of the aggregates as they change over time; these are normalized to the size of the initial frontier bounding box at time=0 and reported as a proportional change in area. Linear regressions of the initial aggregate area versus the cathodal bias were done with Prism 7 (Graphpad Inc.).

2.2.9 Graphing and statistics

All graphs and statistics analysis were done with Python (v2.7.x, Python Software Foundation, Anaconda Distribution) or Prism 7 (Graphpad Inc.) unless otherwise specified. The statistical methods used are reported for each result, in place. α=0.05 unless otherwise specified.

2.3 Results & Discussion

2.3.1 Electrotaxis chamber validation with MatLyLu cells

Our newly designed electrotaxis chambers were first validated computationally, using COMSOL Multiphysics, to verify that a consistent current density would be applied within the plating channel (Figure 6a). Subsequently, we were able to reproduce previous results using the MatLyLu cell line that is known to electrotax toward a cathode [Djamgoz, 2001]. We were able to show results similar to those found in Djamgoz, et al., such that after 2h of exposure to a 100 V/m electrical field, MatLyLu cells moved over twice as much as unexposed cells. The control cells also had only a small net displacement (3.95±3.86 μm) compared to exposed cells that were significantly more attracted to the cathode (26.11±11.75 μm). Further, comparison of the net, field-orthogonal displacement, which should not be affected by an electrical field, resulted in no significant difference.

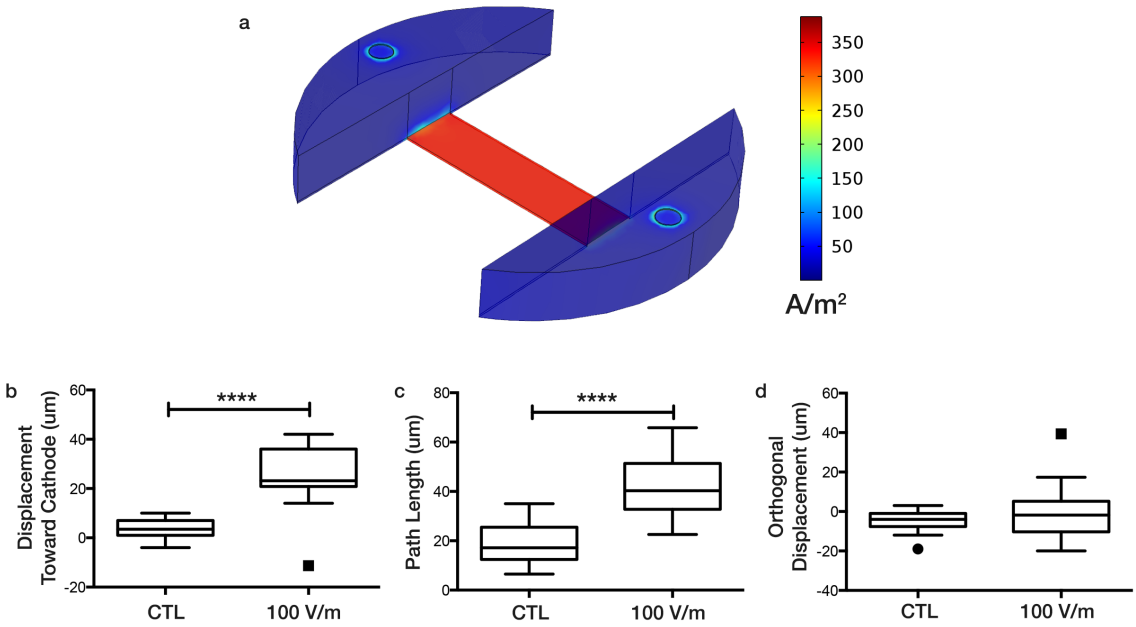

Figure 6. Validation of electrotaxis chamber wells. (a) COMSOL simulation of electrotaxis chamber wells with I_{set} = 330 µA. (b, c & d) MatLyLu single cell tracking results in electrotaxis chamber wells for single cells tracked over two hours for both no electrical field (CTL, n=20) and stimulation equivalent to 100 V/m (n=22) for: (b) displacement along the electrical field lines toward the cathode; (c) total path length traveled, regardless of directionality; and (d) displacement along the axis orthogonal to the electrical field. ****$p < 0.0001$ by Student's t-test.

2.3.2 U87mg cells have mixed electrotactic response at population densities

Our first attempt to perform electrotaxis at population densities was to run spot assays as 2-dimensional models of tumor invasion using one of most widely studied GBM cell lines, U87mg. We hypothesized that electrotaxis would distort the radial outward growth from the initial spot in a way that would mirror a collective cell response to a signaling gradient. Over 48h our positive control MatLyLu spots developed a detectable difference in positive cathodal shift under dcEF, however, the U87mg cells did not exhibit a bias in directionality with the application of dcEF (Figure 7a). Under

further inspection, we noticed that while the global Gaussian envelope did not bias over time for the dcEF+ U87mg spots, certain regions of the cell-area profile displayed marked shifts, locally. At later time points, the U87mg cells began to coalesce into 3D aggregates in both dcEF and control conditions when regions of the spot became over-confluent. These 3D aggregates appeared to elicit a directional response toward the cathode in a dcEF (Figure 7c) whereas control aggregates had unbiased outward growth over time (Figure 7b).

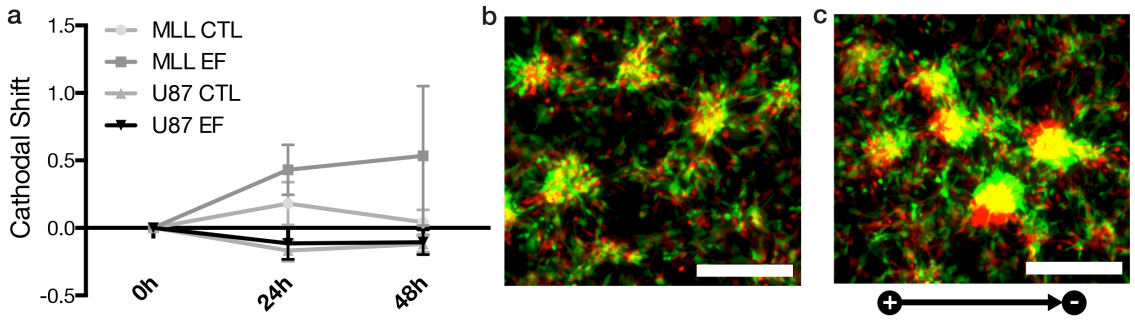

Figure 7. Spot assays undergoing electrotaxis. (a) Cathodal shift of GFP+ MatLyLu (MLL) or U87mg (U87) cells exposed to 100 V/m dcEF (EF) of no dcEF (CTL) for 48h. Mean ± standard error of the mean (SEM) shown. (b & c) Detail of GFP+ U87mg spot assays were 3D aggregates have formed. Pseudocolored for time=0h (red) and time = 8h (green) for no dcEF (b) and 100 V/m (c). Scale: 400 μm.

2.3.3 U87mg cells do not exhibit electrotaxis at single-cell densities

We next performed a series of experiments in order to separate the 2D and 3D aggregate aspects of the spot assays. We first performed a series of single cell tracking

experiments with U87mg cells dispersed in 2D (Figure 8a) or embedded, but dispersed in 3D matrigel (Figure 8b). We observed no electrotactic bias even with a 300 V/m field in 2D. This was surprising as it conflicts with what was previously seen for U87mg cells [Li, 2013], though Huang, et al., have also described similar null results with U87mg cells, noting that these cells did not elicit an electrotactic effect under dcEFs smaller than 600 V/m. At the time, however, we wondered whether this was a result of cell plating density or interference of our particular serum additives. Thus we performed single-cell tracking experiments at 100 and 300 V/m altering the plating density in each spot and also using different media formulations (serum-free, 1% FBS, and 1:100 and 1:200 ratios of matrigel to complete media), yet none of these conditions had significant effect on electrotactic response (Figure 8c). Based on our experiments we conclude that in dcEF below 300 V/m, that U87mg cells do not exhibit electrotaxis.

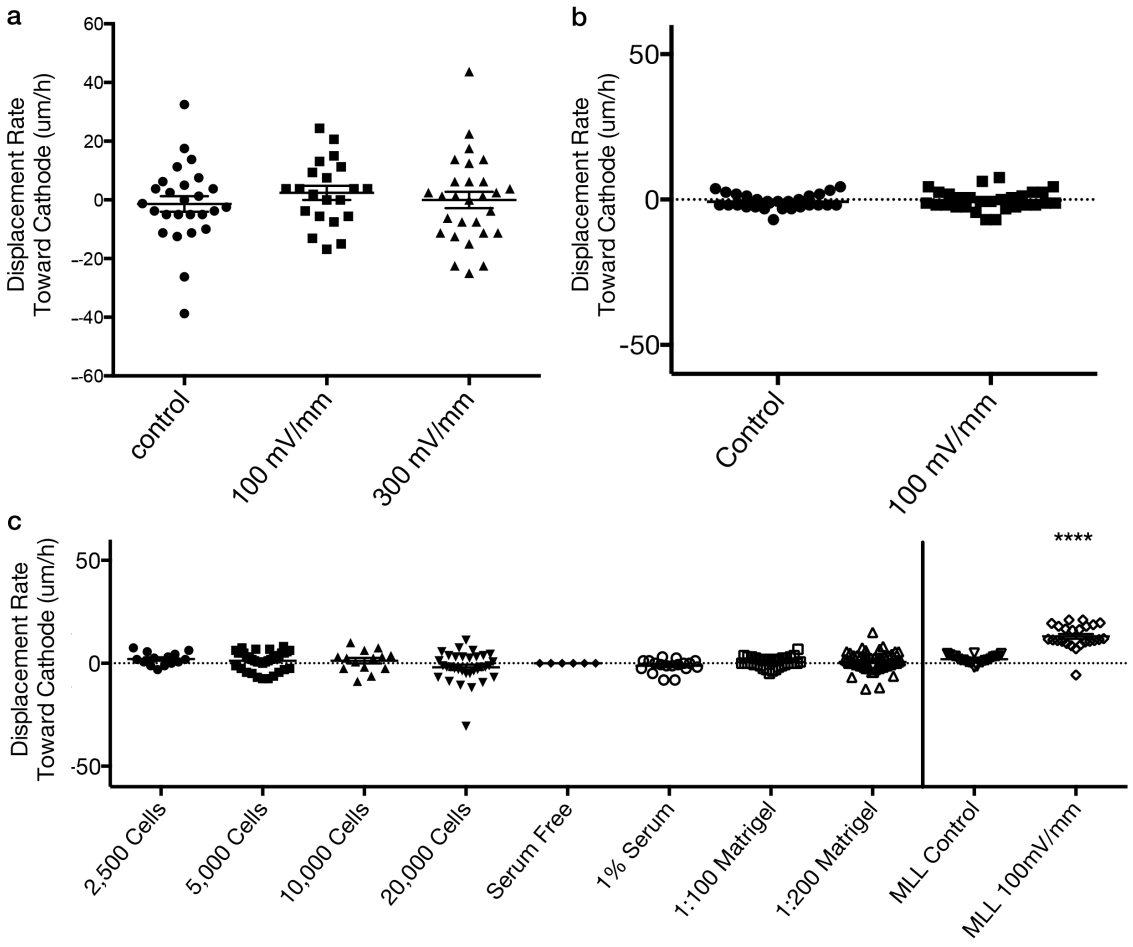

Figure 8. U87mg cells in single cell format do not exhibit electrotactic bias. U87mg cell were plated as dispersed 2D (a) or 3D (b) cells and exposed to dcEFs although exhibited no electrotactic bias relative to controls without dcEF. No statistically significant difference detected in (a) by One-way ANOVA with Holm-Sidak post-hoc test, nor in (b) by Student's t-test. (c) Alterations in plating density (in 5 μL spots) or media formulation also did not elicit an electrotaxis effect. MatLyLu (MLL) single cell controls re-display from FIGURE 2.3.1 for direct comparison. No significant difference other than MLL 100 V/m relative to all other conditions by One-way ANOVA with Holm-Sidak post-hoc test (**** $p < 0.0001$). Mean±SEM shown.

2.3.4 U87mg spheroidal aggregates invade cathodally in dcEFs

To further explore the electrotactic behavior that we observed in our over-confluent spot assays, we used the Aggrewell method to plate isolated spheroidal aggregates in our electrotaxis wells. These aggregates, embedded in a 3D matrix of matrigel, matched the overall response of the aggregates in our spot assays, moving with a cathodal bias under dcEF exposure (Figure 9a,b). After only 8h a significant difference was detected in terms of both the cathodal frontier (for 250 V/m dcEF relative to control, $p=0.0142$) and the overall cathodal bias (for both 100 and 250 V/m dcEF conditions relative to control, $p=0.0448$ and $p<0.0001$ respectively) (Figure 9c) showing a mean cathodal bias of 68±16μm for 250 V/m, for 100 V/m, 37±20μm and 6±12μm for controls (mean±SEM). The cathodal bias for 100 V/m and 250 V/m were also found to be significantly different from each other ($p = 0.0448$). The anodal frontier was not significantly different, though the mean response did decrease with increased voltage. However, what the conservative bounding box method cannot capture is that the bulk of the aggregate has shifted while leaving behind trailing pseudopodia or immobile cells that are included when we demarcate frontiers. The proportional change in spheroid area, as indicated by the size of the frontier bounding box, was slightly, but significantly increased with 100 V/m dcEF ($p=0.0242$), but not discernably different for 250 V/m dcEF relative to control. Using 24h data from later experiments we also found that the initial spheroid area was not a significant factor ($R^2 = 0.00037$, not different than slope of 0, $p=0.8879$) in determining the resulting cathodal bias.

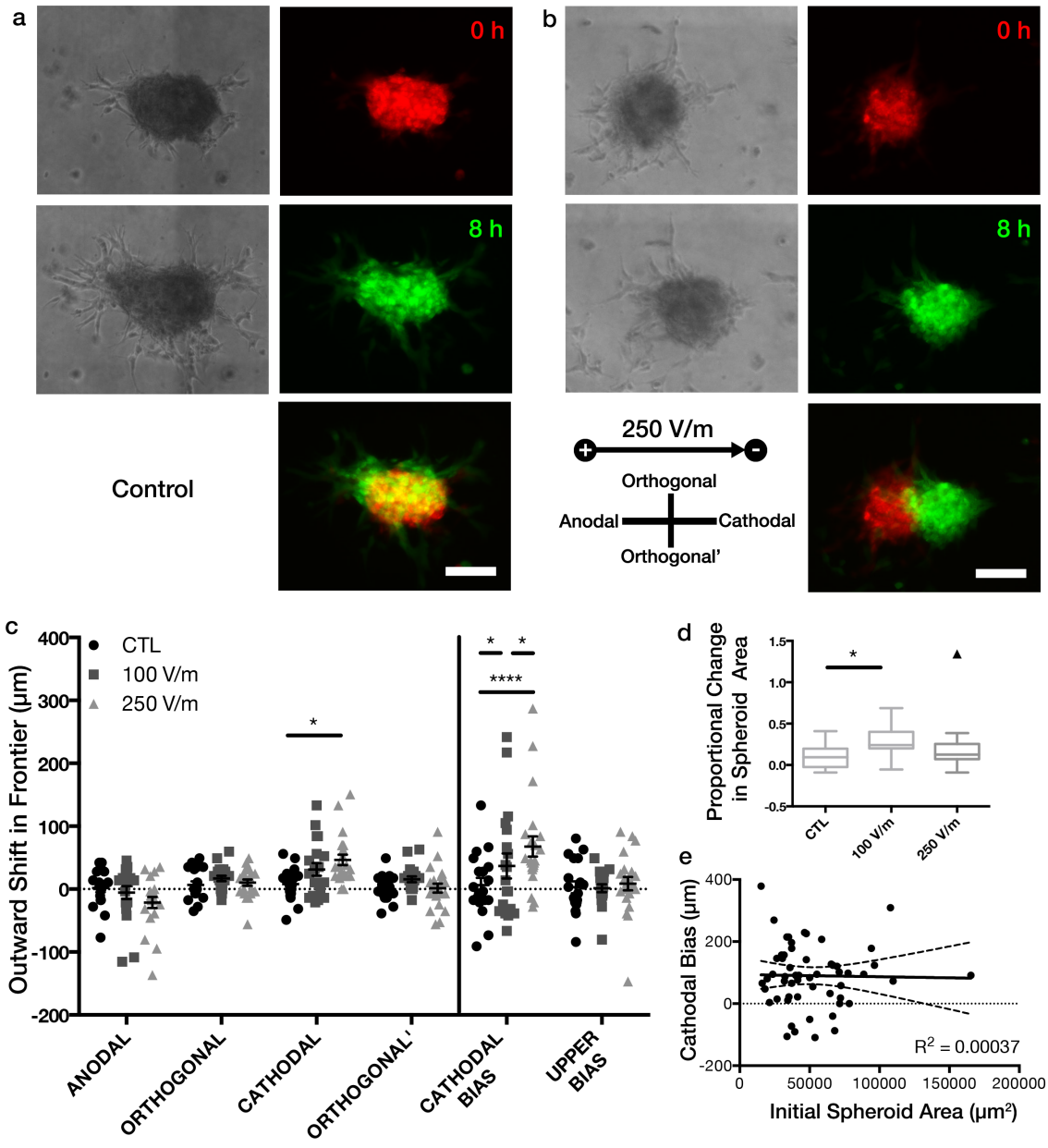

Figure 9. U87mg spheroidal aggregates exhibit cathodal electrotaxis. (a) GFP+ U87mg control aggregates showing no bias in growth direction after 8h. (b) GFP+ U87mg aggregates exposed to 250 V/m dcEF exhibiting cathodal bias, detectable within 8h. (a & b) are pseudo-colored for time=0 (red), time =8h (green). (c) Quantitative assessment of the outward shift of aggregate frontiers after 8h. For cathodal frontier: *p=0.0142; for cathodal bias: *p=0.0448, ****p<0.0001; by Two-way ANOVA and Holm-Sidak post-hoc test. Mean±SEM shown. (d) Proportional change in spheroid area from time=0 to time=8. *p=0.0242, with One-way ANOVA and Holm-Sidak post-hoc test. Mean±Tukey box plots shown. (e) Linear regression of initial spheroid area versus cathodal bias after 8h stimulation with 250 V/m dcEF. R^2=0.00037, not different than slope of 0 with p=0.8879. Scale: 150µm.

2.3.5 DAOY spheroidal aggregates electrotax anodally in dcEFs

We next applied the same spheroidal aggregate procedure to a commonly used cell line model of human MB, DAOY. After just 8h of 250 V/m dcEF exposure, these aggregates exhibited a significant ($p<0.0001$) difference in cathodal bias, yet unlike the U87mg cells, the movement was toward the anode (-69±12μm) relative to controls (-9±8μm) (Figure 10a). For the DAOY aggregates, the outward movement of the anodal frontier (34±9μm) was larger, but not statistically different than in the controls (20±9μm), however the outward growth of the cathodal frontier was (-35±10μm relative to 11±5μm in controls). This suggests that there may be stronger sensing, or perhaps a repulsive effect, of the dcEF at the trailing end of the DAOY aggregates. The bulk of the cathodal bias in the U87mg aggregates came from the change in the cathodal frontier as well, but with a different polarity of response. Like the U87mg counterparts, the DAOY cells did not exhibit a proportional change in overall area (Figure 10b), nor did the initial spheroid area correlate with cathodal bias (Figure 10c).

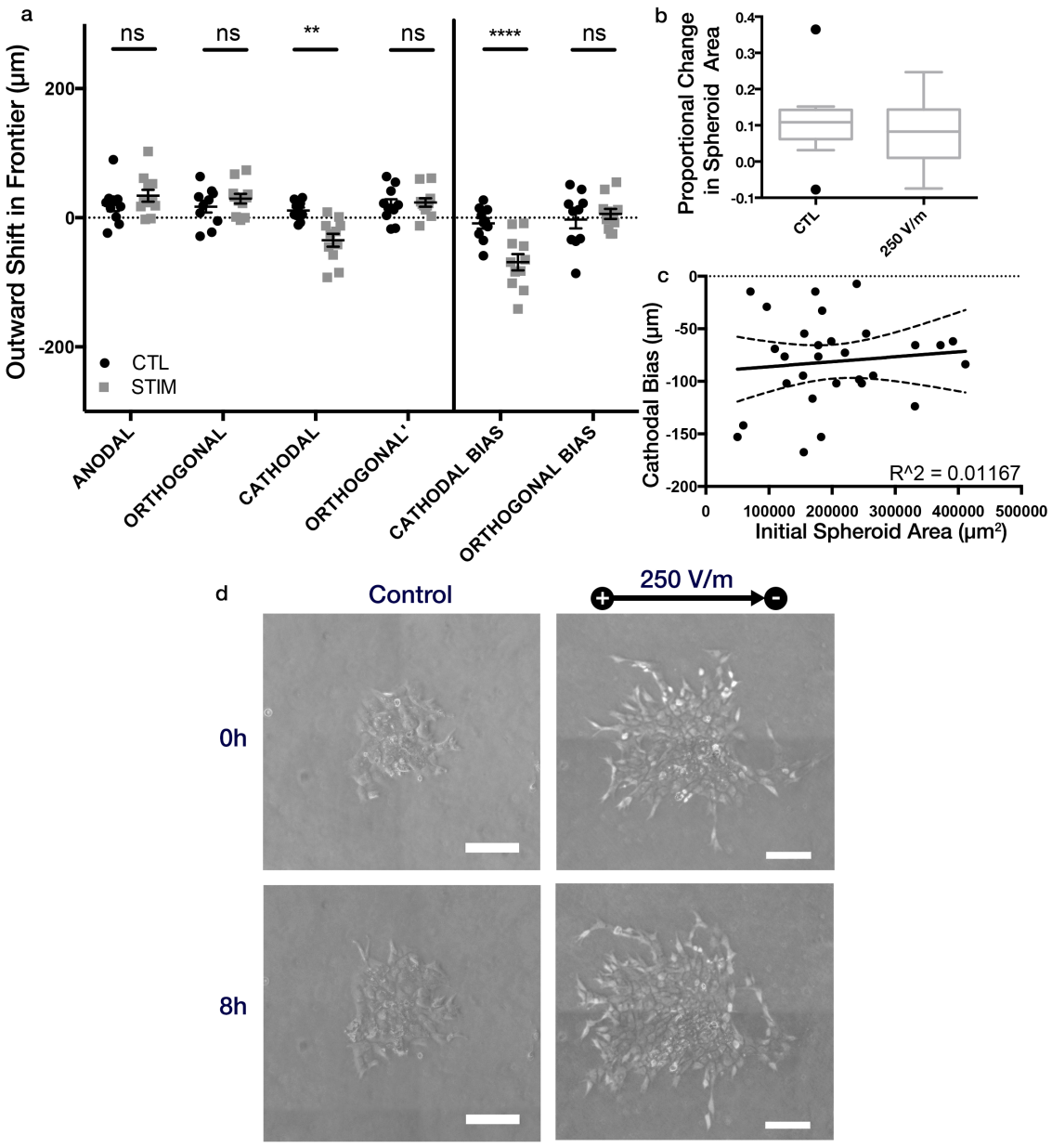

Figure 10. DAOY spheroidal aggregates exhibit anodal electrotaxis. (a) Quantitative assessment of the outward shift of aggregate frontiers after 8h. **p=0.0032; ****p<0.0001; by Two-way ANOVA and Holm-Sidak post-hoc test. Mean±SEM shown. (b) Proportional change in spheroid area from time=0 to time=8. Not significant (p=0.1706) by One-way ANOVA and Holm-Sidak post-hoc test. Mean±Tukey box plots shown. (c) Linear regression of initial spheroid area versus cathodal bias after 8h stimulation with 250 V/m dcEF. R^2=0.01167, not different than slope of 0 with p=0.5770. (d) Example spheroid morphology before and after experiment, with and without 250 V/m dcEF. Scale: 200µm.

2.3.6 24h electrotaxis of additional GBM and MB spheroidal aggregates

In addition to the U87mg and DAOY cell lines, we tested a few other GBM and MB models as spheroidal aggregates for their electrotactic responses. These experiments were done over 24h, rather than 8h and thus we have also provided 24h data for the U87mg and DAOY aggregates as well that were obtained during the experiments presented in Chapter 4 (Figure 11). After 24h of dcEF there are some marked difference to our 8h stimulations. U87mg aggregates still show a significant difference in both cathodal frontier shift ($p=0.0002$) and cathodal bias ($p<0.0001$) relative to controls (Figure 11a). Though, the mean cathodal bias of the U87mg aggregates undergoing electrotaxis does not scale linearly with time from the 8h to 24h data (only 1.32x farther over 3x longer duration), it does increase to 90±14μm after 24h relative to controls -6±20μm. The area of the U87mg aggregates is, after 24h, significantly larger than the control ($p=0.0133$) seen as an elongation parallel to the dcEF field lines (Figure 11c,e).

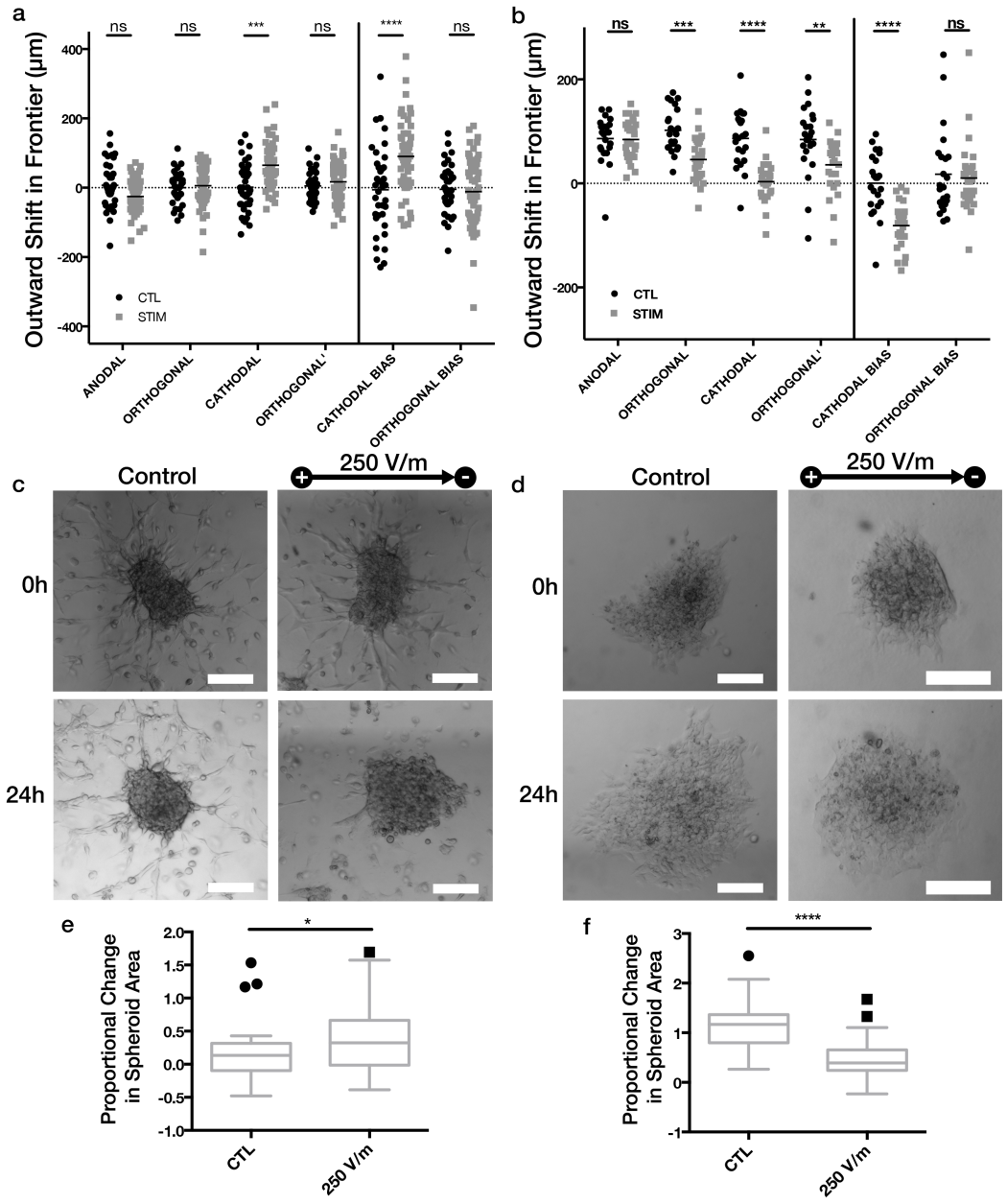

Figure 11. U87mg and DAOY spheroidal aggregates after 24h dcEF exposure. (a & b) Quantitative assessment of the outward shift of aggregate frontiers after 24h for (a) U87mg, and (b) DAOY spheroidal aggregates with 250 V/m dcEF (STIM) or no dcEF (CTL). **p=0.0032; ***p=0.002 for (a), p=0.0007 for (b); ****p<0.0001; by Two-way ANOVA and Holm-Sidak post-hoc test. Mean±SEM shown. (c & d) Example spheroid morphology before and after experiment, with and without 250 V/m dcEF for (c) U87mg, and (d) DAOY spheroidal aggregates. Scale: 200 µm. (e & f) Proportional change in spheroid area from time=0 to time=8 for (e) U87mg, and (f) DAOY spheroidal aggregates. *p=0.0133; ****p<0.0001; by One-way ANOVA and Holm-Sidak post-hoc test. Mean±Tukey box plots shown.

The DAOY aggregates, after 24h, again exhibit a significant difference in the cathodal frontier ($p<0.0001$) but not the anodal frontier, and maintain their anodal bias under dcEF (-81±8μm relative to 0±12μm in control, $p<0.0001$). For these cells, the cathodal bias is also greater than in the 8h case, though this is also less than would be expected for linear scaling over time (2.3x farther over 3x longer duration). One major difference to the 8h experiments is that the DAOY aggregrates now exhibit significant retraction in the orthogonal frontiers ($p=0.0032$ for orthogonal, $p<0.0001$ for orthogonal'), which results in a significantly smaller spheroidal area after 24h ($p<0.0001$) (Figure 11f).

2.3.6.1 A172, LN229, T98G, and U373 GBM cell lines undergo anodal electrotaxis

We tested the electrotactic response of four additional human GBM cell lines under a 250 V/m dcEF for 24h. To our surprise, all of these additional lines exhibited electrotaxis, but unlike the U87mg cells, bias was toward the anode. The matrigel batch used for these experiments was different than previous studies, although U87mg tandem controls still showed a cathodal response.

The A172 cells (Figure 12) underwent electrotaxis similar to the DAOY cells, in that there was a significant decrease in outward growth on the cathodal edge ($p=0.0005$), but not the anodal. However, the A172 anodal bias (-181±34μm, mean±SEM), which was significantly greater in magnitude under 250 V/m dcEF than the controls (-22±17μm, $p<0.0001$), was double that seen for DAOY cells. A slight, but not statistically significant decrease in spheroidal area was observed, and again spheroid size was not significantly related to cathodal bias.

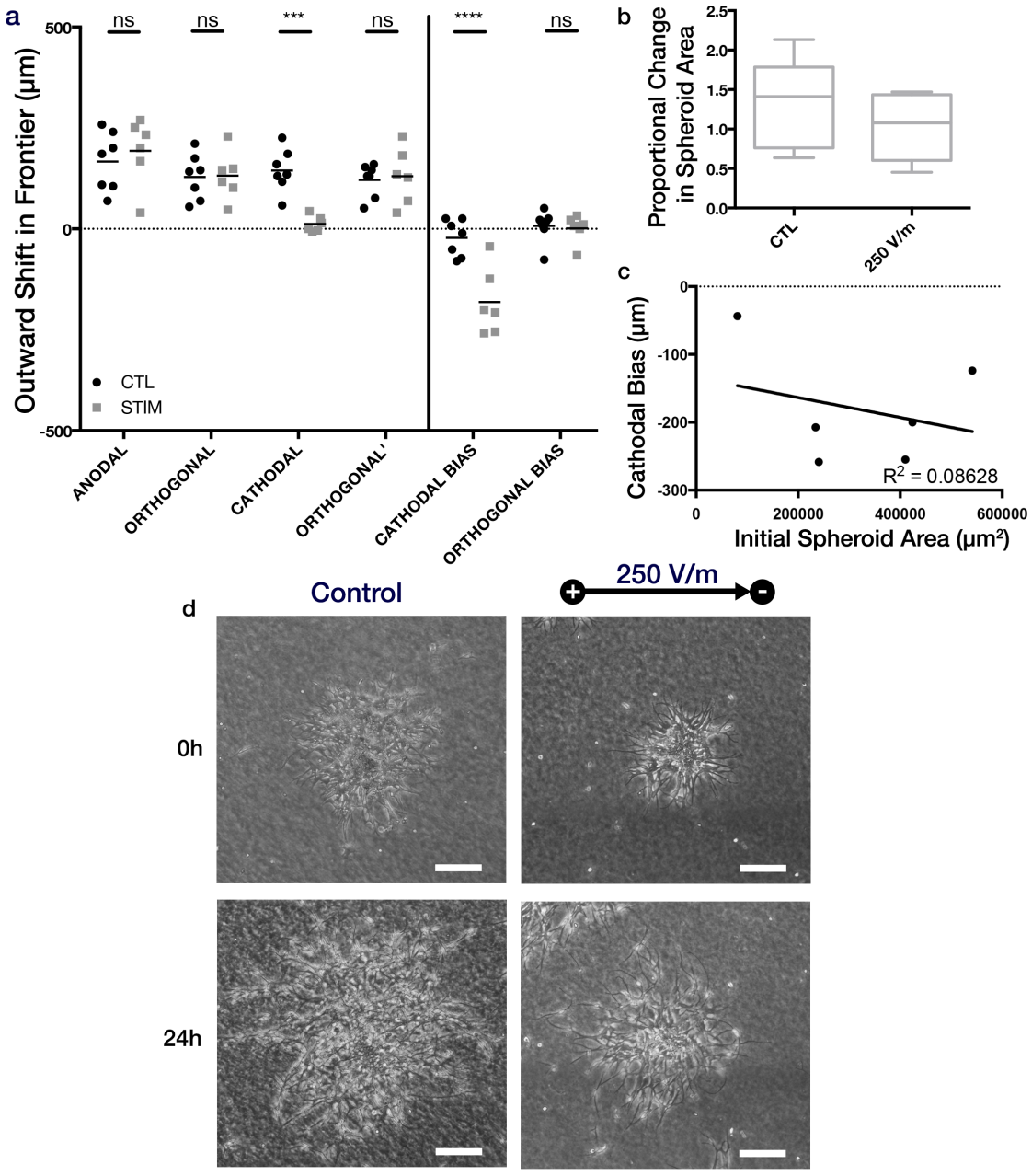

Figure 12. A172 aggregates undergo anodal electrotaxis. (a) Quantitative assessment of the outward shift of A172 aggregate frontiers after 24h. ***p=0.0005; ****p<0.0001; by Two-way ANOVA and Holm-Sidak post-hoc test. Mean±SEM shown. (b) Proportional change in spheroid area from time=0 to time=24. Not significant (p=0.3351) by One-way ANOVA and Holm-Sidak post-hoc test. Mean±Tukey box plots shown. (c) Linear regression of initial spheroid area versus cathodal bias after 24h stimulation with 250 V/m dcEF. R^2=0.08628, not different than slope of 0 with p=0.5721. (d) Example A172 spheroid morphology before and after experiment, with and without 250 V/m dcEF. Scale: 200µm.

LN229 cells (Figure 13) also exhibited a strong anodal bias (-127±15μm, mean±SEM), significantly different than controls (-14±734μm, $p<0.0001$), and a significant decrease in cathodal frontier growth ($p<0.0001$). However, the LN229 aggregates also exhibited a significant increase in outward shift of the leading, anodal frontier (p-0.0074). The LN229 cells also exhibited a greater, but still not significant decrease in spheroid bounding box area, and showed weak correspondence between the cathodal bias and the initial spheroid area.

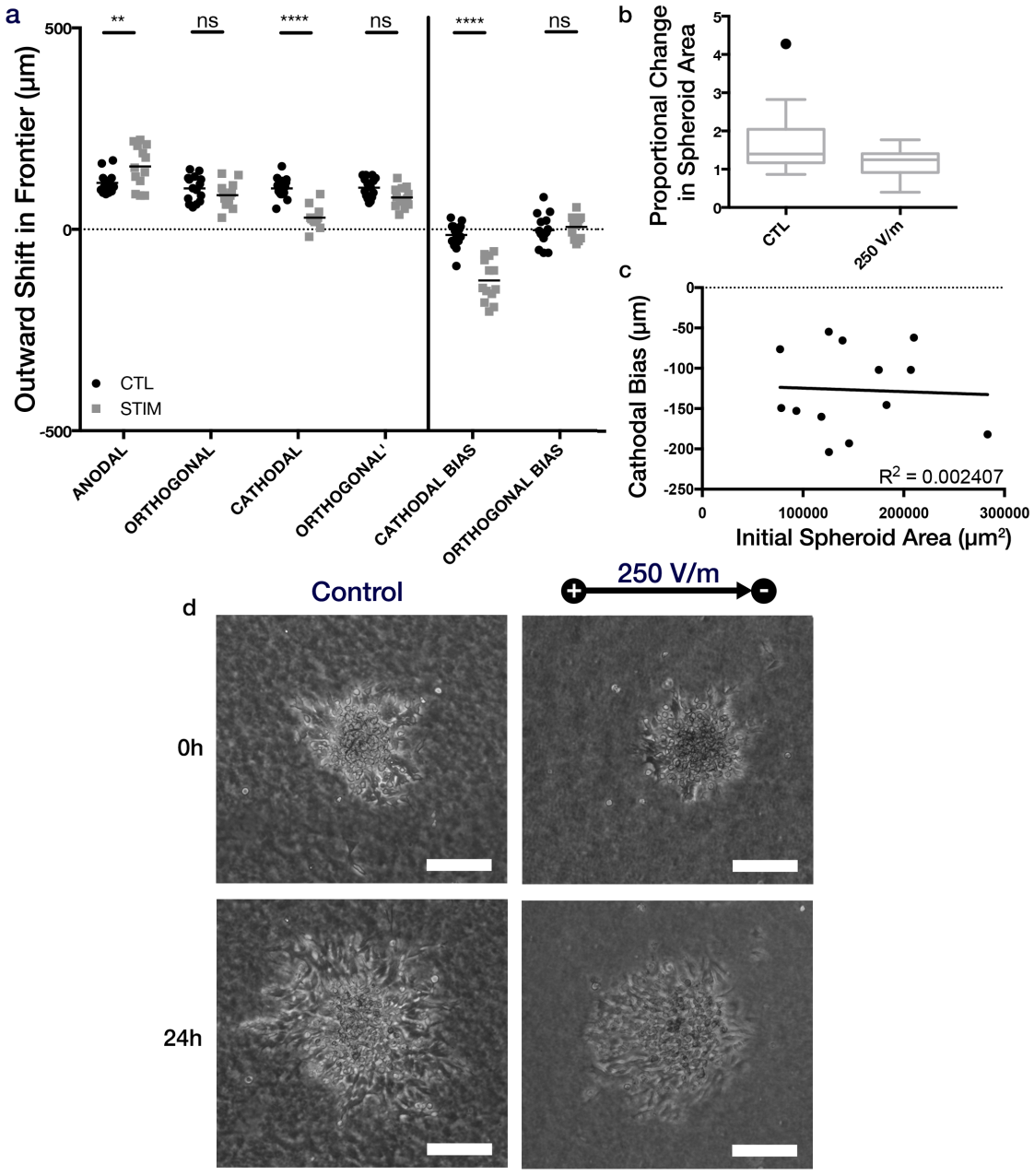

Figure 13. LN229 aggregates undergo anodal electrotaxis. (a) Quantitative assessment of the outward shift of LN229 aggregate frontiers after 24h. **p=0.0074; ****p<0.0001; by Two-way ANOVA and Holm-Sidak post-hoc test. Mean±SEM shown. (b) Proportional change in spheroid area from time=0 to time=24. Not significant (p=0.0526) by One-way ANOVA and Holm-Sidak post-hoc test. Mean±Tukey box plots shown. (c) Linear regression of initial spheroid area versus cathodal bias after 24h stimulation with 250 V/m dcEF. R^2=0.002407, not different than slope of 0 with p=0.8736. (d) Example LN229 spheroid morphology before and after experiment, with and without 250 V/m dcEF. Scale: 200µm.

T98G aggregates (Figure 14) exhibited an even stronger anodal bias (-194±8 μm, $p<0.0001$ relative to controls with -36±11 μm), with the lowest variability of all tested lines. The T98G anodal frontiers were also significantly different than controls ($p=0.0104$), but the effect seen was not a greater growth than the maximum seen in controls, but more consistently maximal. This consistency also impacted the efficiency of the electrotactic response, as the whole spheroid moved together and displayed no significant change in bounding box area over time.

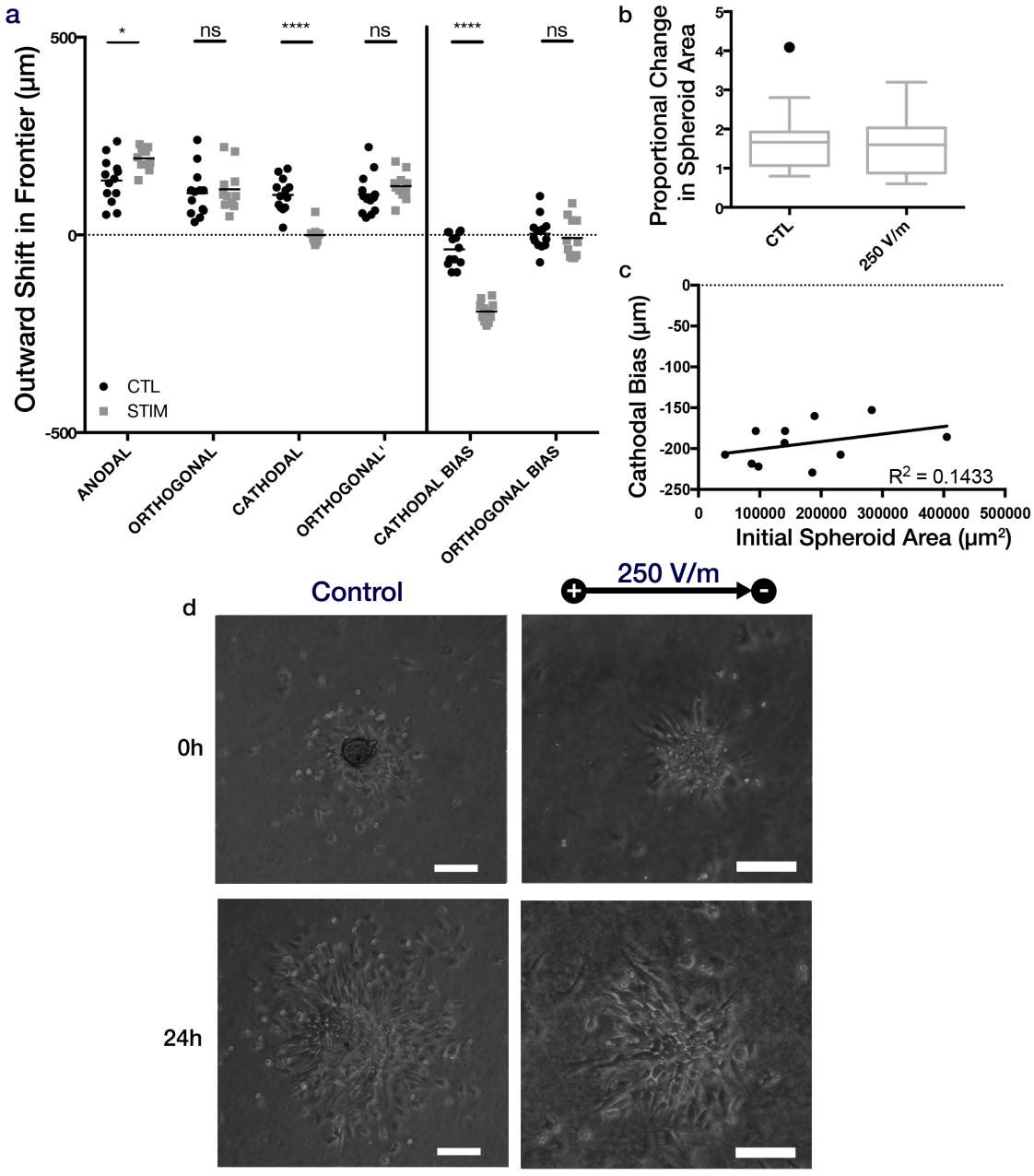

Figure 14. T98G aggregates undergo anodal electrotaxis. (a) Quantitative assessment of the outward shift of T98G aggregate frontiers after 24h. *p=0.0104; ****p<0.0001; by Two-way ANOVA and Holm-Sidak post-hoc test. Mean±SEM shown. (b) Proportional change in spheroid area from time=0 to time=24. Not significant (p=0.6832) by One-way ANOVA and Holm-Sidak post-hoc test. Mean±Tukey box plots shown. (c) Linear regression of initial spheroid area versus cathodal bias after 24h stimulation with 250 V/m dcEF. R^2=0.1433, not different than slope of 0 with p=0.2509. (d) Example T98G spheroid morphology before and after experiment, with and without 250 V/m dcEF. Scale: 200µm.

The greatest anodal bias of all the lines tested was from the U373 aggregates (Figure 15) with -235±30 μm (mean±SEM) under 250 V/m compared to a mere -10±16 μm in controls ($p<0.0001$). The outwardly extending anodal and trailing cathodal frontiers were both significantly different than in controls ($p<0.0001$). Morphologically, these cells were also distinct in that processes on the trailing end did not merely retract, yet appear to wrap around the spheroid bulk toward the anode after 24h. These aggregates displayed no overall change in spheroid area over time, and although their cathodal bias was more strongly related to initial spheroid area, this was largely due to the small variability in cathodal bias relative to the magnitude, and the linear fit was not significantly different than a slope of 0.

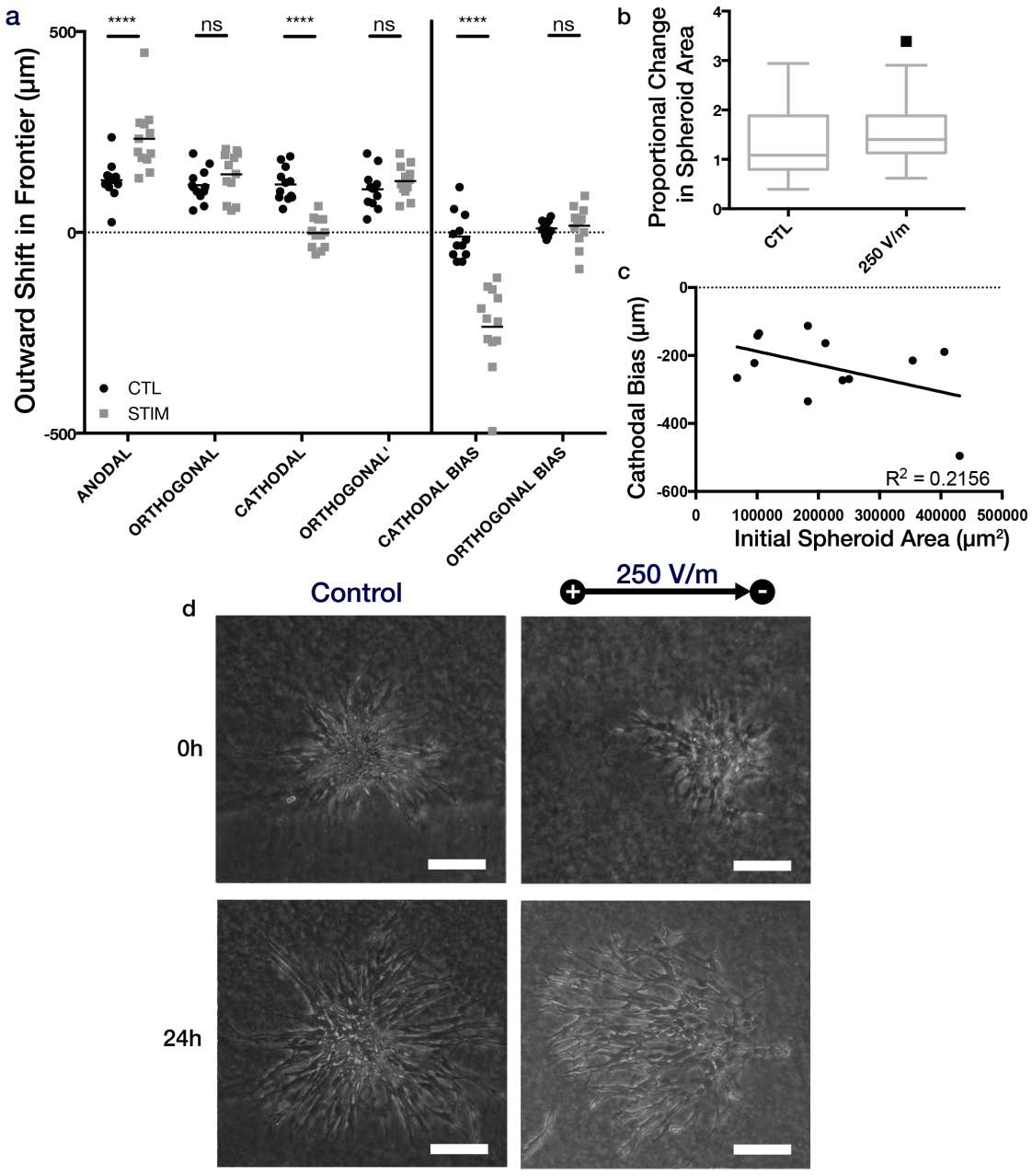

Figure 15. U373 aggregates undergo anodal electrotaxis. (a) Quantitative assessment of the outward shift of U373 aggregate frontiers after 24h. ****p<0.0001; by Two-way ANOVA and Holm-Sidak post-hoc test. Mean±SEM shown. (b) Proportional change in spheroid area from time=0 to time=24. Not significant (p=0.4068) by One-way ANOVA and Holm-Sidak post-hoc test. Mean±Tukey box plots shown. (c) Linear regression of initial spheroid area versus cathodal bias after 24h stimulation with 250 V/m dcEF. R^2=0.2156, not different than slope of 0 with p=0.1283. (d) Example U373 spheroid morphology before and after experiment, with and without 250 V/m dcEF. Scale: 200µm.

2.3.6.2 Electrotaxis of alternate MB cell lines

Two other MB cell lines were also tested for their electrotactic responses, however, these results area herein presented with skepticism. Both the D283MED and D341MED cell lines were unable to be plated as spheroidal aggregates; these cell lines are suspension culture lines and do not form strong cell-cell adherence when plated as aggregates. We attempted to plate the D341MED cells directly as monoclonal spheroids, yet these cells readily disassociated into dispersed single-cell format during mixing with matrigel. Thus, these cells have been omitted from the current study, as it would require substantial additional time to grow the D341MED cells, *in situ*, in our electrotaxis chambers.

We were able to obtain results from the D283MED line (Figure 16), which were plated as a mix of single cells and monoclonal spheroids, yet few of the spheroids survived the plating process. Nonetheless, we were able to detect a small but significant cathodal bias in these samples (22±12μm, mean±SEM, relative to 5±4μm in controls, $p=0.0444$), but two things warrant skepticism of this result: (i) effect was largely due to 2 outlying replicates; and (ii) no invasive processes can be seen extending from the spheroids. It remains unclear why the outlier samples were seen to have a cathodal effect (one is shown in Figure 16d), and whether this was truly an electrotactic effect. Nevertheless, live-cell imaging is likely required to further understand how these cells are deforming the spheroid over time.

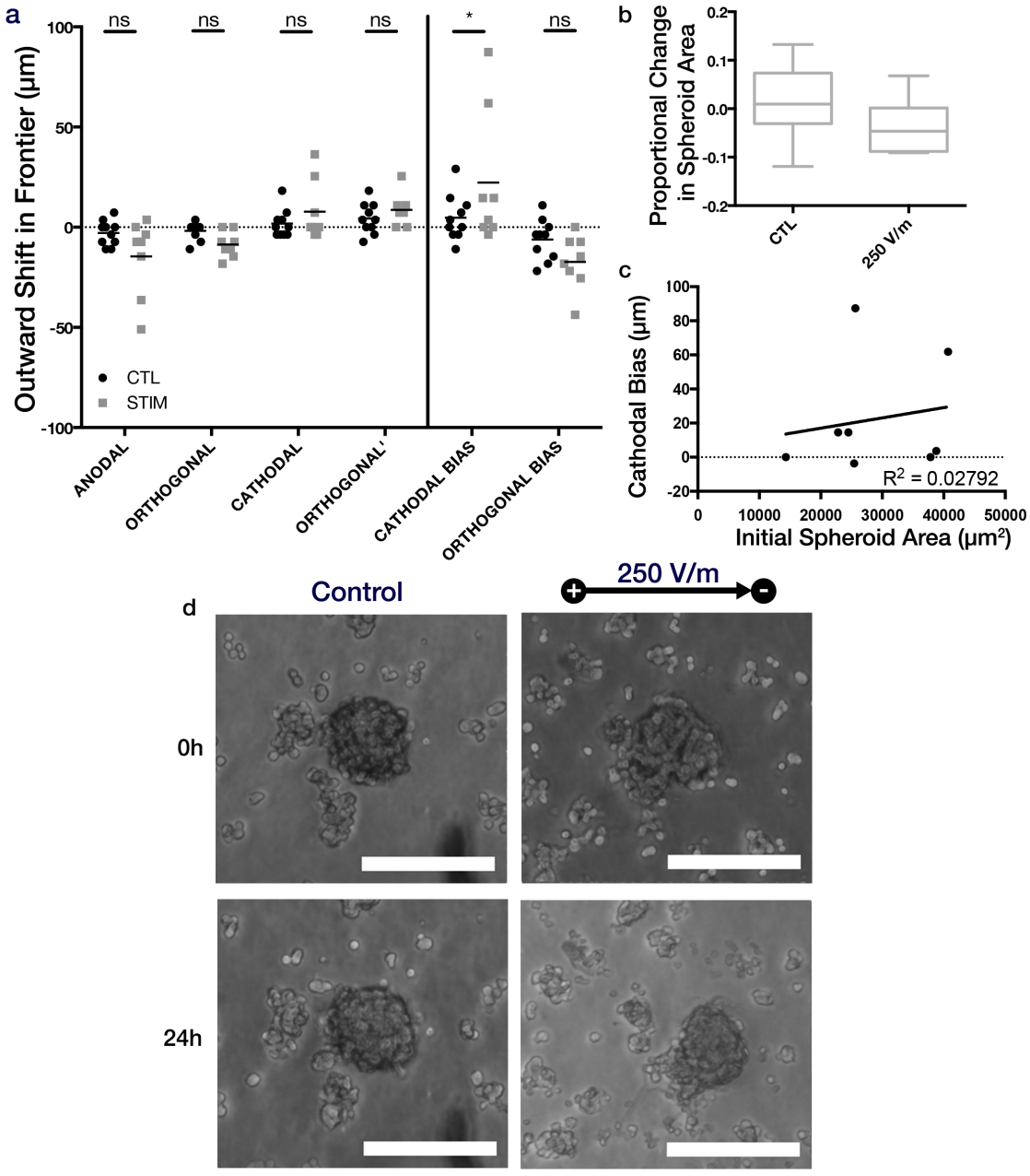

Figure 16. D283Med spheroids undergo cathodal electrotaxis, although not consistently. (a) Quantitative assessment of the outward shift of D283Med spheroid frontiers after 24h. *p<0.0444; by Two-way ANOVA and Holm-Sidak post-hoc test. Mean±SEM shown. (b) Proportional change in spheroid area from time=0 to time=24. Not significant (p=0.1414) by One-way ANOVA and Holm-Sidak post-hoc test. Mean±Tukey box plots shown. (c) Linear regression of initial spheroid area versus cathodal bias after 24h stimulation with 250 V/m dcEF. R^2=0.02792, not different than slope of 0 with p=0.6925. (d) Example D283Med spheroid morphology before and after experiment, with and without 250 V/m dcEF. Scale: 200µm.

2.4 Conclusion

In this chapter, we have described the design of our flexible *in vitro* electrotaxis system and validated it against a known electrotaxis model (MatLyLu cells). This system can be used as complement to existing electrotaxis setups, with emphasis on higher cell densities, populations in 3D, and for longer-term experiments—especially those where live-cell microscopy may not be available, or where microfluidic fabrication is inaccessible (or not cost-effective).

U87mg and DAOY cell lines were initially explored for their electrotactic responses. U87mg cells, in particular, led to the interesting finding that while they did not electrotax in 2D or diffusely in 3D—they did however electrotax when aggregated into 3D cell clusters. While we did not follow this aspect further in the current study, it acts as yet another piece of evidence that our go-to 2D *in vitro* setups are, perhaps obviously, inadequate to capture and recapitulate the full gamut of cellular responses undergoing electrotaxis.

We continued this study by testing other GBM and MB cell lines, with limited success for the MB cells. Surprisingly, all additional GBM cell lines moved in the opposite direction from the U87mg cells, and up to twice as fast (Figure 17). U87mg cells are generally considered one of the least invasive GBM cell line models, and thus this could be an array of responses similar to what was seen previously in breast and prostate cancer lines, with the metastatic potential correlating to stronger responses, and sometimes with alternate directional preference than the weakly metastatic cells.

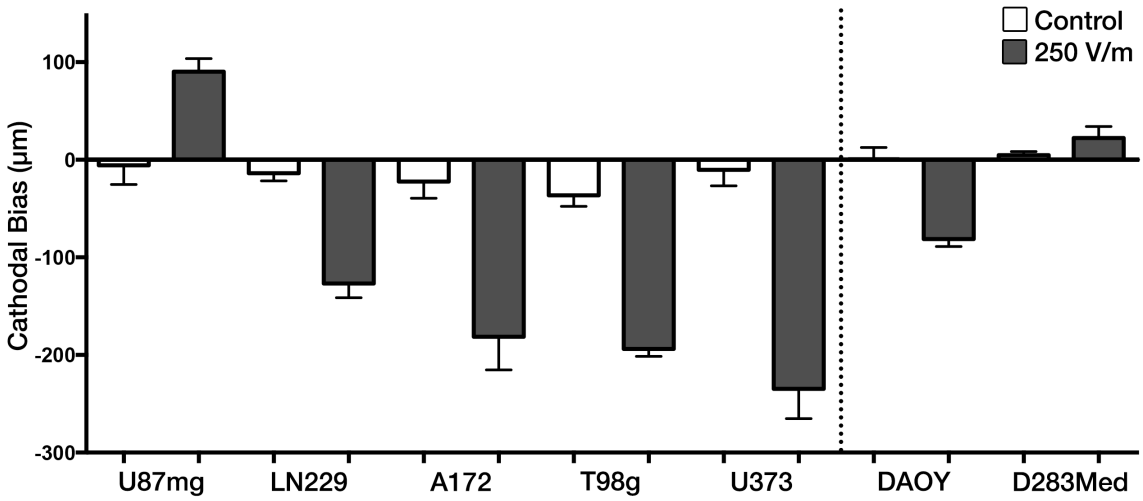

Figure 17. Comparison of electrotactic biases for GBM and MB cell lines.

Regardless, our findings suggest that there remains no guarantee, that given a particular tissue type, the cells will have similar directional preference in response to the same physio-chemical signals. In the following chapters we begin to investigate the question of why this is the case for U87mg and DAOY cells, by looking at a broad screen of potential mechanistic signaling patterns with the hope that a better understanding of cell-line-specific expression patterns could advance our understanding of how to predict, or control, an electrotactic response.

CHAPTER 3. TRANSCRIPTOMIC ANALYSIS OF U87MG GLIOBLASTOMA AND DAOY MEDULLOBLASTOMA SPHEROIDAL AGGREGATES UNDERGOING ELECTROTAXIS

3.1 Introduction

Directed cell migration and the mechanisms that underlie its processes are complex, multimodal, and often cell-specific—electrotaxis is no different. The mechanisms that have been studied or found to be in some way involved in electrotaxis have ranged from alternatively-spliced channel expression [Fraser, 2005], inositol-phospholipid signalling [Zhao, 2006], growth-factor receptor electro-polarization [Yan, 2009], purinergic receptors [Riding, 2015], lipid rafts [Lin, 2017], and glycocalyx bending [Hart, 2017].

While there exist many studies focused on a small number of or single targets, few broad signaling scans on cells undergoing electrotaxis have been performed. In their study of lung cancer electrotaxis, Huang, et al., ran microarray analyses finding 431 gene probes (out of 54,675) to be significantly different after dcEF application, with the most significantly represented signaling pathways being those for adherens and tight junctions, and hTerc transcriptional regulation [Huang, 2011]. Li, et al., included a 60-protein phosphorylation antibody array in their study, which had directed them to their consequent inquiry into dcEF-mediated effects on the ERK pathway [Li, 2013]. Barcoded Dictyostelium mutants have also been used as a high-throughput method to piece apart electrotaxis mechanisms, through conservation of genes that correlate with electrotaxis

hyperresponsitivity [Gao, 2015]. Two recent studies have included ribonucleic acid sequencing (RNA-SEQ) in their mechanistic analysis of electrotaxis, providing insights into how dcEFs impact actin cytoskeletal, mitogen-activated protein kinase (MAPK), and focal adhesion signaling [Yao, 2015; Li, 2015]. Though, even with these myriad electrotaxis mechanism studies, there is still no general consensus on how a dcEF is sensed, how an electrotactic direction is determined, nor how the directional persistence is maintained.

In this chapter, we continue the effort to explore, discover, and explain the effects of dcEFs on cellular signaling. Due to the wide gamut of purported mechanisms, we too chose to screen broadly, looking at the molecular profile of U87mg and DAOY cells—two of our cell lines tested previously that exhibited opposing electrotactic responses. In this chapter we describe our use of microfluidic quantitative, reverse transcription polymerase chain reaction (qRT-PCR) and RNA-SEQ to study underlying signaling impacts of dcEF exposure and electrotaxis.

3.2 Materials & Methods

3.2.1 in vitro cell culture and cell lines

U87mg (human glioblastoma, ATCC HTB-14), and DAOY (human medulloblastoma, ATCC HTB-186) cells were obtained from ATCC. All cells were maintained at 37ºC with 5% CO_2 in Dulbecco's Modified Eagle Medium (Cellgro 15-017CV) with 10% fetal bovine serum (Gemini 900-108), 1% L-Glutamine (Lonza 17-605F), 1% Non-essential amino acids (Cellgro 25-025-CI), and 1% penicillin-

streptomycin (Corning 30-001-CI). Cells were passaged before confluence using 0.25% Trypsin-EDTA (gibco 25200-056).

3.2.2 qRT-PCR

3.2.2.1 Cell culture and preparation

U87mg and DAOY spheroidal aggregates were formed using 700,000 cells in 3mL per agar aggrewell. Aggrewells were incubated for 24h and then spheroids were transferred to electrotaxis chamber and embedded in 1:1 cell culture medium to reduced-growth-factor Matrigel (Corning 354230) and allow to acclimate for 24h before stimulation. Cells were stimulated at 250 V/m for 0, 2, or 8h. Electrotaxis channels were scraped and the cells and Matrigel collected into 600 μL of cell recovery solution (BD, now Corning 354253) and kept on ice for 30 min. Paired duplicate samples were pooled together, providing 4 biological replicates for each condition (except 8h DAOY which only had n=3, due to poor RNA quality in one sample). Pools were centrifuged for 5 min at 800xg and resuspended in 75 μL 1% ß-mercaptoethanol (Sigma M3148)/Buffer RLT (Qiagen 79216), vortexed for 1 min, and stored at -80ºC.

3.2.2.2 RNA Isolation and quality control

RNA was isolated using an RNeasy Micro Kit (Qiagen 74004). Sample purity and concentration was assessed on a Nanodrop 2000 (Thermo-Fischer).

3.2.2.3 Primers

Electrotaxis candidate gene assay primers (100 uM) (Table 1) were obtained from Fluidigm. Primers and sequences are listed in Appendix A (Table 7). For this assay**,** ACTB, GAPDH, IPO8, RPL13A, SDHA, and TBP were used as housekeeping genes [Kreth, 2010]. For the migration gene assay, a Fluidigm-format Human Motility Array (SABiosciences PAHS-128ZH-1, 20uM) was used. Sabioscience primer sequences are proprietary, however, the genes tested are listed in Table 2 and in Appendix A (Table 8). For this assay, ACTB, B2M, GAPDH, HPRT1, and RPL13A were provided on the array as housekeeping genes.

Table 1. Candidate genes for investigation of electrotaxis mechanisms

GENE	Purported role in electrotaxis	Reference(s)
AKT1	PI3K/AKT mediated response in neural progenitor cells	Meng, 2011
CCL2	Increased gene expression in human dermal fibroblasts under dcEF	Park, 2015
CDC42	Hypothesized controller of cell polarity; Increased activity in glioma under dcEFs; Overexpressed in cathodal end of cathodal growing growth cone (xenopus) under dcEF	Etienne-Manneville, 2003; Li, 2013; Rajnicek, 2006
EGFR	Part of PI3K/AKT mediated response in NPCs; EGFR dependence of lung adenocarcinoma cells; Increased gene expression in human dermal fibroblasts under dcEF	Meng, 2011; Tsai, 2013; Park, 2015
FGF2	Increased gene expression in human dermal fibroblasts under dcEF	Park, 2015
FLT1	Up-regulated angiogenic factor in endothelial cells	Bai, 2011

Table 1 (continued)

FRK	Hypothesized down-regulation corresponding with increased invasion	Shi, 2015
FYN	Src family, hypothesized as potential migration regulator	Han, 2014
IPCEF1	Part of PI3K/AKT mediated response in neural progenitor cells	Meng, 2011
MAPK1	Increased gene expression in human dermal fibroblasts under dcEF	Park, 2015
MAPK14	(p38) Up-regulated in glioma under dcEF	Li, 2013
MAPK3	Increased gene expression in human dermal fibroblasts under dcEF	Park, 2015
MAPK8	(Janus Kinase) Up-regulated in glioma under dcEF	Li, 2013
MMP1	Hypothesized to be downstream response of dcEF induction on EGFR	Anand, 2011
MMP9	Down-regulated in human dermal fibroblasts under dcEF	Park, 2015
PIK3CA	Part of PI3K/AKT mediated response in neural progenitor cells	Meng, 2011
PRKACA	Hypothesized indicator of dcEF-induced cAMP activity	Pullar, 2005
PRKCA	Hypothesized indicator of dcEF-induced cAMP activity	Pullar, 2005
PTEN	Part of PI3K/AKT mediated response in neural progenitor cells; Down-regulated in schwann cell electrotaxis	Meng, 2011; Yao, 2015
RAC1	Necessary for keratinocyte electrotaxis; Part of NMDAR signaling pathway in electrotaxis of neural stem/progenitor cells; Increased activity in glioma under dcEFs; Overexpressed in cathodal end of cathodal growing growth cone (xenopus) under dcEFs	Pullar, 2006; Li, 2008; Li, 2013; Rajnicek, 2006
RHOA	Overexpressed in anodal end of cathodal growing growth cone (xenopus) under dcEFs	Rajnicek, 2006

Table 1 (continued)

SCN1B	Hypothesized indicator of voltage-gated sodium channel activity	Yildirim, 2012
SGK1	Hypothesized to indicate dcEF-induced ion channel activity or stress response	Lang, 2013
SOD2	Increased expression in glioma under dcEFs	Li, 2013
VEGFC	Hypothesized paracrine signal, mirroring glial precursor growth	Kranich, 2009

Table 2. Human Motility PCR Array genes grouped by functional category.

FUNCTION	**GENES**
Chemotaxis	FGF2, ITGB2, MAPK1, MYH10, MYH9, PLAUR, PLD1, PRKCA, RAC2, TGFB1, VEGFA, WASF2, WIPF1
Receptors	EGFR, IGF1R, ITGA4, ITGB1, ITGB2, ITGB3, MET, PLAUR, RHO
Growth Factors	CSF1, EGF, FGF2, HGF, IGF1, TGFB1, VEGFA
Rho Signaling	ACTR2, ACTR3, ARHGDIA, LIMK1, MSN, MYL9, MYLK, PLCG1, PLD1, PRKCA, PTEN, PTPN1, RHO, RHOA, RHOB, RHOC, RND3, ROCK1, VIM
Rac Signaling	ACTR2, ACTR3, BAIAP2, CFL1, CRK, PAK1, PAK4, PLD1, PRKCA, RAC1, RAC2, STAT3, WASF1, WASF2, WAS
CDC42 Signaling	ACTR2, ACTR3, CDC42, PFN1, WASF1, WASF2, WASL
Cell-Cell Adhesion	DPP4, EGFR, EZR, ITGA4, ITGB1, ITGB2, MSN, MYH9, ROCK1, TGFB1

Table 2 (continued)

Cell-Matrix Adhesion	ACTN1, ACTN3, CSF1 (MCSF), ILK, ITGB1, ITGB2, ITGB3, MMP14, PTEN, PTK2B, PXN, RASA1, RHOA
Focal Adhesion	ACTN1, ACTN3, ARHGEF7, BCAR1, CAPN1, CAPN2, CAV1, ENAH, ILK, ITGB1, MYL9, PTK2, PTK2B, PXN, TLN1, VASP, VCL
Leukocyte Adhesion & Rolling	EZR, ITGA4, ITGB1, ITGB2, MSN, ROCK1
Integrin-Mediated Signaling	BCAR1, ILK, ITGA4, ITGB1, ITGB2, ITGB3, MYH9, PTK2
Filopodia	BAIAP2, CDC42, DIAPH1, EGFR, ENAH, EZR, MSN, RDX, SVIL, VASP
Lammelipodia	CTTN, DPP4, EGFR, ENAH, FAP, PIK3CA, PLD1, PTK2, PXN, RDX, SVIL, VASP, VCL, WASF1, WASF2, WASL
Stress Fibers	ACTN4, DIAPH1, MYH10, MYH9, RHOA, RHOB, RHOC
Membrane Blebs	ACTN1, ACTN3, ACTN4, EZR, MYH10, MYH9, MYLK, RND3, ROCK1
Invasive Projections	ACTR2, ACTR3, ARF6, CDC42, CFL1, CTTN, DPP4, EGF, EZR, FAP, MMP14, MMP2, MMP9, MSN, MYH9, PLAUR, RAC2, RASA1, SH3PXD2A, SRC, SVIL, TGFB1, VEGFA, WASL, WIPF1
Growth Cones	ARHGEF7, CDC42, CFL1, PTK2B
Membrane Ruffles	ACTR2, ACTR3, ARF6, BAIAP2, BCAR1, CTTN, DIAPH1, EZR, ITGB1, MYH9, RAC1, RAC2, RDX, RHOA, TLN1, WASF2
Cell Polarity	CDC42, CFL1, EZR, IGF1R, ILK, MYH9

Table 2 (continued)

Proteolysis	AKT1, CAPN1, CAPN2, DPP4, FAP, HGF, MMP14, MMP2, MMP9, MYH9, PLAUR, TIMP2

3.2.2.4 Library Preparation and Fluidigm qRT-PCR

Complementary deoxyribonulcleic acid was produced slightly differently for each assay. For the candidate gene assay a RT2 First Strand kit (Qiagen 330401) was used; for the motility gene assay the RT2 Microfluidics Reagent System (Qiagen 330431) and RT2 PreAMP Pathway Primer Mix for Fluidigm (Qiagen 330241) were used. Fluidigm qRT-PCR was performed on a Fluidigm BioMark Genetic Analysis Platform at the Georgia Tech Genomics Core.

3.2.2.5 Data Analysis

qRT-PCR data were analyzed using the SABiosciences RT2 Profiler PCR Array Data Analysis web tool (version 3.5), with default settings other than a geometric mean used for housekeeping gene normalization and a cycle threshold of 35. Data were post-processed and visualized using custom Python (v2.7.x, Python Software Foundation, Anaconda Distribution) code. Multiple hypothesis correction was done with the statsmodel library using the Benjamin-Hochberg method.

3.2.3 RNA-SEQ

3.2.3.1 Cell Culture and Preparation

U87mg and DAOY spheroidal aggregates were formed using 700,000 cells in 3mL per agar aggrewell. Aggrewells were incubated for 24h and then spheroids were transferred to electrotaxis chamber and embedded in 1:1 cell culture medium to Growth Factor Reduced Matrigel (Corning 354230) and allow to acclimate for 24h before stimulation. Cells were stimulated at 250 V/m for 0, 2, or 8h. Electrotaxis channels were scraped and the cells and Matrigel collected into 600 μL of cell recovery solution (BD, now Corning 354253) and kept on ice for 30 min. Paired triplicate samples were pooled together, providing 4 biological replicates for each condition (except 8h DAOY which only had n=3, due to poor RNA quality in one sample). Pools were centrifuged for 5 min at 800xg, supernatant removed and stored at -80ºC.

3.2.3.2 RNA isolation, Quality Control and Library Preparation

RNA was extracted using a RNeasy Micro Plus Kit (Qiagen 74034). Purity and yield was assessed on a Nanodrop 2000 (Thermo-Fisher). RNA integrity was assessed with an Agilent Bioanalyzer RNA 6000 Nanokit on an Agilent Bioanalyzer 2100. The 3 biological replicates with the best quality control results were chosen for each of the 6 conditions. Library preparation was done with a TruSeq Stranded mRNA Sample Preparation Guide LT with polyA tail pull-down. Library was validated with an Agilent DNA 1000 kit after fragmentation and addition of adapters. Samples were cleaned with

AMPure XP beads and normalized with fluorimetric quantification to 10nM using a Qubit 2.0 Fluorometer using Qubit Broad Range (ThermoFisher Q32850) and High Sensitivity (ThermoFisher Q32854) kits.

3.2.3.3 Sequencing

The 3 samples for each condition with the best quality control analysis were selected for sequencing. RNA-Sequencing was performed by the High-Throughput DNA Sequencing Core Facility at Georgia Tech. Samples were run on an Illumina HiSeq 2500 with single-ended, 100 base-pair reads using a cBOT to split lanes before sequencing.

3.2.4 RNA-SEQ Data Analysis

3.2.4.1 Post-Sequencing Quality Control

Data were processed using the FASTQC Toolkit (v2.0.0, Illumina Basespace). Minimum read length was set to 32. Adapter, base, quality, and Poly-A/T trimming were performed according to previously published methods [McManes, 2014; Del Fabbro, 2013; Hansen, 2010].

3.2.4.2 Sequence alignment and differential expression

Transcript-level sequence alignment was done using the pseudo-alignment tool, Kallisto (0.43.0) [Bray, 2016] and the GENCODE v24 transcriptome for Homo sapiens (www.gencodegenes.org) [Harrow, 2012] using 100 bootstrap samples, single-end mode, with the average fragment length and standard deviation obtain for each sample during

quality control. Differential expression was performed using Sleuth [Pimentel, 2017] in R (v 3.2.1, R Foundation for Statistical Computing).

3.2.4.3 Pathway over-representation analysis

The differentially expressed transcripts were pre-filtered to exclude transcripts with an absolute fold change of less than 2-fold. For each condition-pair, gene ontology was performed using g:profiler version: r1732_e89_eg36 (http://biit.cs.ut.ee/gprofiler) [Reimand, 2016]. The Homo sapiens dataset was used and the search included Gene Ontology, Kyoto Encyclopedia of Genes and Genomes (KEGG), CORUM, Reactome, and Regulatory Motif databases and the built-in g:SCS threshold was used to correct p-values for significance cutoff. Default settings were used. QuickGo (https://www.ebi.ac.uk/QuickGO) web service was used for obtaining additional gene ontology information for visualization with Python (v2.7.x, Python Software Foundation, Anaconda Distribution).

3.2.4.4 Pathway Enrichment Analysis

Gene Set Enrichment Analysis (GSEA) (v3.0 build: 0160, http://www.broadinstitute.org/gsea) [Subramanian, 2005] was used to perform pathway enrichment analysis. Pre-ranked analysis was performed against the Molecular Signatures Database gene sets for: curated data (c2.all.v6.0), gene ontology (c5.all.v6.0), and oncogenic signatures (c6.all.v6.0) gene sets. For the ranking scheme, we used the negative-log of the multiple-hypothesis-corrected p-value (obtained via differential expression analysis in Sleuth) and signed according to the fold-change direction. The transcript with the lowest p-value was selected in cases of gene symbol collision. Default

settings were used except the maximum and minimum pathway size exclusion criteria were set to 1,000 and 5, respectively.

3.2.5 Graphing and Statistics

All graphs and statistics analysis were done with Python (v2.7.x, Python Software Foundation, Anaconda Distribution) or Prism 7 (Graphpad Inc.) unless otherwise specified. The statistical methods used are reported for each result, in place.

3.3 Results & Discussion

3.3.1 qRT-PCR: canonical motility & candidate gene arrays

Our exploration of electrotaxis mechanisms began with a series of qRT-PCR gene arrays. The first was a custom gene array comprised of 25 genes either previously shown or hypothesized to involved in electrotactic machinery (Table 1). Gene expression was compared at 2h and 8h, relative to unstimulated cells, with significant, differential expression criteria set to $p<0.05$ and Log_2(fold-change) of greater than 1 or less than -1 (Figure 18). For these conditions, however, no genes were found to be significantly differentially expression, even before multiple hypothesis corrections to the p-values.

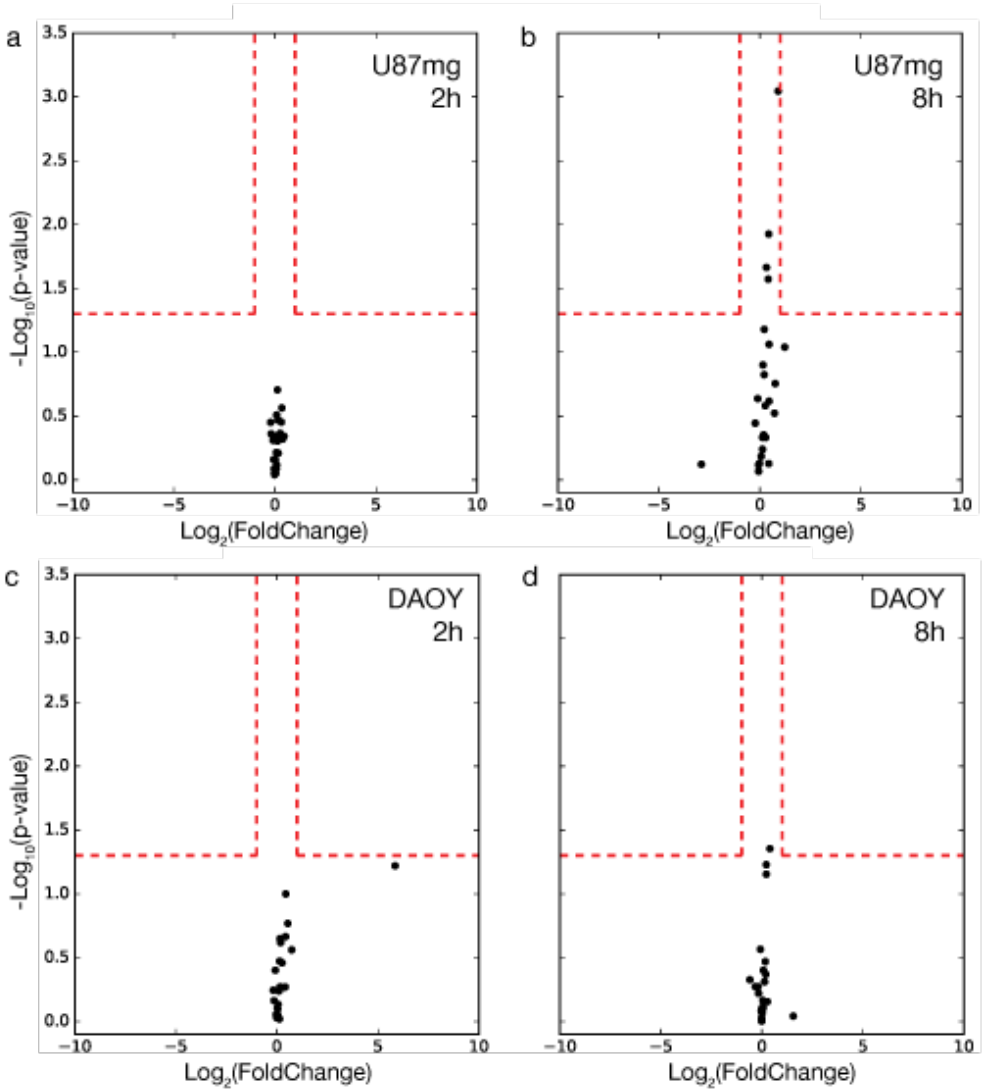

Figure 18. Candidate gene qRT-PCR volcano plots. (a & b) U87mg, or (c & d) DAOY cells were analyzed for gene expression of 25 candidate electrotaxis genes. Shown are the p-values and fold-changes for these genes comparing the expression at (a & c) 2h, or (b & d) 8h after dcEF onset, relative to controls at 0h without dcEF. Significance was determined as any gene with $p<0.05$ and a Log_2(fold-change) of greater than 1 or less than -1. No genes were found to be significantly, differentially expression for these conditions.

Next, deciding to expand our search to canonical mechanisms of cell movement, we analyzed gene expression using a commercial PCR array of known human motility genes (Table 2 and Figure 19). PLCG1 and RHOA (both involved in Rho signaling) were found to be differentially down-regulated in U87mg cells after 2h and EGF was observed to be up-regulated after 8h. The RHO receptor was the only gene found to be differentially expressed in DAOY cells, up-regulated after 8h. However, after multiple-hypothesis correction was performed on the initial p-values, none of those genes were found to remain significantly, differentially expressed.

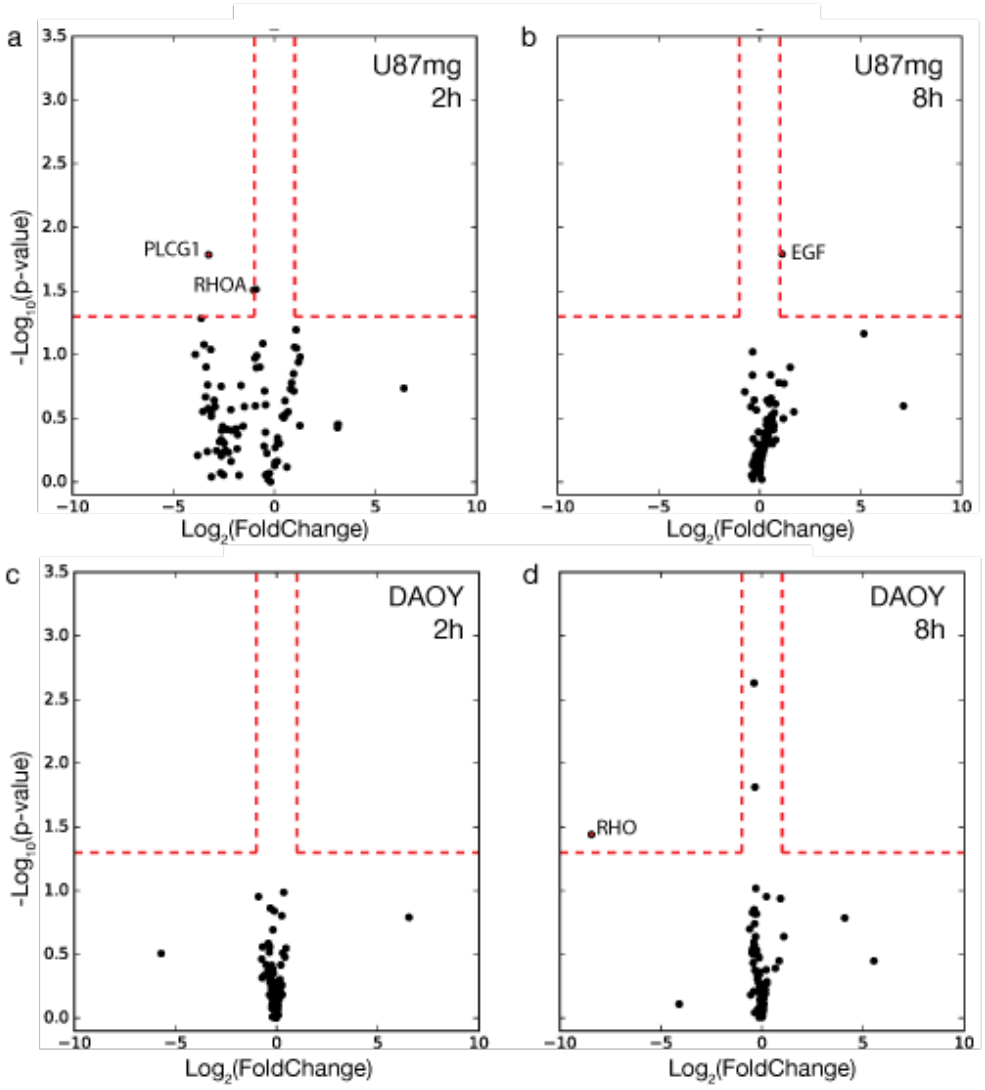

Figure 19. Motility gene array qRT-PCR volcano plots. (a & b) U87mg, or (c & d) DAOY cells were analyzed for gene expression of 25 candidate electrotaxis genes. Shown are the p-values and fold-changes for these genes comparing the expression at (a & c) 2h, or (b & d) 8h after dcEF onset, relative to controls at 0h without dcEF. Significance was determined as any gene with $p<0.05$ and a Log_2(fold-change) of greater than 1 or less than -1. While PLCG1, RHOA, RHO and EGF were found to be differentially-expressed under these criteria, after multiple-hypothesis correction was performed on the initial p-values, no genes were found to be significantly, differentially expressed.

Initially, it was surprising to see no canonical motility genes differentially expressed under dcEF, when a dramatic change in motility behavior was clearly observed. However, what is distinct about our specific electrotaxis assay, is that the cells are embedded in a rich, adhesive matrix, and even without dcEF, the cells are invading directionally—away from the center of the cellular aggregate. What this means is that more so than previous electrotaxis assays—where cells have gone from random or non-motile behaviors—our assays must be considered as moving from one form of directed invasion to another. Thus the dynamics of gene expression are likely more subtle, as they will relate more to the change in a particular cue, than a complete change in machinery for a different mode of invasion. Thus, we continued our study with a more powerful mRNA analysis tool in order to probe this subtlety.

3.3.2 RNA-SEQ

We performed RNA-SEQ on U87mg and DAOY spheroidal aggregates 0h, 2h, and 8h after being exposed to 250 V/m dcEFs. Over 91% of all transcript reads were pseudo-aligned and assigned to 145,327 unique transcript accessions (Appendix B, Figure 39). A number of these transcripts were found to be differentially expressed comparing either the 2h or 8h transcripts against the control, 0h transcripts. Differential expression was based on cutoff criteria of a false-discovery rate (FDR) < 0.05 and a Log_2(fold-change) > 1 or < -1. Both the 8h conditions had substantially more differentially expressed transcripts as was to be expected, and the DAOY 8h comparison yielded 4.5x as many as the U87mg 8h comparison (Table 3 and Figure 20**)**. Over 75% of all differentially expressed transcripts were for protein coding mRNA and the remaining were ‘processed transcripts’ (transcripts without an open reading frame) or ‘retained

introns', mapping to purported splicing variant transcripts. Heatmaps and clustermaps of the most significantly differentially expressed genes are provided in Appendix B (Figure 40, Figure 41, and Figure 42).

Table 3. Counts for differentially expressed transcripts

	U87		DAOY	
# Differentially Expressed Transcripts	**2h**	**8h**	**2h**	**8h**
Up-regulated	4	25	6	155
Down-regulated	9	39	1	137
Total	13	64	7	292

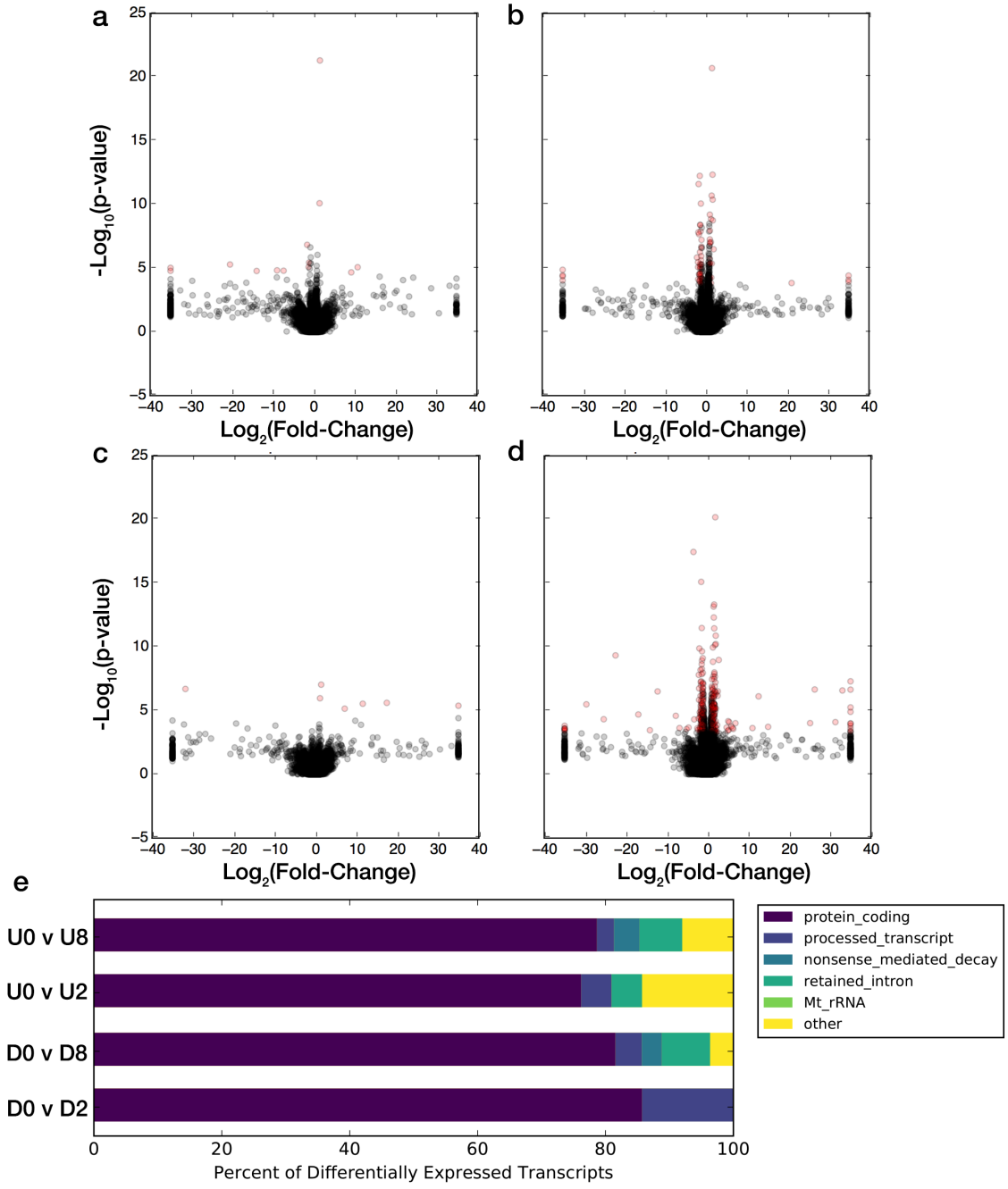

Figure 20. Differential expression of transcripts from RNA-SEQ. (a, b, c, & d) Volcano plots comparing fold-change and p-value of each identified transcript accession for (a & b) U87mg and (c & d) DAOY cellular aggregates for samples exposed to 250 V/m dcEFs for (a & c) 2h, or (b & d) 8h compared 0h, unexposed controls. Significance threshold is set to FDR < 0.05 and a Log_2(fold-change) of > 1 or < -1. Differentially expressed transcripts are shown in red. (e) Proportional breakdown of which GENCODE biotypes were associated to the identified, differentially expressed transcripts for each condition (U=U87mg, D=DAOY).

3.3.2.1 Over-representation analysis

Using the differentially-expressed transcripts, we performed a pathway over-representation analysis, finding several such over-represented pathways for all conditions except for the U87mg 2h set (Table 4). For the DAOY 2h condition, only CYR61 and TGFBR2 were found in any pathway annotations, so the pathways discovered for this search are likely unreliable for the current study: atrioventricular valve development & morphogenesis, and TGFB-receptor type II homodimer complex. Selected pathways from this analysis are listed in Appendix B (Table 9, and Table 10). Both the U87 8h and DAOY 8h conditions yielded significant over-representation for mRNA metabolism, and gene expression regulation. A substantial number of transcription factors were also identified as being significantly overrepresented (Appendix B, Table 11). Additionally, the pathways for establishment of RNA localization, cell stress, and mRNA splicing via spliceosome were overrepresented in DAOY 8h genes. mRNA localization, for ß-actin in particular, has been previous implicated as a factor in directed cell migration [Shestakova, 2001]. Additionally, ATPase regulator activity was significantly overrepresented in U87 8h genes, which was previously shown to occur in tandem with ß-actin localization at the leading edge in electrotaxing calvarial osteoblasts [Özkucur, 2011]. However, further analysis would be required to determine which, if any, mRNA are being re-localized to this effect.

Table 4. Counts for over-represented pathways by condition

	U87mg		DAOY	
	2h	**8h**	**2h**	**8h**
# of significantly over-represented pathways	0	94	3	217

Genes that were found to be differentially expressed after 8h for both U87mg and DAOY were well correlated to each other, with a Pearson's correlation coefficient of 0.9397 ($p<7.9x10^{-19}$) (Figure 21). 5 pathways were found to be significantly over-represented using this gene subset: RNA splicing, gene expression, RNA metabolic process, and two transcription factor pathways, ETV7 and E2F1 (Appendix B, Table 12). This suggests that if there is indeed a conserved transcriptional machinery in response to dcEF exposure, it may lie in regulation of RNA spling and processing.

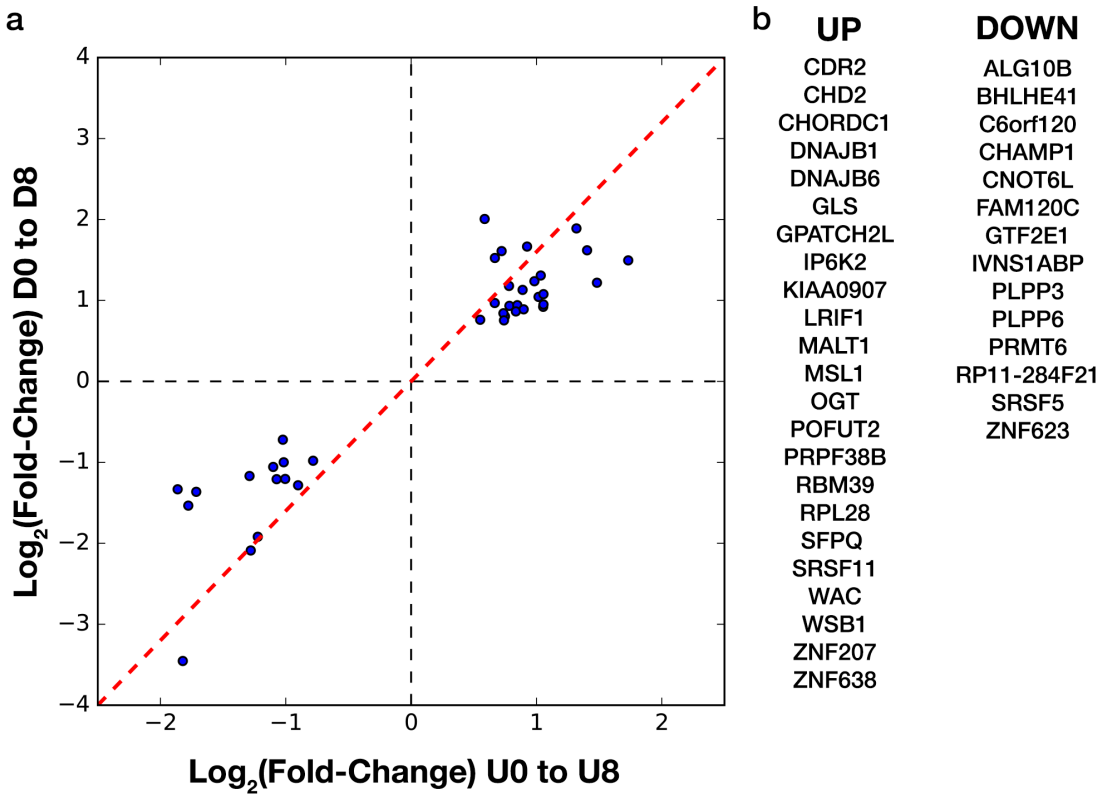

Figure 21. Correlation of transcripts differentially expressing in U87mg and DAOY. (a) Scatterplot of all transcripts that were differentially expressed after 8h dcEF for both U87mg and DAOY cellular aggregates. (b) List of gene symbols for based whether they were significantly up-regulated, or down-regulated for both U87mg and DAOY after 8h dcEF. No genes were found that fell outside these two sets.

We also explored transcripts that were differentially expressed, but not for both cell types, and that had opposite directions of regulation across the two cell types (Figure 22). These genes were of interest as candidates for describing the difference in directional preference between the cathodally-directed U87mg and anodally-directed DAOY cells, though no pathways were found that were significantly overrepresented by either subset of these genes (quadrants II and IV in Figure 22).

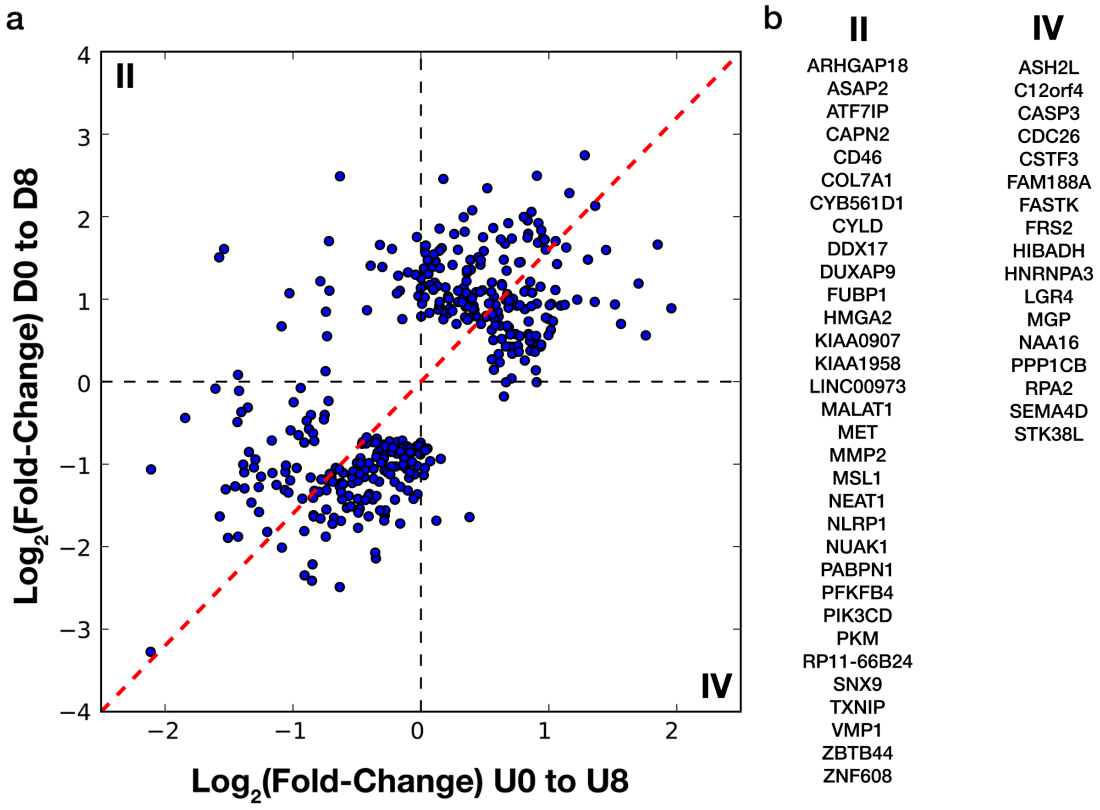

Figure 22. Correspondence of transcripts differentially expressed in U87mg and DAOY. (a) Scatterplot of all transcripts that were differentially expressed after 8h dcEF for both U87mg and DAOY cellular aggregates. (b) List of gene symbols for based whether they were significantly up-regulated, or down-regulated for both U87mg and DAOY after 8h dcEF. No genes were found that fell outside these two sets.

3.3.2.2 Gene-set enrichment analysis

We next performed a gene-set enrichment analysis using all transcripts with custom ranking: transcripts were ordered by the -Log-transformed p-values with the sign corresponding to the direction of their fold-change applied. Three of the msigDB gene sets were used, CURATED, GENE ONTOLOGY (GO), and ONCOGENIC, and the

number of significantly enriched gene sets for each are provided in Table 5. Significance criteria was p-value<0.05 and the GSEA tool recommended false-discovery rate of 0.25.

Table 5. Gene-set enrichment analysis summary counts.

	D2	D8	U2	U8
CURATED	872	1028	720	753
GO	168	153	248	539
ONCOGENIC	25	20	28	30
TOTAL	1065	1201	996	1322

While there is not sufficient space in this thesis to present all of the significantly enriched gene sets, we have culled the lists for pathways we hypothesize, or have been previously shown, to be relevant to electrotaxis machinery. We found only limited pathways that matched the 2 previous RNA-SEQ studies for electrotaxis, which could be due to our cells being in 3D or plated as spheroids in invasion-promoting matrix. Li, et al. had found the broad cytokine-cytokine receptor and chemokine signaling pathways to be differentially regulated, however, neither of these were found enriched for any of our conditions [Li, 2015]. KEGG focal adhesion and MAPK signaling pathways were found to be upregulated, but only in DAOY cells, yet this matching the findings of Yao, et al. for Schwann cell electrotaxis toward the anode [Yao, 2015].

Several signatures of chemotaxis were also present. Most strikingly, all conditions showed upregulation of genes matching data from Mili, et al., a study that characterized RNAs that were localized to cell protrusions under chemotaxis and haptotaxis [Mili, 2008]. The gene ontology for RNA localization was also significantly enriched for all dcEF conditions.

There were also many pathways enriched relating to the phosphoinositide 3-kinase (PI3K) pathway, a pathway highly involved in chemotaxis intracellular regulation and previously shown to be a mediated of neural progenitor cell electrotaxis [Meng, 2011]. Related pathways include the reactome PI3K cascade in both U87mg and DAOY cells after dcEF exposure, and gene ontology for phosphatidylinositol (3,4,5)-triphosphate in DAOY cells. Mechanistic target of rapamycin (mTOR) genes were also enriched, as pathways for rapamycin sensitive genes, mTOR signaling and the Insulin-like growth factor 1 (IGF1)/mTOR pathways were enriched in both cell lines.

Several growth-factor-associated pathways were also upregulated for both cells including reactome pathways for EGFR, fibroblast growth factor receptor, Insulin receptor, transforming growth factor Beta (TGFB), and nerve growth factor, and the pathway interaction database pathways for MET, platelet-derived growth factor Beta, TGFB receptor, and vascular endothelial growth factor 1 and 2. All conditions also displayed positive enrichment for genes that had been previously found to be co-regulated by hepatocyte growth factor (HGF) and Ki-Ras oncogene activity [Seiden, 2006]

ErbB and EGFR signaling were also well represented by the significantly enriched gene sets. Both DAOY and U87mg cells under dcEFs were enriched for the gene ontology for regulation of ErbB signaling as well as the pathway interaction database ErbB1 downstream gene set. Enriched genes for both DAOY and U87mg cells under dcEFs also reflected data for genes affected by ErbB ligands, EGF & neuregulin 1 [Nagashima, 2007].

Matching the over-representation analysis, both DAOY and U87mg 8h conditions were enriched for ATPase activator and regulator activity, as well as numerous pathways relating to spliceosome including the gene ontologies for regulation of mRNA splicing and prespliceosome, as well as the KEGG pathway for the spliceosome.

3.4 Conclusion

Mechanistic literature on electrotaxis has been limited in scope and largely contradictory when comparing between different cells. Single target methods, such as antibodies or inhibitors, have often been used, but are difficult to scale to screen the multitude of pathways involved in electrotactic processes—complex processes such as extracellular sensing and transduction, or cell polarity, motility, and persistent invasion. Scouring the underlying signaling pathways with omic-level analysis may be a better way to initially characterize a cell's response, but has been relatively unused for electrotaxis studies. Further, causal effects of dcEFs on cells can be simultaneously explored when performed omic analyses, as the procurement of transcripts from a bulk cell does not discriminate to only those signals involved in electrotaxis.

Our initial high-throughput qRT-PCR custom screens elicited no findings for our two cell lines, U87mg and DAOY, under dcEFs. However, this seems to show that by plating cells in conditions where their phenotype is already highly invasion and directional (outward from the center of the spheroidal aggregates), can provide a baseline of motile behavior, useful for better remove the background of standard motility processes that are not specific to electrotaxis.

In order to investigate more deeply into the dcEF-mediated cellular signaling, we performed RNA-SEQ, taking a temporal snapshot of the bulk transcriptome as the dcEF was applied. In our analysis, we found many pathways that were significantly impacted by the dcEF, ranging from chemotaxis, to growth factor signaling, to intermediate signaling activity of the PI3K and mTOR pathways. We saw enrichment and overrepresentation of spliceosome and RNA localization pathways, and ATPase regulation. Yet, just because a pathway is over-represented or enriched does not guarantee it will be causally linked to electrotaxis. Thus, in the next chapter, we attempt to validate some of these hypothetical mechanisms with a series of selective inhibitor studies.

CHAPTER 4. ASSESSMENT OF THE ROLE OF SELECT PATHWAYS ON ELECTROTAXIS USING PHARMACOLOGICAL INHBITION

4.1 Introduction

Our transcriptomic analysis provided numerous hypotheses that require further validation. In this chapter, we aim to test a select few of these, in order to determine whether what we have seen in terms of gene expression is causally linked to electrotaxis.

For simplicity, we have first constrained our inquiry to inhibition studies that can be performed with the mere addition of a pharmacological agent. Secondly, we have chosen targets using the PI3K pathway as a nexus, since many of our transcriptomic findings, as well as previous electrotaxis studies, have pointed to this pathway as an intermediate regulator for transducing the sensing of a dcEF into the persistent and directional migration of a cell. The inhibitor targets we have chosen are displayed in Figure 23 and listed in Table 6.

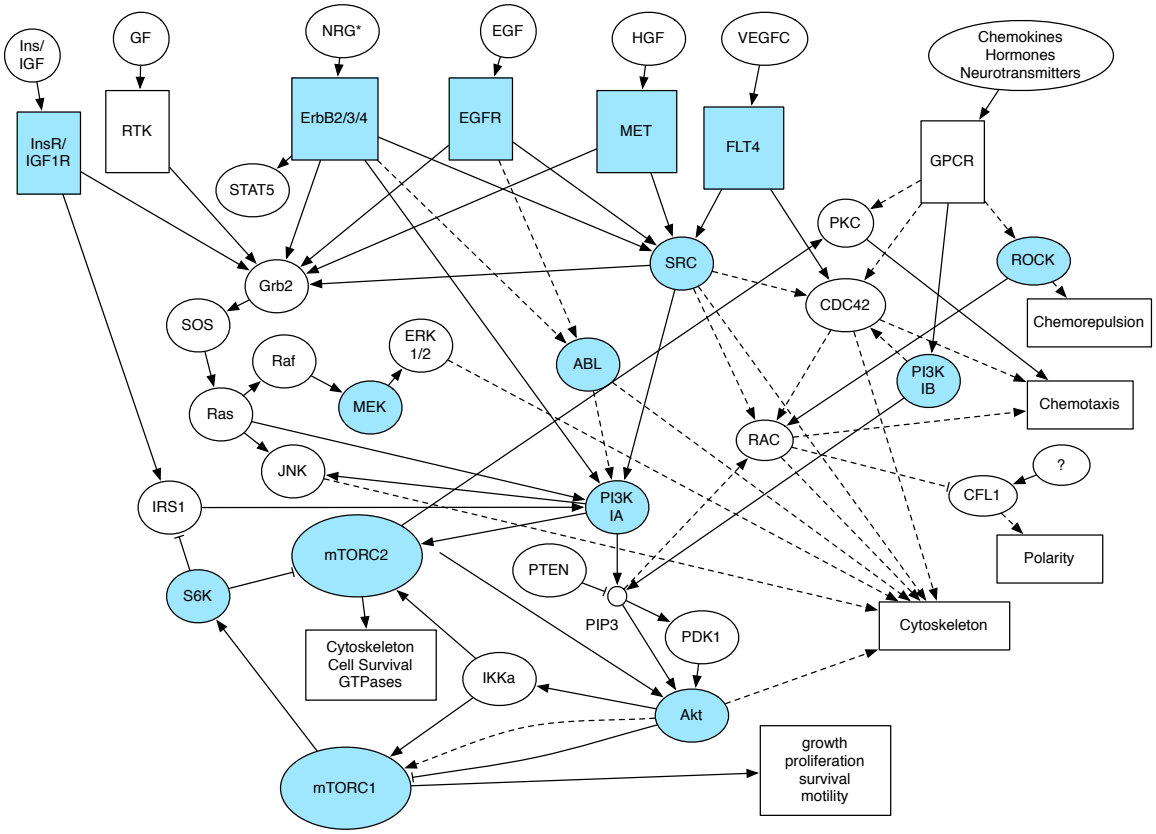

Figure 23. Abridged pathway network for selected targets. Inhibited components are highlighted in blue. Data obtained from multiple KEGG pathways [Kanehisa, 2000].

Table 6. Pharmacological Inhibitors used to explore electrotaxis pathways. Note, some compounds were used at multiple doses (highlighted in red).

Compound	CAS#	Target(s)	Dose(s) (uM)
Isoginkgetin	548-19-6	pre-mRNA splicing	33
AZD8931	848942-61-0	EGFR, ErbB2/3	**1, 10**
OSI-906	867160-71-2	IGF1R, InsR	1

Table 6 (continued)

Bosutinib	380843-75-4	Src, Abl	1
KU-0063794	938440-64-3	mTORC1/2	2.5
MK-2206	1032350-13-2	Akt1/2/3	2
Foretinib	849217-64-7	Met, KDR, Tie-2, FLT4	0.5
PD0325901	391210-10-9	MEK	0.5
LY294002	154447-36-6	PI3Kα/δ/β	**2, 20**
BEZ235	915019-65-7	PI3Kα/δ/β/γ, mTOR, ATR	**0.025, 0.25**
Rapamycin	53123-88-9	mTOR	0.1
Erlotinib	183319-69-9	EGFR	**5, 50**
CZC24832	1159824-67-5	PI3Kγ	1
Mubritinib	366017-09-6	ErbB2	1
Y-27632	129830-38-2	ROCK1/2	10
AZ5104	1421373-98-9	EGFR, ErbB4	0.006

4.2 Materials & Methods

4.2.1 in vitro Cell Culture and Cell Lines

U87mg (human glioblastoma, ATCC HTB-14) cells were obtained from ATCC. DAOY (human medulloblastoma, ATCC HTB-186), and MCF-7 (human adenocarcinoma, ATCC HTB-22) cells were obtained from the Duke University Cell Culture Facility, all originally sourced from ATCC. All cells were maintained at 37ºC with 5% CO_2 in Dulbecco's Modified Eagle Medium (Cellgro 15-017CV) with 10% fetal bovine serum (Gemini 900-108), 1% L-Glutamine (Lonza 17-605F), 1% Non-essential amino acids (Cellgro 25-025-CI), and 1% penicillin-streptomycin (Corning 30-001-CI). Cells were passaged before confluence using 0.25% Trypsin-EDTA (gibco 25200-056).

4.2.2 Pharmacological Inhibitors

Inhibitors used (listed in Table 6) were obtained from SelleckChem, with the exception of Isoginkgetin, which was purchased from Sigma-Aldrich. Doses were selected based on literature and experimental data provided by SelleckChem (see Appendix C, Table 13). Inhibitors were solubilized in dimethyl sulfoxide (Sigma-Aldrich, D2650) according to manufacturer instructions and stored in high-concentration aliquots at -80ºC prior to making working dilutions with cell culture media, which were stored at -20ºC for no more than one month prior to experiments. Working solutions were thawed for use immediately beforehand at room temperature.

4.2.3 Inhibition/Electrotaxis Assays

U87mg or DAOY spheroidal aggregates were plated in electrotaxis chambers and dcEFs were applied as described in Chapter 2. However, for conditions with inhibitors, appropriately concentrated solutions were added immediately before matrigel was added to the cell-aggregates/media solution. Cells were again given 24h in matrigel (and inhibitor, if specified) before application of dcEF. Analysis of spheroidal aggregates was performed as described in Section 2.2.8.

4.2.4 Microscopy

Images were taken with a Leica DMi8 with Leica Application Suite X tile scan. Plates were all aligned in the microscope such that the anodal side (direction toward positive battery terminus) is to the left of the image. Z plane focus was set to the middle depth of the channel.

4.2.5 Viability Assays

For our initial inhibitor studies, viability assays (see Appendix C, Figure 43) were performed using Cell-Counting Kit 8 (CCK8) (Dojindo, CK04-01). 5000 cells were plated in test wells of a 96-well plate (biological replicates, n=4). Cells plated at densities of 5000, 2500, 1250, and 0 without inhibitors, as well as blank, media-only wells, and 5000 cell wells with 1% dimethyl sulfoxide (Sigma-Aldrich, D2650) were used as controls. Cells were incubated with inhibitors for 24h before addition of CCK8 solution for 1h before imaging on a plate reader (SpectraMax i3x, Molecular Devices) at 450nm absorbance.

4.2.6 Flow cytometry

For ErbB2 cell surface expression, U87mg cells were plated as 2D dispersed, 3D dispersed, and as spheroidal aggregates with and without matrigel. Cells and aggregates were trypsinized and stained in phosphate-buffered saline (Corning 21-040-CV) with 10% fetal bovine serum (Gemini 900-108) and 0.09% sodium azide (Sigma-Aldrich, S2002). ErbB2 expression was measured using 1:20 dilutions of APC/Fire 750 anti-human CD340 (BioLegend 324421) and APC/Fire 750 mouse IgG1, κ isotype (BioLegend 400195) as negative control. MCF-7 cells, known to have elevated ErbB2 expression, plated as 2D dispersed were used as positive control for CD340. Cells were analyzed on a Novocyte 2060 flow cytometer. All flow cytometry data analysis was performed using FlowJo vX.07.

4.2.7 Graphing and statistics

All graphs and statistics analysis were done with Python (v2.7.x, Python Software Foundation, Anaconda Distribution) or Prism 7 (Graphpad Inc.) unless otherwise specified. The statistical methods used are reported for each result, in place. $\alpha=0.05$ unless otherwise specified.

4.3 Results & Discussion

We characterized the invasive responses of DAOY and U87mg cellular aggregates under exposure to various pharmacological inhibitors with and without dcEF. Data is provided in the appendix for the proportional change in spheroidal bounding box for the controls without dcEF, from 24h to 48h after exposure to each inhibitor (Appendix C,

Figure 44). Only rapamycin's effect on the U87mg cells was found to be significantly different than controls (p=0.0039) with a negative proportional change in area over that time period. Additionally, viability data is also provided in the appendix for our initially tested inhibitors (Appendix C, Figure 43**)**. The mTOR1/2 inhbitor, KU-0063794, significantly affected viability over 24h exposure for both U87mg and DAOY cells, though it was at a level consistent with the amount of growth for no additional proliferation, and morphologically, the cells did not appear to be distressed. Similarly, the pan-AKT inhibitor, MK-2206, had a similar outcome for the U87mg cells. It is important to note these findings as it may constrain our claims when it comes to the electrotactic effects on the cells with those inhibitors.

4.3.1 PI3K Signaling Inhibition

The PI3K pathway has been previously studied in electrotaxis, as mentioned above, and is of particular interest with respect to the hypothesis that electrotaxis is just another form of chemotaxis—the notion that electrotaxis is just electrophoresis of extracellular macromolecules forming a signaling gradient. The pathway is also important for the production and maintenance of intracellular signaling gradients, and is part of the signaling that often impacts the specific directionality of a given cell. Thus, we are interested in determining whether and how this pathway impacts either of the cell lines we have been studying.

Our first set of inhibitors target the PI3K pathway directly. For DAOY cells, neither pan-PI3K inhibitor, LY294002 (2 μM) nor BEZ235 (25 nM), appeared to affect the electrotactic bias (Figure 24).

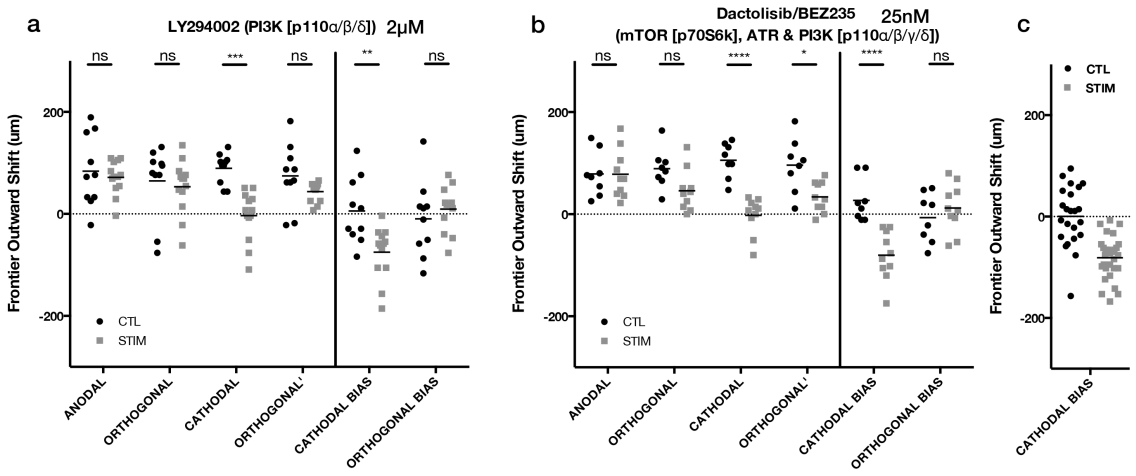

Figure 24. PI3K inhibitors for DAOY cells. 24h hours after dcEF (stim) or controls without dcEF (CTL) (a) LY294002 (2 μM) ***p=0.0003, **p=0.0020, ns=not significant (b) BEZ235 (25 nM) *p=0.0112, ****p<0.0001, ns=not significant (c) DAOY data without inhibitor compounds, redisplayed from section 2.3.6. Two-way ANOVA, Holm-Sidak post-hoc. Mean±SEM shown.

Although direct inhibition of PI3K was not impacted for DAOY, we continued our study by moving downstream to the mTOR pathway, which is also involved in many aspects of cell growth and invasions, sometimes independently of PI3K signaling. The mTOR inhibitor, rapamycin (100 nM), appeared to increase overall outward growth of the DAOY cells, however the anodal bias was still preserved (Figure 25a). Inhibition of mTORC1/2 with KU-0063794 no longer exhibited an anodal bias, however this was one of the conditions were viability was affected, and there appears to be an overall decrease in outward frontier growth (Figure 25b).

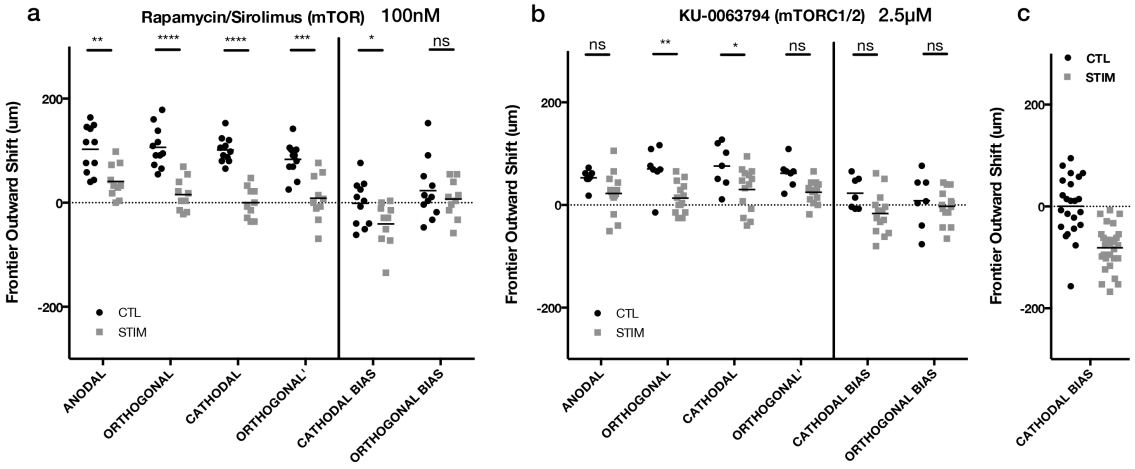

Figure 25. mTOR inhibitors for DAOY cells. 24h hours after dcEF (stim) or controls without dcEF (CTL) (a) Rapamycin (100 nM) **p=0.0014, *p=0.00465, ****p<0.0001, ns=not significant (b) KU-0063794 (2.5 μM) **p=0.0057, *p=0.0351, ns=not significant (c) DAOY data without inhibitor compounds, redisplayed from section 2.3.6. Two-way ANOVA, Holm-Sidak post-hoc. Mean±SEM shown.

We also tested DAOY cells against PI3K upstream and downstream targets, but neither IGF inhibition with OSI-906 (1 μM), nor pan-AKT inhibition with MK-2206 (2 μM), had an effect on these cells (Figure 26).

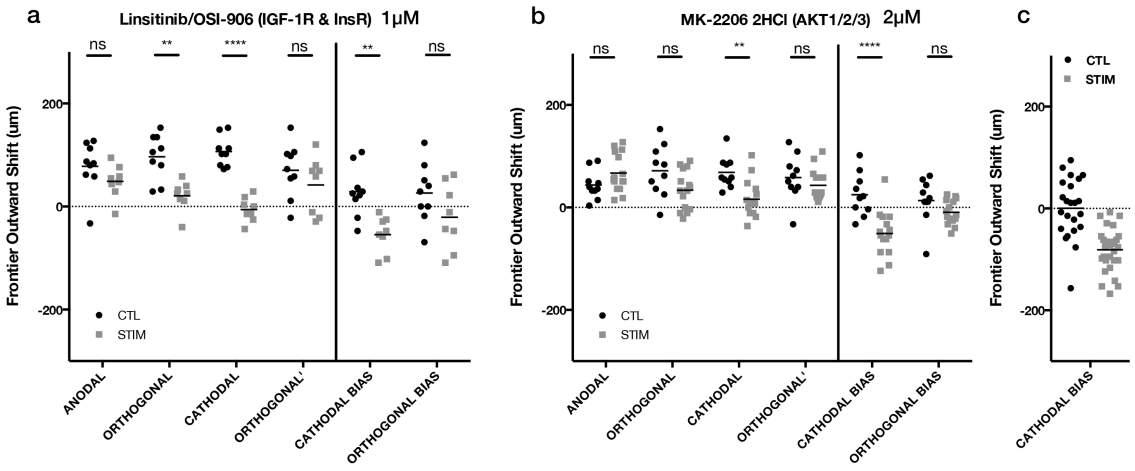

Figure 26. IGF/AKT inhibitors for DAOY cells. 24h hours after dcEF (stim) or controls without dcEF (CTL) (a) OSI-906 (1 μM) **p=0.0034 (orthogonal), **p=0.0013 (cathodal bias), ****p<0.0001, ns=not significant (b) MK-2206 (2 μM) **p=0.0040, ****p<0.0001, ns=not significant (c) DAOY data without inhibitor compounds, redisplayed from section 2.3.6. Two-way ANOVA, Holm-Sidak post-hoc. Mean±SEM shown.

However, unlike the DAOY cells, the U87mg cells appear to require aspects of the PI3K signaling pathway for electrotaxis. Pan-PI3K inhibition resulted in a loss of significant difference in the outward movement of the cathodal frontier, and, although it was still significantly different, the cathodal bias under LY294002 (2 μM) inhibition appeared slightly diminished relative to no inhibitor controls (Figure 27). Surprisingly, BEZ235 (25 nM) inhibition led to a small significant difference in cathodal bias, but the directionality was now slightly anodal.

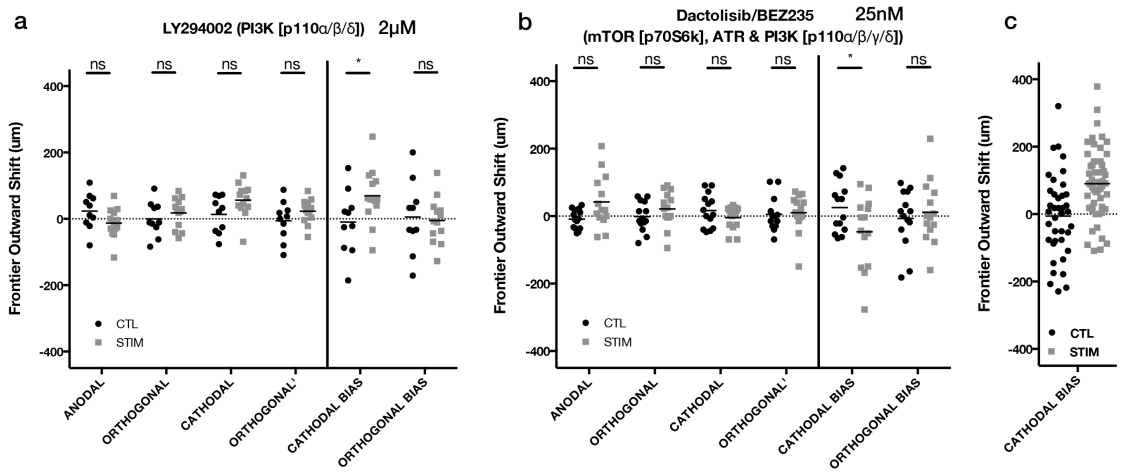

Figure 27. PI3K inhibitors for U87mg cells. 24h hours after dcEF (stim) or controls without dcEF (CTL) (a) LY294002 (2 μM) *p=0.0269, ns=not significant (b) BEZ235 (25 nM) *p=0.0306, ns=not significant (c) U87mg data without inhibitor compounds, redisplayed from section 2.3.6. Two-way ANOVA, Holm-Sidak post-hoc. Mean±SEM shown.

A follow-up study was run with the same inhibitors (LY294002 and BEZ235), but this time with 10x higher dose (Figure 28). The results for LY294002 (20 μM) were consistent with the smaller dose, and seemed to have no overall effect on the cathodal bias. For BEZ235 (250 nM), the bias was no longer anodal, however, any electrotactic bias was gone, and the frontiers appeared to be no different than the unstimulated controls.

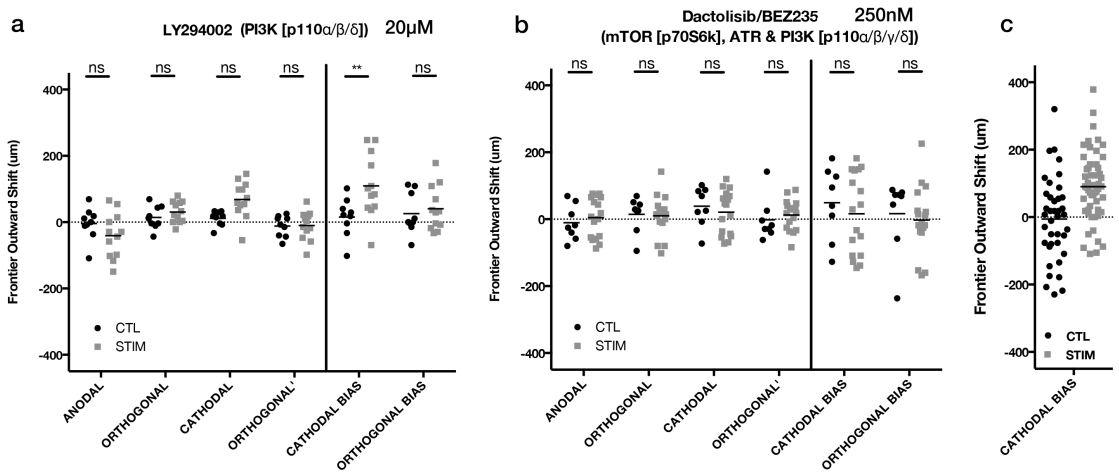

Figure 28. PI3K inhibitors at increased dosage for U87mg cells. 24h hours after dcEF (stim) or controls without dcEF (CTL) (a) LY294002 (20 μM) **p=0.0015, ns=not significant (b) BEZ235 (250 nM) ns=not significant (c) U87mg data without inhibitor compounds, redisplayed from section 2.3.6. Two-way ANOVA, Holm-Sidak post-hoc. Mean±SEM shown.

There are only a few targets that don't overlap between LY294402 and BEZ235, one of those being PI3Kγ, unique from other PI3Ks in that it is primary an intermediate in the G-protein coupled receptor pathway (GPCR)—whereas PI3Ks α, β, and δ are more strongly tied to receptor tyrosine kinase signaling. We used the PI3Kγ-specific inhibitor, CZC24832 (1 μM) to test the hypothesis that this was the particular target that was necessary for producing an electrotactic bias (Figure 29), and indeed, specific inhibition of PI3Kγ appeared to also obliterate any electrotactic bias. This strongly suggests that PI3Kγ signaling and potentially upstream signaling from GPCRs play a role in the electrotaxis of U87mg cells. This finding is also strengthened by earlier evidence that PI3Kγ is crucial for cathodal electrotaxis, where Zhao, et al., showed growth attenuation

in dcEF-assisted wound healing for PI3Kγ-knockout murine cells relative to wild-type cells [Zhao, 2006].

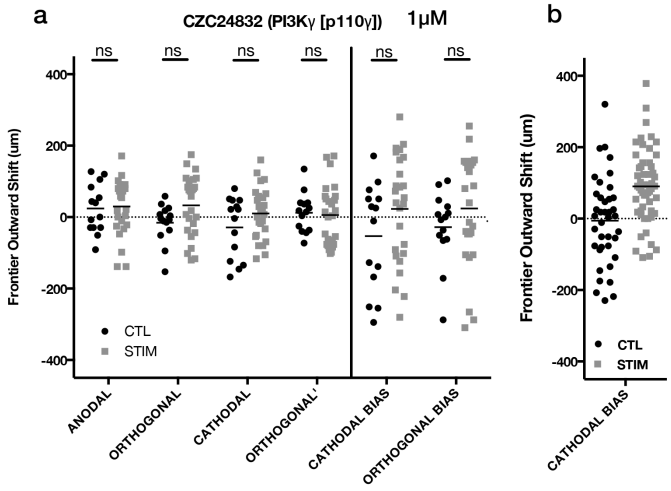

Figure 29. PI3Kγ inhibitor for U87mg cells. 24h hours after dcEF (stim) or controls without dcEF (CTL) (a) CZC24832 (1 μM) ns=not significant (b) U87mg data without inhibitor compounds, redisplayed from section 2.3.6. Two-way ANOVA, Holm-Sidak post-hoc. Mean±SEM shown.

We continued our exploration of U87mg PI3K signaling's role in electrotaxis with the finding that inhibition of mTOR and mTORC1/2 both led to abrogation of any electrotactic bias (Figure 30) as well as pan-AKT inhibition (Figure 31b). IGF inhibition did not impact cathodal bias (Figure 31a), which was expected as IGF signaling requires the PI3K pathway that includes PI3Ks α, β, and δ.

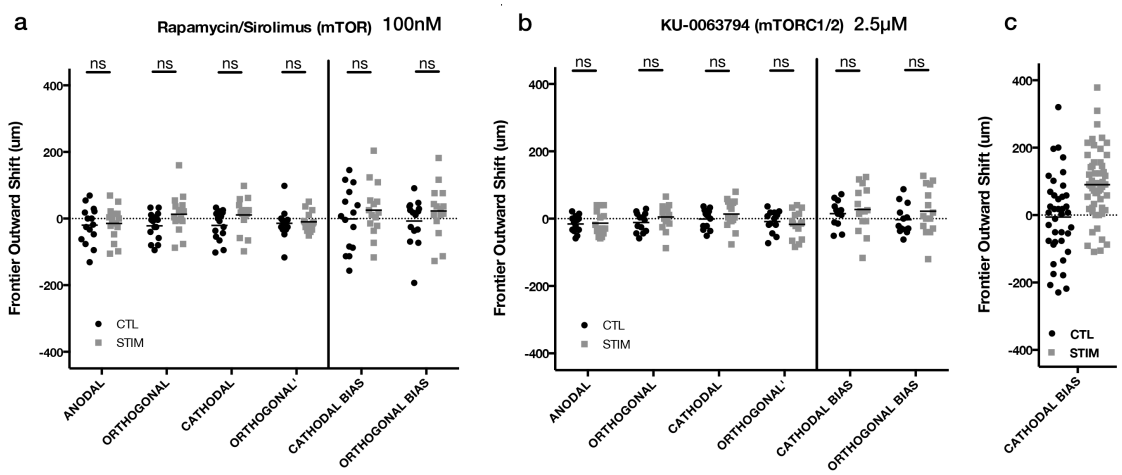

Figure 30. mTOR inhibitors for U87mg cells. 24h hours after dcEF (stim) or controls without dcEF (CTL) (a) Rapamycin (100 nM) ns=not significant (b) KU-0063794 (2.5 μM) ns=not significant (c) U87mg data without inhibitor compounds, redisplayed from section 2.3.6. Two-way ANOVA, Holm-Sidak post-hoc. Mean±SEM shown.

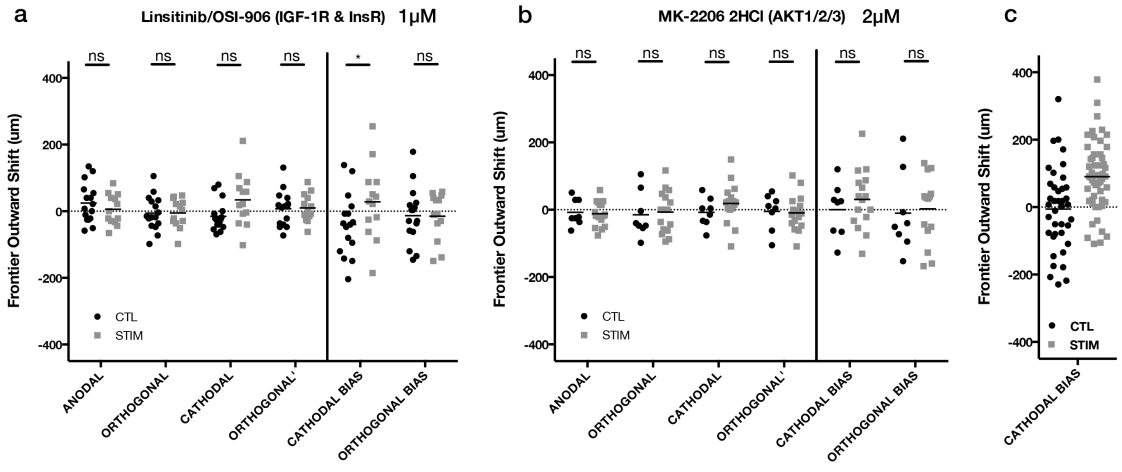

Figure 31. IGF/AKT inhibitors for U87mg cells. 24h hours after dcEF (stim) or controls without dcEF (CTL) (a) OSI-906 (1 μM) *p=0.0479, ns=not significant (b) MK-2206 (2 μM) ns=not significant (c) U87mg data without inhibitor compounds, redisplayed from section 2.3.6. Two-way ANOVA, Holm-Sidak post-hoc. Mean±SEM shown.

4.3.2 ErbB signaling inhibition

Another pathway for which we observed broad regulatory changes in our RNA-SEQ data was the ErbB pathway. This family of surface receptors is known to form hetero- and homo-dimers on the cell surface as sensors for various ligands. EGFR has been previously studied for its role in electrotaxis, as mentioned above, yet the other ErbB isoforms have not. We began our study by targeting 3 of the 4 main ErbB2 isoforms, EGFR (or ErbB1), ErbB2 (or HER2), and ErbB3 (or HER3).

Inhibition of ErbB signaling with neither Erlotinib (5 μM) nor AZD8931 (1 μM) seemed to affect the electrotactic bias of DAOY cells (Figure 32). However, the outward growth of each frontier was greatly diminished relative to non-inhibitor controls, yet since the electrotactic bias was still in place, this could merely be due to a diminished source of general growth signal from the ErbB receptors.

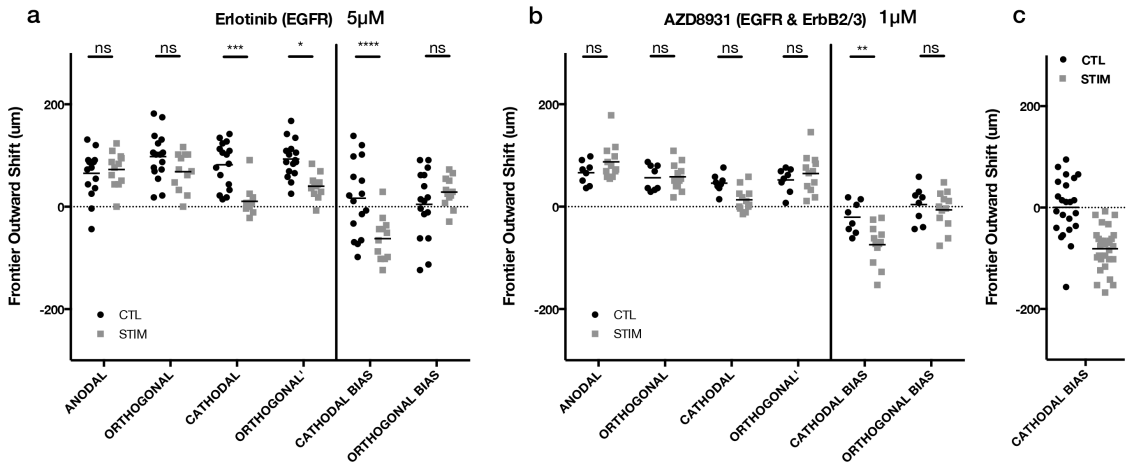

Figure 32. ErbB inhibitors for DAOY cells. 24h hours after dcEF (stim) or controls without dcEF (CTL) (a) Erlotinib (5 μM) ***p=0.0004, *p=0.0127, ****p<0.0001, ns=not significant (b) AZD6931 (1 μM) **p=0.0014, ns=not significant (c) DAOY data without inhibitor compounds, redisplayed from section 2.3.6. Two-way ANOVA, Holm-Sidak post-hoc. Mean±SEM shown.

The U87mg cells appeared to be unaffected by EGFR inhibition, however, the cellular aggregates grew no differently than controls with the pan-ErbB inhibitor AZD8931 (1 μM), and had lost their cathodal bias entirely (Figure 33). Testing both ErbB inhibitors at 10x increased doses, yielded the same effect (Figure 34).

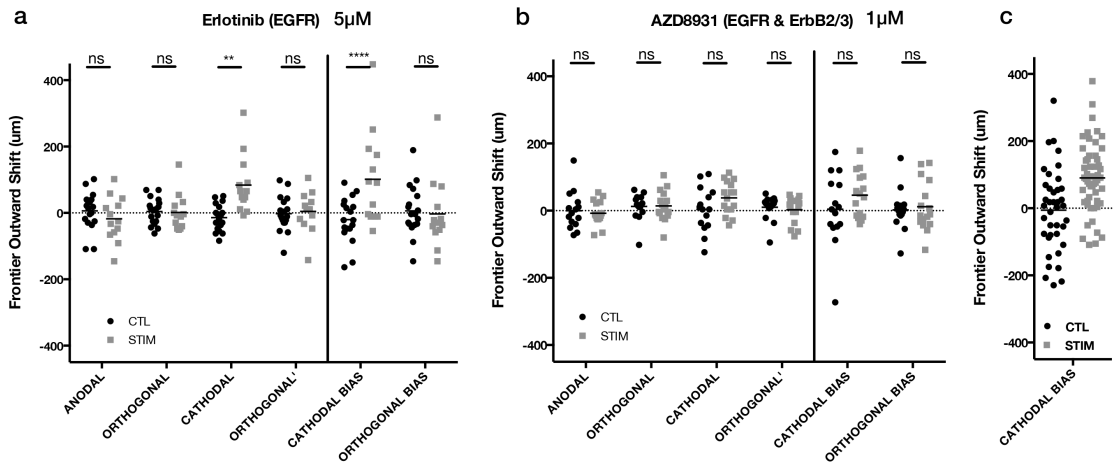

Figure 33. ErbB inhibitors for U87mg cells. 24h hours after dcEF (stim) or controls without dcEF (CTL) (a) Erlotinib (5 μM) **p=0.0016, ****p<0.0001, ns=not significant (b) AZD6931 (1 μM) ns=not significant (c) U87mg data without inhibitor compounds, redisplayed from section 2.3.6. Two-way ANOVA, Holm-Sidak post-hoc. Mean±SEM shown.

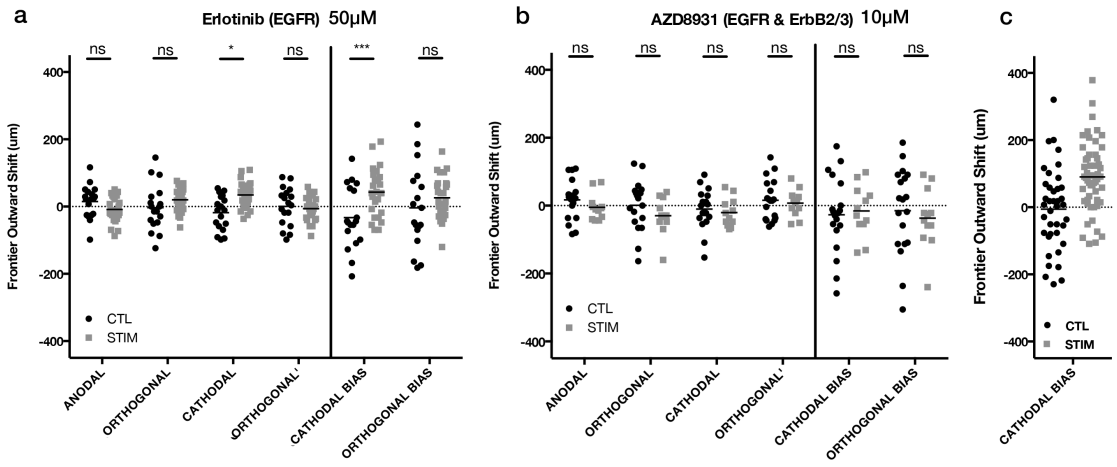

Figure 34. ErbB inhibitors at increased dosage for U87mg cells. 24h hours after dcEF (stim) or controls without dcEF (CTL) (a) Erlotinib (50 μM) *p=0.0278, ***p=0.0004, ns=not significant (b) AZD6931 (10 μM) ns=not significant (c) U87mg data without inhibitor compounds, redisplayed from section 2.3.6. Two-way ANOVA, Holm-Sidak post-hoc. Mean±SEM shown.

We were unable to procure an inhibitor for ErbB3-specific inhibition, but we did attempt to determine whether ErbB2-specific inhibition resulted in loss of electrotactic bias, and surprisingly, it did (Figure 35a). This is notable, because U87mg cells are generally considered ErbB2-negative or ErbB2-weakly-expressing [Mineo, 2004]. We hypothesized that perhaps the U87mg cells, as some tumor cells have been shown to do previously [Pickl, 2009], up-regulated their ErbB2 expression when they were plated in 3D or as aggregates, which would also explain the tempered electrotactic response we observed for 2D-dispersed scenarios. This was not the case however, as flow cytometry of the U87mg in 2D vs. 3D, dispersed vs. aggregated, yielded no change in ErbB2 expression relative to an isotype negative control, and did not approach the signal of

ErbB2+ MCF7 breast cancer cells (see Appendix C, Figure 45). Lastly, inhibition of EGFR and ErbB4 did not impact U87mg electrotactic bias (Figure 35b).

It remains unclear how such a low expression of ErbB2 in U87mg cells could affect their ability to electrotax, and further it is surprising that no other tested ErbB family member was associated with this process, as ErbB2 homodimers are orphan receptors with no known ligand or functional input [Brennan, 2000]. Overexpression of either ErbB2 or ErbB3 can lead to an increased anodal electrotaxis in breast tumor cells, though it has yet to be shown what dimerization was occurring in those cells [Pu, 2007]. While ErbB3 was not directly tested in our assays, U87mg cells are known to have little or no ErbB3 expression [Carrasco-Garcia, 2011], and given that inhibition of EGFR and ErbB4 had no impact on electrotaxis, the evidence points to a ErbB2-specific pathway. Further study will be required in order to better piece apart: (a) whether the ErbB2 proteins are re-coordinated on the cell surface in response to a dcEF; and (b) what forms of dimerization are occurring.

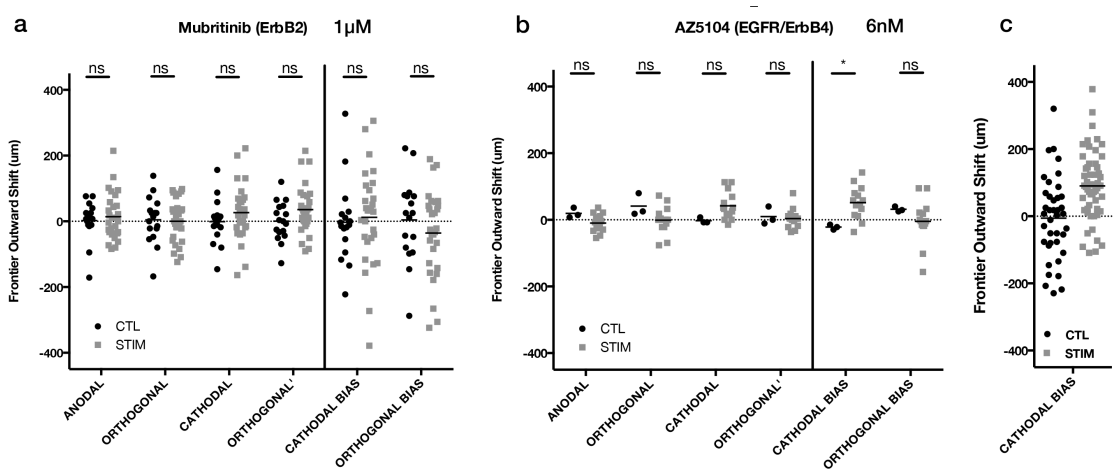

Figure 35. Additional ErbB inhibitors for U87mg cells. 24h hours after dcEF (stim) or controls without dcEF (CTL) (a) Mubritinib (1 μM) ns=not significant (b) AZ5104 (6 nM) *p=0.0386, ns=not significant (c) U87mg data without inhibitor compounds, redisplayed from section 2.3.6. Two-way ANOVA, Holm-Sidak post-hoc. Mean±SEM shown.

4.3.3 Additional inhibition targets

We tested a few additional inhibitors for various targets that were found to be differentially-regulated after dcEF in the RNA-SEQ data. Both the Src and HGF pathways are of interest in that their activity would support a chemotactic-overlap hypothesis for electrotaxis. The Src/Abl pathway acts upstream of PI3K and receives input from a number of receptor molecules including EGFR, signals of oxidative stress, and growth factors [Greuber, 2013]. Our RNA-SEQ analyses produced several significantly enriched gene sets for ERK signaling, which has also been previously implicated in electrotaxis [Tsai, 2013], thus we have also chosen, PD0325901, a MEK inhibitor that acts upstream of ERK signaling.

We saw numerous gene sets across both cell lines suggesting that HGF and VEGF signaling we differentially regulated under dcEFs thus we have included an ATP-competitive inhibitor of both HGFR and VEGFR (mostly for MET, KDR, TIE2, and FLT4). We also saw much evidence pointing to dcEF-induced RNA localization and splicing. While inhibition of RNA localization is beyond the scope of simple pharmacological inhibition, we were able to perform a cursory test on general inhibition of RNA splicing with isoginkgetin [O'Brien, 2008].

Both inhibition of MEK with PD0325901 (500 nM) and Src/Abl with Bosutinib (1 μM) in DAOY aggregates led to a loss of significant different in anodal bias relative to controls, however, this may be a technical/statistical artifact, because all but two of the replicates for each had an anodal bias (Figure 36). Inhibition of the pre-spliceosome with isoginkgetin (33 μM) had no effect on DAOY electrotactic bias, nor did inhibition of HGF/VEGF signaling with Foretinib (500 nM). Since no chemotactic signaling pathway we inhibited was observed to have an effect on DAOY electrotactic bias, we wondered if the mechanism was instead driven by chemorepulsion on the cathodal side. However, this hypothesis was quickly nullified when inhibition of ROCK1/2 with Y-27632 (10 μM) led to a 2.8-fold increase in anodal bias.

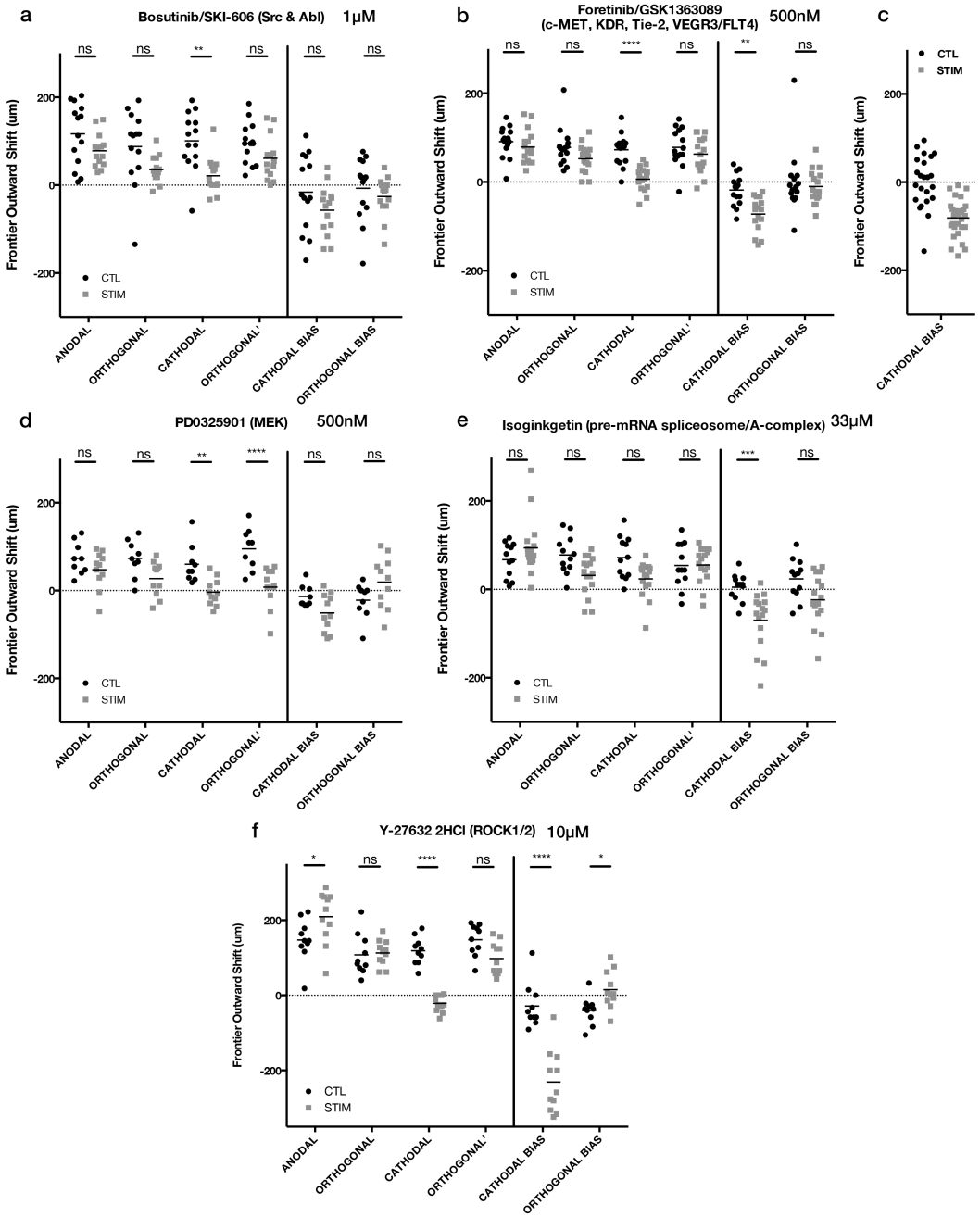

Figure 36. Additional inhibitors for DAOY cells. 24h hours after dcEF (stim) or controls without dcEF (CTL) (a) Bosutinib (1 μM) **p=0.0035, ns=not significant (b) Foretinib (500 nM) **p=0.0016, ****p<0.0001, ns=not significant (c) DAOY data without inhibitor compounds, redisplayed from section 2.3.6. (d) PD0325901 (500 nM) **p=0.0058, ****p<0.0001, ns=not significant (e) Isoginkgetin (33 μM) ***p=0.0006, ns=not significant (f) Y-27632 (10 μM) *p=0.0279 (anodal), *p=0.0472 (orthogonal bias), ****p<0.0001, ns=not significant. Two-way ANOVA, Holm-Sidak post-hoc. Mean±SEM shown.

For the U87mg aggregates, of the four additional inhibitors we tested only Src/Abl inhibition with Bosutinib (1 μM) had any effect on the overall cathodal bias (Figure 37). Though, this is particularly interesting with respect to our findings with ErbB inhibition, as Src is known to interact with ErbB2 and ErbB3 complexing [Ishizawar, 2007]. Yet Src and Abl are, like mTOR and AKT, broadly connected to signaling pathways for many cellular functions, and whether Src, ErbB2/3, mTOR, AKT, and PI3Kγ actually forms a mechanistic network in U87mg electrotaxis requires further confirmation.

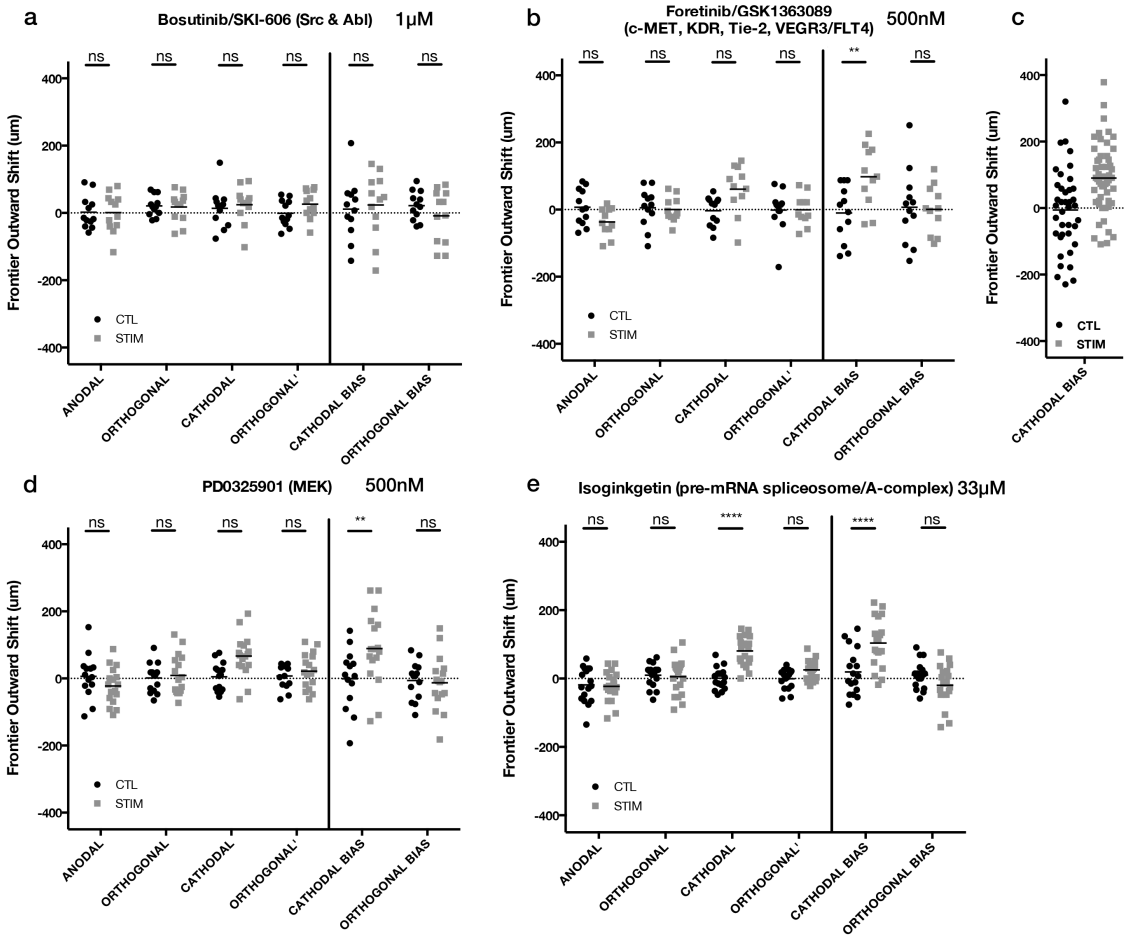

Figure 37. Additional inhibitors for U87mg cells. 24h hours after dcEF (stim) or controls without dcEF (CTL) (a) Bosutinib (1 μM) ns=not significant (b) Foretinib (500 nM) **p=0.0013, ns=not significant (c) U87mg data without inhibitor compounds, redisplayed from section 2.3.6. (d) PD0325901 (500 nM) **p=0.0015, ns=not significant (e) Isoginkgetin (33 μM) ****p<0.0001, ns=not significant. Two-way ANOVA, Holm-Sidak post-hoc. Mean±SEM shown.

4.4 Conclusion

Overall, while DAOY cells did not appear to be affected by a loss of PI3K, mTOR, IGF, or AKT signaling, the U87mg cellular aggregates lost their cathodal bias when PI3Kγ was inhibited, yet other PI3Ks (α, β, and δ) do not appear to be regulating

electrotaxis. mTOR and AKT also appear to be part of the electrotactic response in U87mg cells, though if and how they are connected to PI3Kγ requires further study, as well as determining what input to PI3Kγ is driving the response and why it induces a cathodal response in these particular cells. mTOR and AKT are known to be connected signaling pathways, but both also have broad signaling connectivity across the spectrum of cellular function, thus confirming how the electrotactic signal propagates through the PI3K/AKT/mTOR network also demands further study.

The ErbB pathway also appeared to be required for electrotaxis, as inhibition of ErbB2 and potentially ErbB3 was able to attenuate the cathodal bias to no different than controls without dcEFs. This was surprising as ErbB2 expression in U87mg cells is known to be low, and we did not see an impact to this based on our variety of plating formats. Which particular hetero- and homo-dimers of ErbB2 and ErbB3 are specifically involved requires further study, as well as whether these receptors are undergoing electrophoresis and asymmetrically expressed, as EGFR was found to be in previous electrotactic studies [Wu, 2013].

None of our additional four inhibitors for Src/Abl, MEK, pre-spliceosome, or HGF/VEGF signaling seemed to have much effect on DAOY cells. However, the inhibition of ROCK1/2 did dramatically increase the DAOY anodal bias, suggesting that future studies should examine the balancing of various GTPases as a way to attenuate or enchance electrotaxis in these cells.

For the U87mg aggregates, only the Src/Abl inhibitor was able to remove the cathodal bias. This interesting in that, although Src is broadly connected to many cellular

functions, it is known to be connected to the other targets we verified to be in part essential for U87mg electrotaxis.

CHAPTER 5. FUTURE DIRECTIONS

The ability to harness and to better understand electrotaxis could have broad implications for many biomedical enterprises including advances primarily in control of cellular growth for tissue engineering, wound healing, and cancer therapy. Further, with the rising ubiquity of electroceuticals, and therein the rise in available technologies, and methods, and the overall increase in interest in electrical modes of therapy, holds promise that we may soon see clinical applications of electrotaxis. There is however, much work to move our understanding of electrotaxis forward, to a level commensurate with clinically-viable technologies.

Several studies could immediately follow from the work we have presented in this thesis. The PI3K, AKT, mTOR, and Src signaling pathway are densely connected to many cellular processes, and the more we can understand their interconnectivity under dcEFs, the better we can hone in on the particular systems that can sense dcEFs, and those that can translate that signal into persistent direction motility. Additionally, the question of how the ErbB2, and possibly the ErbB3 receptors fit into this. Are they acting as electrical sensors, possibly altering their confirmation or complexing based on transmembrane voltage? Are the relevant signaling ligands being electrophoresed, or are the receptors? Additionally, in our RNA-SEQ data we observed many other potential membrane-bound effectors that could also be involved in this process including TGFB, WNT, and NGF and are ripe for successive inhibition studies.

Overall a broader RNA-SEQ would be helpful to enable a better refinement of the search for electrotactic mechanisms. We only performed RNA-SEQ using the DAOY and U87mg and using bulk multi-cellular samples. The addition of more cell lines, and/or the inclusion of primary tumor samples would enable improved differential analysis, to help hone in on conserved electrotaxis mechanisms, as well as to enable more clustering-based approaches to find differentially expressed gene sets that map to particular types of observed electrotactic responses. Single-cell RNA-SEQ may also be of interest, particularly for segmenting population-level studies, as it was seen in Cohen, et al.,that leader and follower cells both responded differently to dcEFs [Cohen, 2014].

There also remains the yet unanswered challenge of how either a material substrate, or plating dimensionality drives different electrotaxis responses. This will be important, especially if electrotaxis ever finds its use in clinical applications, as the mapping of how an explant behaves *in vitro,* must reliably correspond to its expected patient-*in situ*, lest the tumor be driven in the wrong direction.

When considering an actual therapeutic application of electrotaxis, a few truly powerful concepts could be realized. If it is the case that (i) cancer cells selectively respond to electrotaxis more than noncancerous cells; and (ii) this process invokes changes in specific signaling pathways; then electrotaxis could be a path to selective chemotherapeutics or a way to increase chemosensitivity. This however, depends largely on a more advanced molecular-biological understanding of electrotaxis for each target cell types, as well as the availability of therapeutic compounds that target those pathways.

Electrotaxis could also be used therapeutic with the concept of *exvasion*, introduced by Jain, et al., through the use of physical conduits, containing a particular microtopology that encourages exvasion toward a specified site [Jain, 2014]. dcEFs could be applied in integration with these conduits, or perhaps even as electrode montages that don't require any particular topology to exvade tumor cells. One could even envision electrode montages that issue a lensed electrical field that could aggregate a diffuse tumor toward a surgical site. Or perhaps such an electrotaxis lens could be turned inward on the tumor, forcing its invasive growth toward perpetual necrosis and implosion.

There is however one safety concern that must be addressed before dcEFs that provide electrotactic cues can be applied in long-term use. Eventually any stable dcEF source will produce non-faradaic charge transfer, an electrochemical phenomenon that is known to cause many non-biocompatible byproducts [Merrill, 2005]. In our experiments we use exchangeable salt-bridges to mitigate this issue, but continuously having to replace part of a medical implant every day could be infeasible. One way to circumvent this issue would be to use an asymmetric, biphasic dcEF, which has been previously shown effective at producing electrotaxis of neural precursor cells [Babona-Pilipos, 2015]. In fact, modulating the dcEF may be add even more therapeutically-desirous effects, as was seen in Hart, et al., where adding alternating current to a dcEF produced an enhancement in keratinocyte electrotaxis [Hart, 2013]. Or perhaps the biphasic modulation frequency could be set at a tumor-treating field frequency?

Eventually, we envision a flexible, electroceutical modality, where electrotaxis and tumor-treating fields could be combined like a therapeutic synthesizer, consolidating tissue, while simultaneously exvading and treating (Figure 38)—a therapy where

treatment signals can be combined more facilely, precisely, and potentially more safely, than with multiple drug combinations. This is the future of electrotaxis for biomedicine.

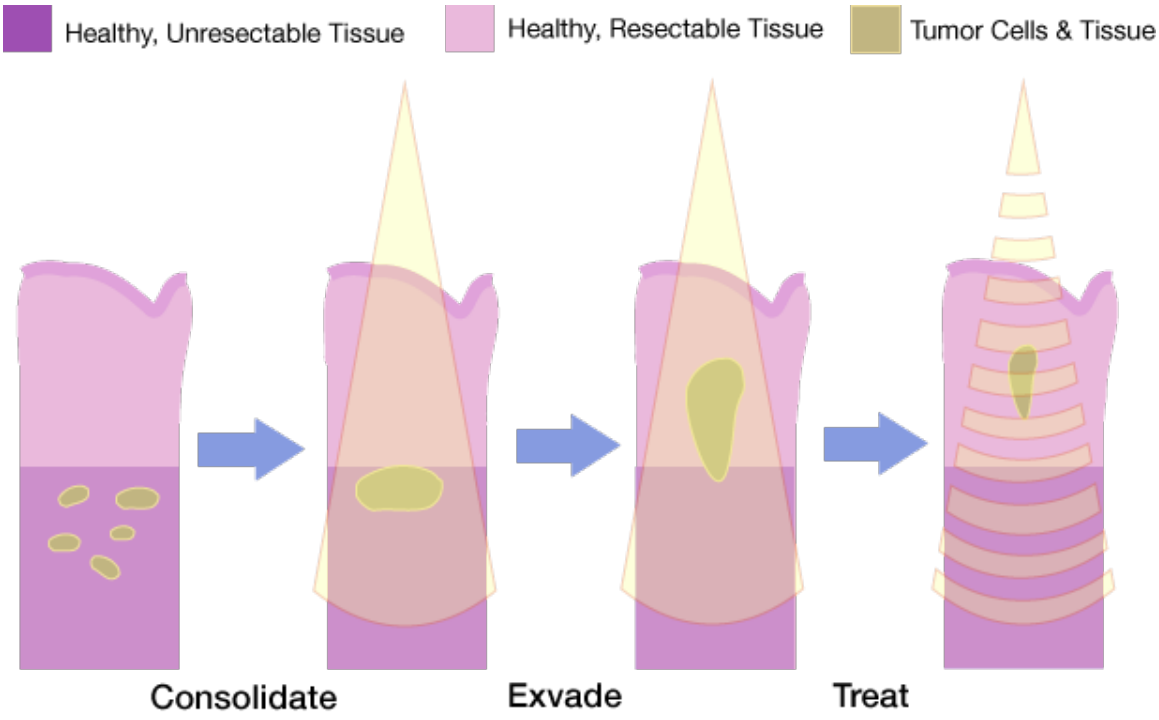

Figure 38. Conceptual diagram of an electrotaxis-based therapy for brain tumors.

APPENDIX A. QRT-PCR SUPPLEMENTAL INFORMATION

Table 7. Candidate Gene Assay Primers & Sequences

GENE	NCBI Refseq	Forward Primer	Reverse Primer
AKT1	NM_005163.2	CACACACTCACCGAGAACC	TCGTGGGTCTGGAAAGAGTA
CCL2	NM_002982.3	TAGCAGCCACCTTCATTCCC	CCTCTGCACTGAGATCTTCCTA
CDC42	NM_001791.3	GGTGGAGAACCATATACTCTTGG	GGATAACTCAGCGGTCGTAAT
EGFR	NM_005228.3	GCAGTGACTTTCTCAGCAACA	TTGGGACAGCTTGGATCACA
FGF2	NM_002006.4	TGCTAACCGTTACCTGGCTA	AAGAAACACTCATCCGTAACACA
FLT1	NM_001159920.1	TAGCTGGCAAGCGGTCTTAC	GCAGATTTCTCAGTCGCAGGTA
FRK	NM_002031.2	TGTCAAGCTGGGGAAACCA	TCCCATTGGTCCACGGTTTTA
FYN	NM_153047.1	GAGCCCATCTACATCGTCAC	TTCAGAGCTCTTCCTTCTCCA
IPCEF1	NM_001130700.1	TCAGAAGCCCAGGAGGAAA	GCATGGCCCAGATCTTTACA
MAPK1	NM_002745.4	TTGGTACAGGGCTCCAGAAA	TCTGCCAGAATGCAGCCTA
MAPK14	NM_001315.2	GGCTCCTGAGATCATGCTGAA	ACAGCTCGGCCATTATGCA
MAPK3	NM_002746.2	GAAGATCAGCCCCTTCGAACA	GCAGCAGGATCTGGATCTCC
MAPK8	NM_002750.2	TCTCCAACACCCGTACATCA	CCCTTTCATCTAACTGCTTGTCA
MMP1	NM_001145938.1	CACCTTCAGTGGTGATGTTCA	GCTGGACAGGATTTTGGGAA
MMP9	NM_004994.2	AGTGGCACCACCACAACA	GCAAAGGCGTCGTCAATCA

Table 7 (continued)

PIK3CA	NM_006218.2	CTGCAGTTCAACAGCCACAC	ACAGGTCAATGGCTGCATCA
PRKACA	NM_002730.3	AAGGAGACCGGGAACCACTA	AGGGTGTGTTCGATCTGTTTCA
PRKCA	NM_002737.2	ACCATCCGCTCCACACTAAA	AGTCGTCGGTCTTTGTCTGAA
PTEN	NM_000314.4	CCAGACATGACAGCCATCA	AGTCTTTCTGCAGGAAATCCC
RAC1	NM_018890.3	TCACCTATCCGCAGGGTCTA	GCCGAGCACTCCAGGTATTTTA
RHOA	NM_001664.2	GTGCCCACAGTGTTTGAGAA	TGTGTCCCACAAAGCCAAC
SCN1B	NM_000314.4	TTCACCGAGTGGACCTTCC	TCCAGCTGCAACACCTCA
SGK1	NM_001037.4	CTTGGGCTACCTGCATTCAC	TGTGTCCCTGTGAATCTAGCA
SOD2	NM_001024465.1	AGGAACGGGGACACTTACAA	TCAATCCCCAGCAGTGGAATA
VEGFC	NM_005429.2	GCCAACCTCAACTCAAGGAC	GCATGCATTGAGTCTTTCTCCA
HOUSEKEEPING GENES			
ACTB	NM_001101.3	CCAACCGCGAGAAGATGAC	TAGCACAGCCTGGATAGCAA
GAPDH	NM_002046.4	GAACGGGAAGCTTGTCATCAA	ATCGCCCCACTTGATTTTGG
IPO8	NM_001190995.1	TTCAGTGCAAAGGAAGGGGAA	ACCCCTCGAGTTAATCTCTCCA
RPL13A	NM_012423.3	GAGGCCCCTACCACTTCC	GCCGTCAAACACCTTGAGAC
SDHA	NM_004168.2	ACATCGGAACTGCGACTCA	TTCTTGCAACACGCTTCCC
TBP	NM_001172085.1	TGCCCGAAACGCCGAATATA	CGTGGTTCGTGGCTCTCTTA

Table 8. Motility Gene Assay Primers

NCBI Refseq	Symbol	NCBI Refseq	Symbol	NCBI Refseq	Symbol
NM_001102	ACTN1	NM_000875	IGF1R	NM_002859	PXN
NM_001104	ACTN3	NM_004517	ILK	NM_006908	RAC1
NM_004924	ACTN4	NM_000885	ITGA4	NM_002872	RAC2
NM_005722	ACTR2	NM_002211	ITGB1	NM_002890	RASA1
NM_005721	ACTR3	NM_000211	ITGB2	NM_002906	RDX
NM_005163	AKT1	NM_000212	ITGB3	NM_000539	RHO
NM_001663	ARF6	NM_002314	LIMK1	NM_001664	RHOA
NM_004309	ARHGDIA	NM_002745	MAPK1	NM_004040	RHOB
NM_003899	ARHGEF7	NM_000245	MET	NM_175744	RHOC
NM_006340	BAIAP2	NM_004995	MMP14	NM_005168	RND3
NM_014567	BCAR1	NM_004530	MMP2	NM_005406	ROCK1
NM_005186	CAPN1	NM_004994	MMP9	NM_014631	SH3PXD2A
NM_001748	CAPN2	NM_002444	MSN	NM_005417	SRC
NM_001753	CAV1	NM_005964	MYH10	NM_003150	STAT3
NM_001791	CDC42	NM_002473	MYH9	NM_003174	SVIL
NM_005507	CFL1	NM_006097	MYL9	NM_000660	TGFB1
NM_016823	CRK	NM_053025	MYLK	NM_003255	TIMP2

Table 8 (continued)

NM_000757	CSF1	NM_002576	PAK1	NM_006289	TLN1
NM_005231	CTTN	NM_005884	PAK4	NM_003370	VASP
NM_005219	DIAPH1	NM_005022	PFN1	NM_003373	VCL
NM_001935	DPP4	NM_006218	PIK3CA	NM_003376	VEGFA
NM_001963	EGF	NM_002659	PLAUR	NM_003380	VIM
NM_005228	EGFR	NM_002660	PLCG1	NM_003931	WASF1
NM_001008493	ENAH	NM_002662	PLD1	NM_006990	WASF2
NM_003379	EZR	NM_002737	PRKCA	NM_003941	WASL
NM_004460	FAP	NM_000314	PTEN	NM_003387	WIPF1
NM_002006	FGF2	NM_005607	PTK2		
NM_000601	HGF	NM_004103	PTK2B		
NM_000618	IGF1	NM_002827	PTPN1		

HOUSEKEEPING GENES

NM_004048	B2M
NM_000194	HPRT1
NM_012423	RPL13A
NM_002046	GAPDH
NM_001101	ACTB

APPENDIX B. RNA-SEQ SUPPLEMENTAL INFORMATION

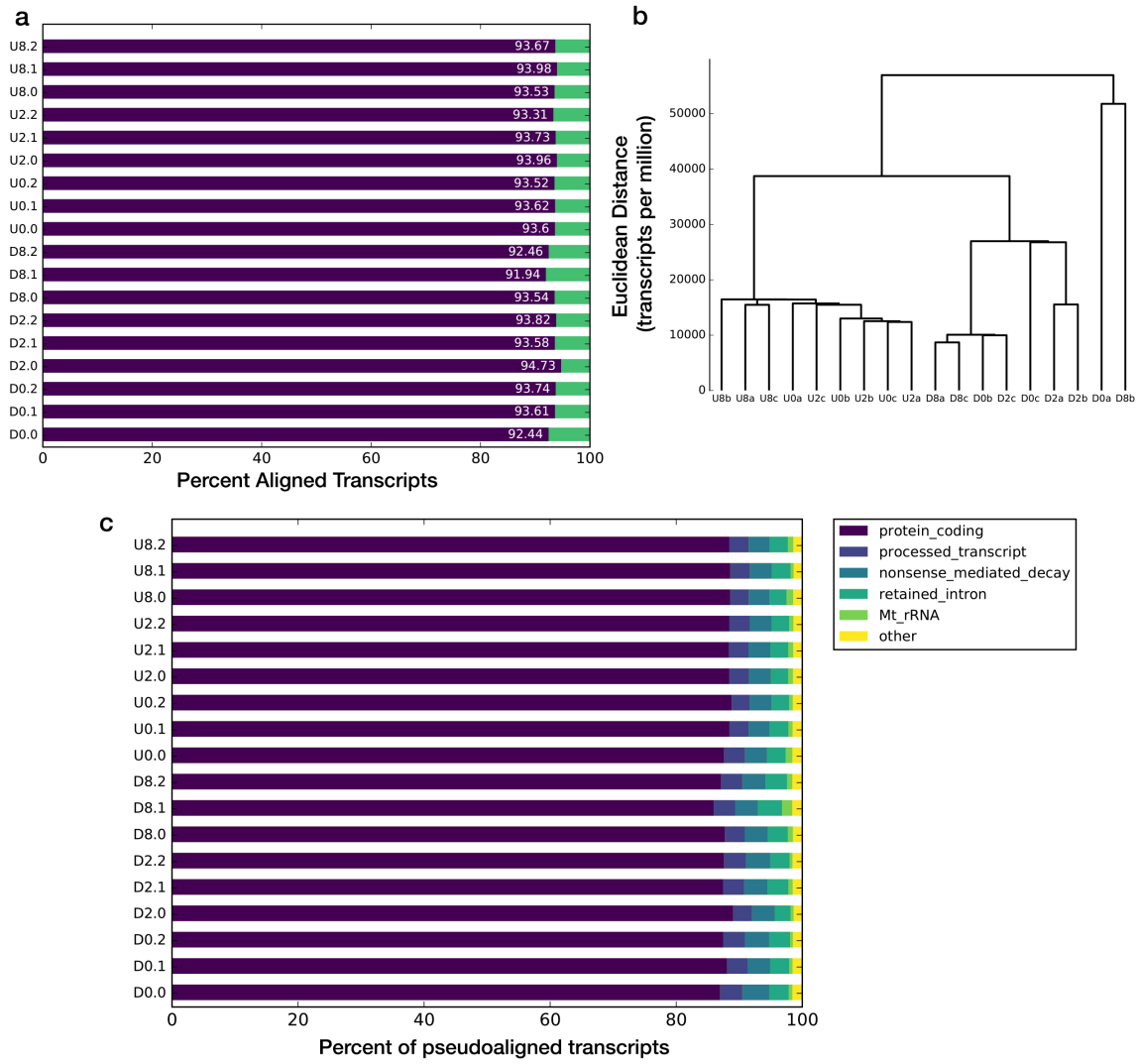

Figure 39. Pseudo-alignment performance. (a) Percent of each sample aligned to a transcript in the reference. (b) Dendrogram, showing clustering of the expression profiles across input samples using the Euclidean distance comparing all pseudo-aligned transcripts. (c) Percent of pseudo-aligned transcripts that were aligned to a particular GENCODE biotype.

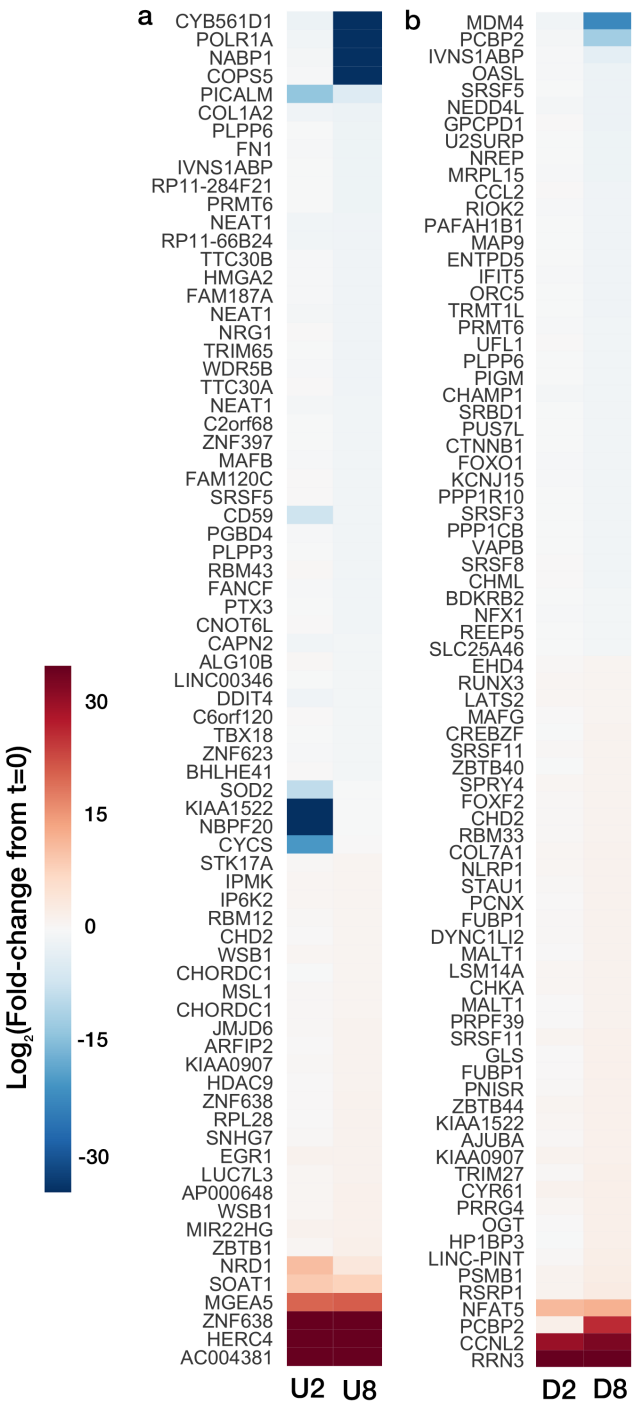

Figure 40. Fold-change of most significantly differentially expressed transcripts. Comparing (a) U87mg, or (b) DAOY differentially expressed genes for 2h, or 8h of dcEF relative to 0h unexposed controls (U=U87mg, D=DAOY). Not all differentially expressed transcripts are shown, as Daoy significance cutoff was set to $p<0.001$ for improved readability.

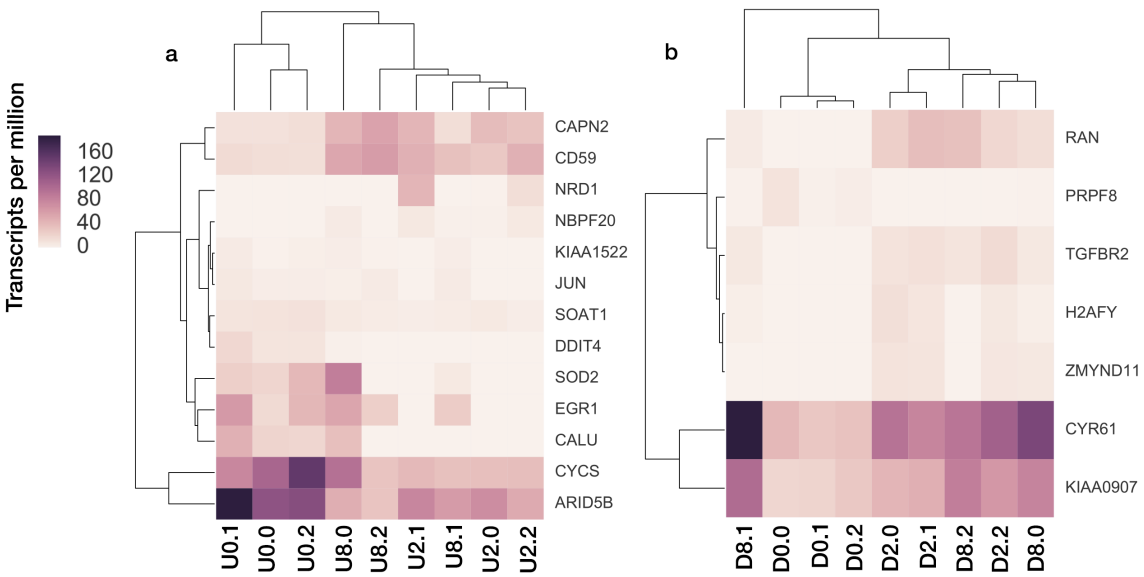

Figure 41. Clustermaps for transcripts per million of differentially expressed transcripts after 2h. Transcripts per million are shown for (a) U87mg and (b) Daoy cells after 2h dcEF exposure relative to 0h unexposed controls. Each column represents transcripts from a single replicate sample (U=U87mg, D=DAOY).

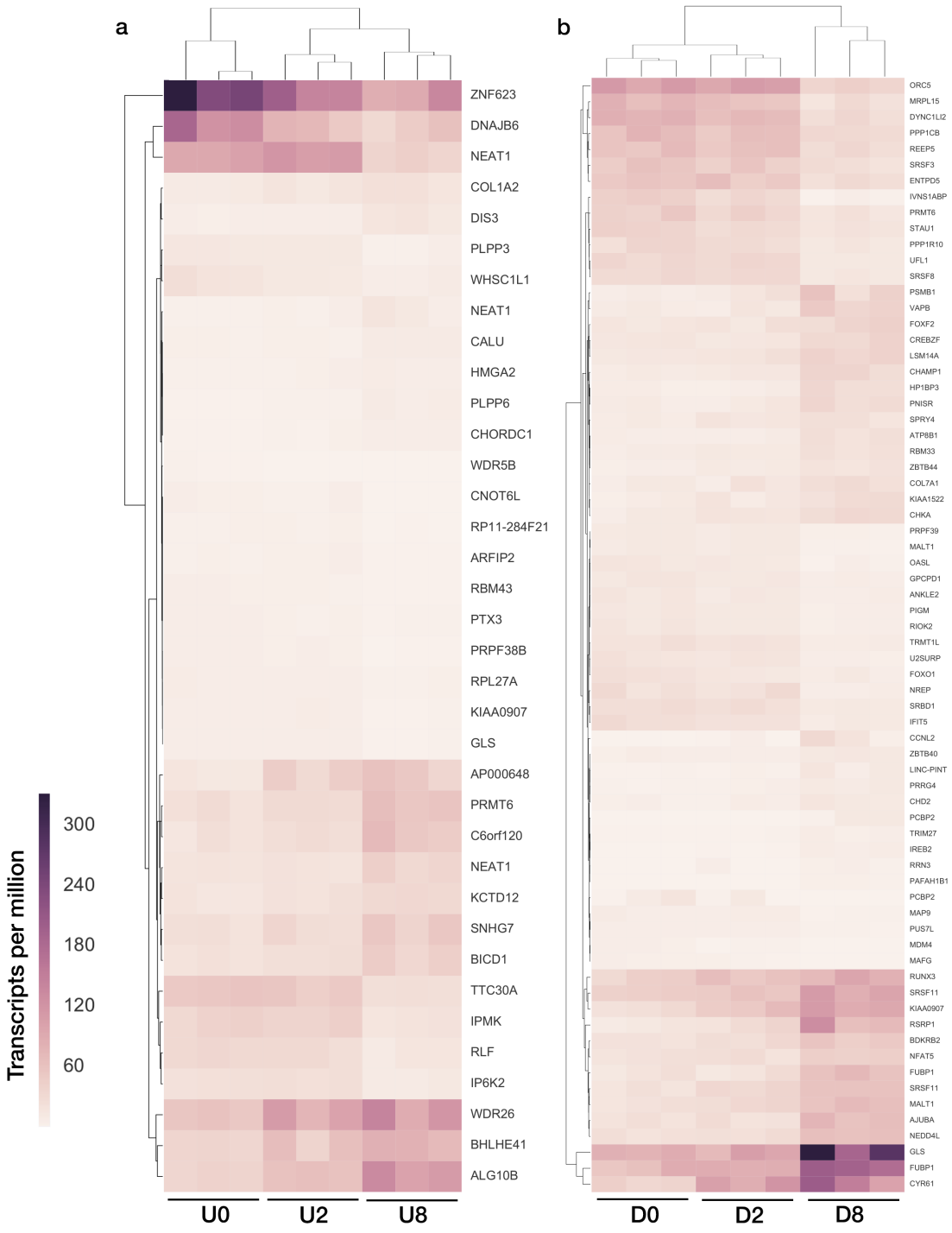

Figure 42. Clustermaps for transcripts per million of differentially expressed transcripts after 8h. Transcripts per million are shown for (a) U87mg and (b) Daoy cells after 8h dcEF exposure relative to 0h unexposed controls. Each column represents transcripts from a single replicate sample (U=U87mg, D=DAOY). Not all differentially expressed transcripts are shown, as Daoy significance cutoff was set to $p<0.0005$ and U87mg to $p<0.005$ for improved readability.

Table 9. Selected over-represented pathways for U87mg 8h

term ID	term name	p-value	ORA genes
GO:0060590	ATPase regulator activity	0.000281	DNAJA1, DNAJB6, HSPH1, DNAJB1, BAG3, DNAJB4
GO:0044260	cellular macromolecule metabolic process	0.000142	ZNF207, ZZZ3, HDAC9, POLR1A, JMJD6, ZNF638, DIS3, DNAJA1, WAC, DDX17, PPM1A, SRSF5, DNAJB6, EDRF1, RPL28, LUC7L3, WSB1, CHORDC1, TBX18, SEC24A, CPEB4, FN1, SFPQ, IVNS1ABP, SRSF11, RLF, RBM25, HSPH1, COPS5, LRIF1, BHLHE41, CKS2, NCOA3, VAPB, NDP, ZBTB1, CALU, RBM39, DNAJB1, PRPF38B, CNOT6L, MBNL2, CTTNBP2NL, ABL2, OGT, HERC4, HMGA2, UPF2, BICD1, BAG3, HNRNPDL, GTF2E1, NRG1, PPP1R15B, PLPP3, CAPN2, PTX3, RICTOR, STK17A, FRS2, RPL27A, FNTA, PPIC, OTUD3, BPTF, JMJD1C, MALT1, NAA16, SP3, NABP1, CHD2, ALG10B, CSTF3, FANCF, ZNF623, ZNF397, POFUT2, MSL1, MGEA5, NCOA6, PRMT6, MAFB, HSPA1B, ZBED6, TXNIP, PPP4R3B, DDX52
GO:0010467	gene expression	0.00000718	ZNF207, ZZZ3, HDAC9, POLR1A, JMJD6, ZNF638, TNPO1, DIS3, WAC, DDX17, PPM1A, SRSF5, DNAJB6, EDRF1, RPL28, LUC7L3, TBX18, CPEB4, FN1, SFPQ, IVNS1ABP, SRSF11, RLF, RBM25, HSPH1, COPS5, LRIF1, BHLHE41, CKS2, NCOA3, NDP, ZBTB1, RBM39, DNAJB1, PRPF38B, CNOT6L, MBNL2, OGT, HMGA2, UPF2, BICD1, BAG3, HNRNPDL, GTF2E1, NRG1, PPP1R15B, PLPP3, CAPN2, RICTOR, RPL27A, BPTF, JMJD1C, MALT1, NAA16, SP3, NABP1, CHD2, CSTF3, ZNF623, ZNF397, POFUT2, NCOA6, PRMT6, MAFB, HSPA1B, ZBED6, TXNIP, DDX52
GO:0016071	mRNA metabolic process	0.000457	JMJD6, DIS3, DDX17, SRSF5, RPL28, LUC7L3, SFPQ, SRSF11, RBM25, ZBTB1, RBM39, PRPF38B, CNOT6L, MBNL2, UPF2, RPL27A, CSTF3, HSPA1B, ZBED6
GO:0010468	regulation of gene expression	0.0000855	ZNF207, ZZZ3, HDAC9, POLR1A, JMJD6, ZNF638, TNPO1, DIS3, WAC, DDX17, PPM1A, SRSF5, DNAJB6, EDRF1, RPL28, TBX18, CPEB4, FN1, SFPQ, RLF, RBM25, HSPH1, COPS5, LRIF1, BHLHE41, CKS2, NCOA3, NDP, ZBTB1, RBM39, DNAJB1, CNOT6L, MBNL2, OGT, HMGA2, UPF2, BAG3, HNRNPDL, GTF2E1, NRG1, PPP1R15B, PLPP3, RICTOR, RPL27A, BPTF, JMJD1C, MALT1, NAA16, SP3, CHD2, ZNF623, ZNF397, POFUT2, NCOA6, PRMT6, MAFB, HSPA1B, ZBED6, TXNIP

Table 10. Selected over-represented pathways for DAOY 8h

term ID	term name	p-value	ORA genes
GO:0044260	cellular macromolecule metabolic process	1.2E-09	IBTK, MAP3K14, PAFAH1B1, PSMB1, ZNF207, RNF216, MBTPS2, UFL1, RUNX3, ZIC2, NEDD4L, PTCD2, CUL1, RIOK2, SPEN, ARFGEF1, JMJD6, TRIB2, DAZAP1, DERL2, NUAK1, ZNF638, POLD3, UBE2K, UBE2D4, RIF1, PUM3, ATP8B1, CYLD, RRN3, USP40, NFX1, PPP1R15A, MMP2, PAPOLA, OSBPL8, NLRP1, PSMD5, BTAF1, WAC, DDX17, PPM1A, SRSF5, PABPN1, CSTF1, NFAT5, EHD4, GABPB1, IKBKB, DNAJC2, MET, DNAJB6, AHR, RPL28, CCL2, PEX12, EFTUD2, WSB1, CHORDC1, RNF141, CBL, METAP2, SRSF3, FBXL4, PTP4A1, COL7A1, CBLB, COMMD2, KLHL24, EIF4G1, RAP1A, SFPQ, IVNS1ABP, PRDM2, TROVE2, SRSF11, TSNAX, KLHL12, CD46, RPA2, ANKRD13C, CPSF3, KBTBD7, TRMT1L, LRIF1, HNRNPA2B1, MED13L, BHLHE41, NMI, AGO2, VAPB, SRSF6, AHNAK, HP1BP3, ATF4, PUS7L, AJUBA, DTD2, ARHGEF6, ASH2L, SNX9, RBM39, DNAJB1, RAN, H3F3B, UNK, CCNA1, SWAP70, PRPF38B, DMTF1, TGFBRAP1, IREB2, TRA2B, SKIL, FOXF2, FLOT1, CREBZF, MRPL15, PPIG, CNOT6L, SBNO1, PARN, CLTC, CSNK1D, EPHA2, CYR61, PIGM, TARS2, PIK3R1, RNF44, OGT, ERLIN2, UHRF2, LATS2, VEGFC, FOXO1, NR4A2, GTF2E1, IMPACT, FZD7, UBE2Z, PLPP3, OMA1, FUBP1, PEA15, MSX1, CGGBP1, U2SURP, PGGT1B, CASP3, EN2, ORC5, FASTK, METTL2B, KIAA1958, KBTBD6, TAF1D, ZNF143, RIMKLB, CLPX, CRK, KMT2D, CTNNB1, BDKRB2, MAP2K1, SDC2, ZEB2, KLF13, HNRNPA3, SOCS5, PIK3CD, ATF7IP, MALT1, BNC2, CHD2, ATR, ALG10B, CDC26, ANKLE2, THAP5, TCEAL8, EWSR1, ZNF623, TOB2, ZBTB40, UBE2G2, MAFF, PRPF39, HEXIM1, POFUT2, ENTPD5, TET3, SPRY4, SEMA4D, AGRN, MSL1, ZBTB44, CD55, MAFG, PCBP2, IPP, MCMBP, ZNF181, MGEA5, DDX39B, BAZ1A, MDM4, STK39, TTC37, PRMT6, CHML, PBX2, MRPS18B, TRIM27, LGR4, STK38L, PPP1CB, CCNL2, MRPS6, USP51, LSM14A, SRSF8, RBM8A, GTF2H5, KMT2B, NEFL
GO:0033554	cellular response to stress	0.000482	PAFAH1B1, PSMB1, MBTPS2, UFL1, CUL1, DERL2, NUAK1, POLD3, UBE2K, RIF1, PPP1R15A, PSMD5, WAC, IKBKB, DNAJC2, MET, DNAJB6, CCL2, CHORDC1, CBL, EIF4G1, SFPQ, MTR, RPA2, PYROXD1, VAPB, STAU1, HP1BP3, ATF4, AJUBA, ARHGEF6, ASH2L, DNAJB1, GSTM3, SKIL, FLOT1, CNOT6L, EPHA2, PIK3R1, ERLIN2, FOXO1, NR4A2, IMPACT, FZD7, PEA15, MSX1, CASP3, CRK, CTNNB1, BDKRB2, MAP2K1, ZEB2, SOCS5, CHD2, ATR, ZBTB40, UBE2G2, CASP4, TXNRD1, DDX39B, MDM4, STK39, PRMT6, USP51, GTF2H5, NEFL
GO:0051236	establishment of RNA localization	0.0447	RIOK2, SRSF5, PABPN1, SRSF3, SRSF11, CPSF3, HNRNPA2B1, SRSF6, RAN, FLOT1, HNRNPA3, ATR, DDX39B, RBM8A

Table 10 (continued)

GO:0010467	gene expression	1.23E-08	PSMB1, ZNF207, MBTPS2, UFL1, RUNX3, ZIC2, NEDD4L, PTCD2, RIOK2, CNN2, SPEN, RAB27A, JMJD6, DAZAP1, ZNF638, RIF1, PUM3, ATP8B1, CYLD, RRN3, NFX1, PPP1R15A, PAPOLA, PSMD5, BTAF1, WAC, DDX17, PPM1A, SRSF5, PABPN1, CSTF1, NFAT5, GABPB1, IKBKB, DNAJC2, MET, DNAJB6, AHR, RPL28, EFTUD2, RNF141, CBL, METAP2, SRSF3, COMMD2, EIF4G1, SFPQ, IVNS1ABP, PRDM2, TROVE2, SRSF11, TSNAX, CD46, CPSF3, TRMT1L, LRIF1, HNRNPA2B1, MED13L, BHLHE41, NMI, AGO2, SRSF6, AHNAK, HP1BP3, ATF4, PUS7L, AJUBA, DTD2, ASH2L, RBM39, DNAJB1, RAN, H3F3B, UNK, CCNA1, PRPF38B, DMTF1, TGFBRAP1, IREB2, TRA2B, SKIL, FOXF2, CREBZF, MRPL15, PPIG, CNOT6L, SBNO1, PARN, CSNK1D, CYR61, TARS2, PIK3R1, OGT, ERLIN2, UHRF2, FOXO1, NR4A2, GTF2E1, IMPACT, FZD7, PLPP3, OMA1, FUBP1, MSX1, CGGBP1, CHCHD4, U2SURP, CASP3, EN2, FASTK, METTL2B, KIAA1958, TAF1D, ZNF143, CRK, KMT2D, CTNNB1, MAP2K1, ZEB2, KLF13, HNRNPA3, PIK3CD, ATF7IP, MALT1, BNC2, CHD2, THAP5, TCEAL8, EWSR1, ZNF623, TOB2, ZBTB40, MAFF, PRPF39, HEXIM1, POFUT2, TET3, SEMA4D, AGRN, ZBTB44, CD55, MAFG, PCBP2, ZNF181, DDX39B, BAZ1A, MDM4, TTC37, PRMT6, PBX2, MRPS18B, TRIM27, LGR4, CFI, PPP1CB, CCNL2, MRPS6, LSM14A, SRSF8, RBM8A, GTF2H5, KMT2B
GO:0016071	mRNA metabolic process	0.00109	PTCD2, SPEN, JMJD6, DAZAP1, PAPOLA, DDX17, SRSF5, PABPN1, CSTF1, RPL28, EFTUD2, SRSF3, EIF4G1, SFPQ, SRSF11, CPSF3, HNRNPA2B1, AGO2, SRSF6, ATF4, RBM39, PRPF38B, TRA2B, CNOT6L, PARN, U2SURP, HNRNPA3, PRPF39, PCBP2, DDX39B, TTC37, SRSF8, RBM8A, GTF2H5
GO:0000398	mRNA splicing, via spliceosome	0.00042	SPEN, JMJD6, DAZAP1, PAPOLA, DDX17, SRSF5, PABPN1, CSTF1, EFTUD2, SRSF3, SFPQ, SRSF11, CPSF3, HNRNPA2B1, SRSF6, TRA2B, U2SURP, HNRNPA3, PRPF39, PCBP2, DDX39B, RBM8A

Table 11. TRANSFAC transcription factor motifs significantly over-represented

U87 only	DAOY only	Both U87 & DAOY
EHF	AHR	CPBP
ELK1	BARHL2	DP1
ETS1	c-ETS1	E2F
ETV5	CDX2	E2F1
ETV7	CHD2	E2F4
FOXC1	CHurchill	EGR1
PSF	DP2	ELF1
	E2F3	ELF4
	ELF2	ER81
	ELK4	ETF
	ER71	FLI1
	ERG	RB
	ERM	SP2
	FOXJ2	SP6
	GABPA	ZF5
	GR	
	HMX3	
	HNF1B	
	HOXA13	
	HOXA9	
	LHX3	
	MSX1	
	NRF1	
	OCT4	
	PAX6	
	PET1	
	REX1	
	RNF96	
	SP1	
	SP3	
	TEF3	
	TEL1	
	ZBTB7C	

Table 12. All over-represented pathways for differentially expressed transcripts in {U87mg 8h} ∩ {DAOY 8h}

term ID	term name	p-value	ORA genes
GO:0008380	RNA splicing	0.0258	ZNF638, SRSF5, SFPQ, IVNS1ABP, SRSF11, RBM39, PRPF38B
GO:0010467	gene expression	0.0237	ZNF207, ZNF638, WAC, SRSF5, DNAJB6, RPL28, SFPQ, IVNS1ABP, SRSF11, LRIF1, BHLHE41, RBM39, DNAJB1, PRPF38B, CNOT6L, OGT, GTF2E1, PLPP3, MALT1, CHD2, ZNF623, POFUT2, PRMT6
GO:0016070	RNA metabolic process	0.0057	ZNF207, ZNF638, WAC, SRSF5, DNAJB6, RPL28, SFPQ, IVNS1ABP, SRSF11, LRIF1, BHLHE41, RBM39, DNAJB1, PRPF38B, CNOT6L, OGT, GTF2E1, PLPP3, MALT1, CHD2, ZNF623, PRMT6
TF:M02071_1	Factor: ETV7	0.0113	IP6K2, ZNF638, WAC, SRSF5, DNAJB6, RPL28, WSB1, CHORDC1, GLS, SFPQ, IVNS1ABP, LRIF1, BHLHE41, RBM39, DNAJB1, KIAA0907, CDR2, OGT, MALT1, ALG10B, ZNF623, FAM120C, C6ORF120, POFUT2, CHAMP1, PRMT6
TF:M07250_0	Factor: E2F-1	0.00492	ZNF207, IP6K2, ZNF638, GPATCH2L, WAC, SRSF5, DNAJB6, RPL28, WSB1, CHORDC1, GLS, SFPQ, IVNS1ABP, SRSF11, BHLHE41, RBM39, DNAJB1, KIAA0907, PRPF38B, CNOT6L, CDR2, OGT, GTF2E1, PLPP3, MALT1, ALG10B, ZNF623, FAM120C, C6ORF120, POFUT2, MSL1, CHAMP1, PRMT6, PLPP6

APPENDIX C. PHARMACOLOGICAL INHIBITION

SUPPLEMENTAL INFORMATION

Table 13. Literature and Data used to determine experimental doses for pharmacological inhibitors. Note, when available, prior data specific for U87mg or DAOY cells was used. *data from Sigma-Aldrich; †reported full target inhibition; ‡50 nM for HER2 IC50; NR: not reported

Drug	in vitro IC50 (from SelleckChem)	Previous in vitro use	Reference
Isoginkgetin	30 uM*	33um in HEK	O'Brien, 2008
AZD8931	4 nM	0.001-10 uM in various	Hickinson, 2010
OSI-906	1 uM†	0.02-0.8 uM in various	Mulvihill, 2009
Bosutinib	100 nM	250 nM in MDA	Vultur, 2008
KU-0063794	30 nM	5 uM in U373	Fan, 2010
MK-2206	NR	1-10uM in U87	Jin, 2013
Foretinib	0.4-165 nM	.5-2.5uM in DAOY	Faria, 2014
PD0325901	2-123 nM	0.1-1uM in various	See, 2012
LY294002	0.38-45 uM	20 uM in U87/U251	Li, 2013
BEZ235	75 nM	0.001-0.1uM in U87	Liu, 2009
Rapamycin	0.1nM-1uM	100 nM in U87	Takeuchi, 2005

Table 13 (continued)

Erlotinib	20 nM-20uM	1-10uM in U87	Fan, 2007
CZC24832	1.5uM	1 uM in Multiple myeloma cells	Piddock, 2017
Mubritinib	0.1uM-25uM	0.25-1 uM in AML cells	Ufkin, 2014
Y-27632	0.3-1uM	10 uM in DAOY	Coniglio, 2008
AZ5104	2.6-80 nM‡	3-80 nM in Lung Cancers	Cross, 2014

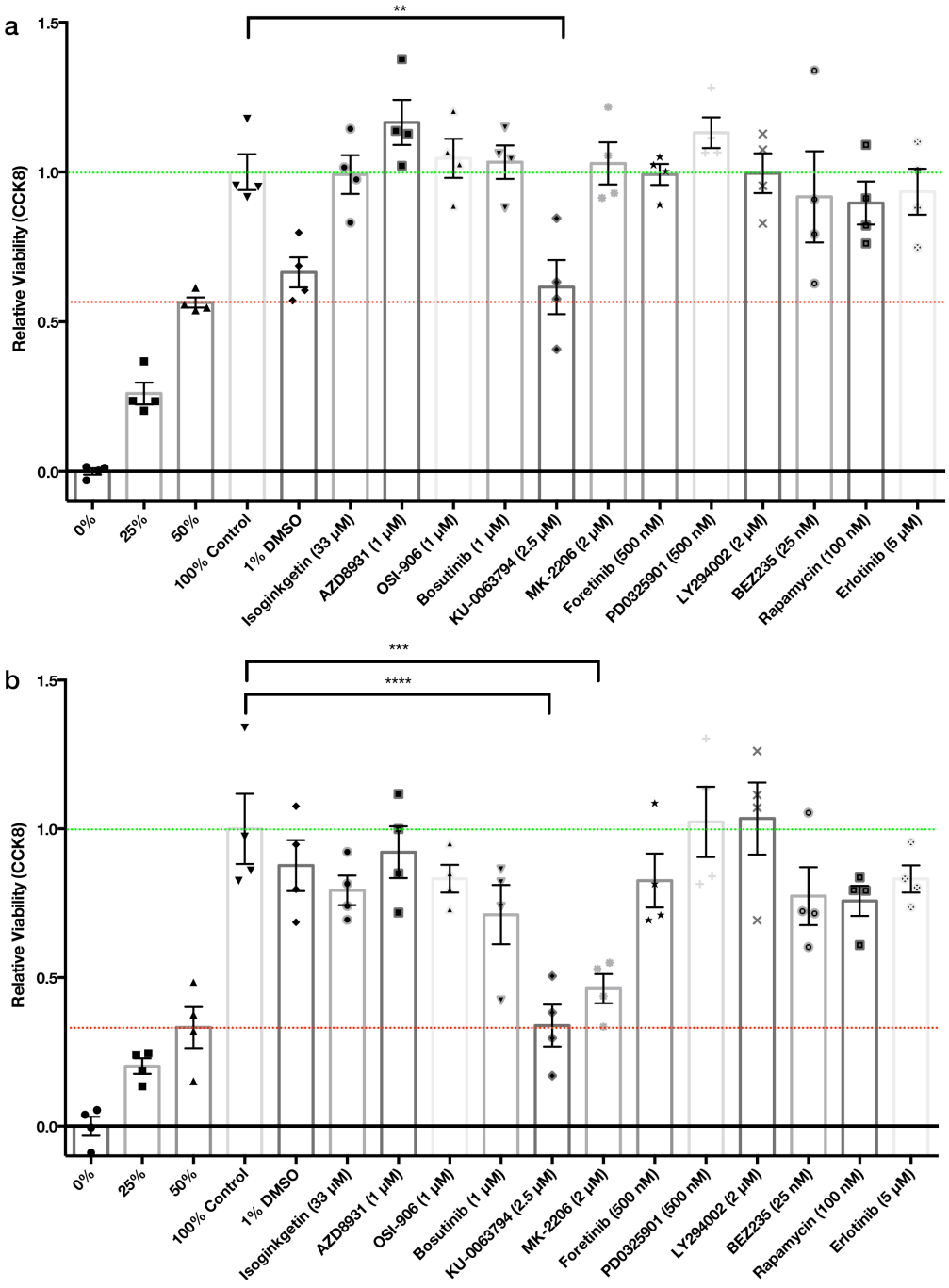

Figure 43. Viability Assessment with Cell-Counting Kit 8 Assay after addition of inhibitors. Viability after 24h exposure to various inhibitory compounds for (a) U87mg and (b) DAOY cells. **p=0.0032, ***p=0.0002, ****p<0.0001. 100% control represents 5000 cells initially plated, 50% 2500 cells, etc. 50%, 25%, and 0% were also significantly different than 100% controls, and 1% DMSO control was only significantly different for U87mg cells.

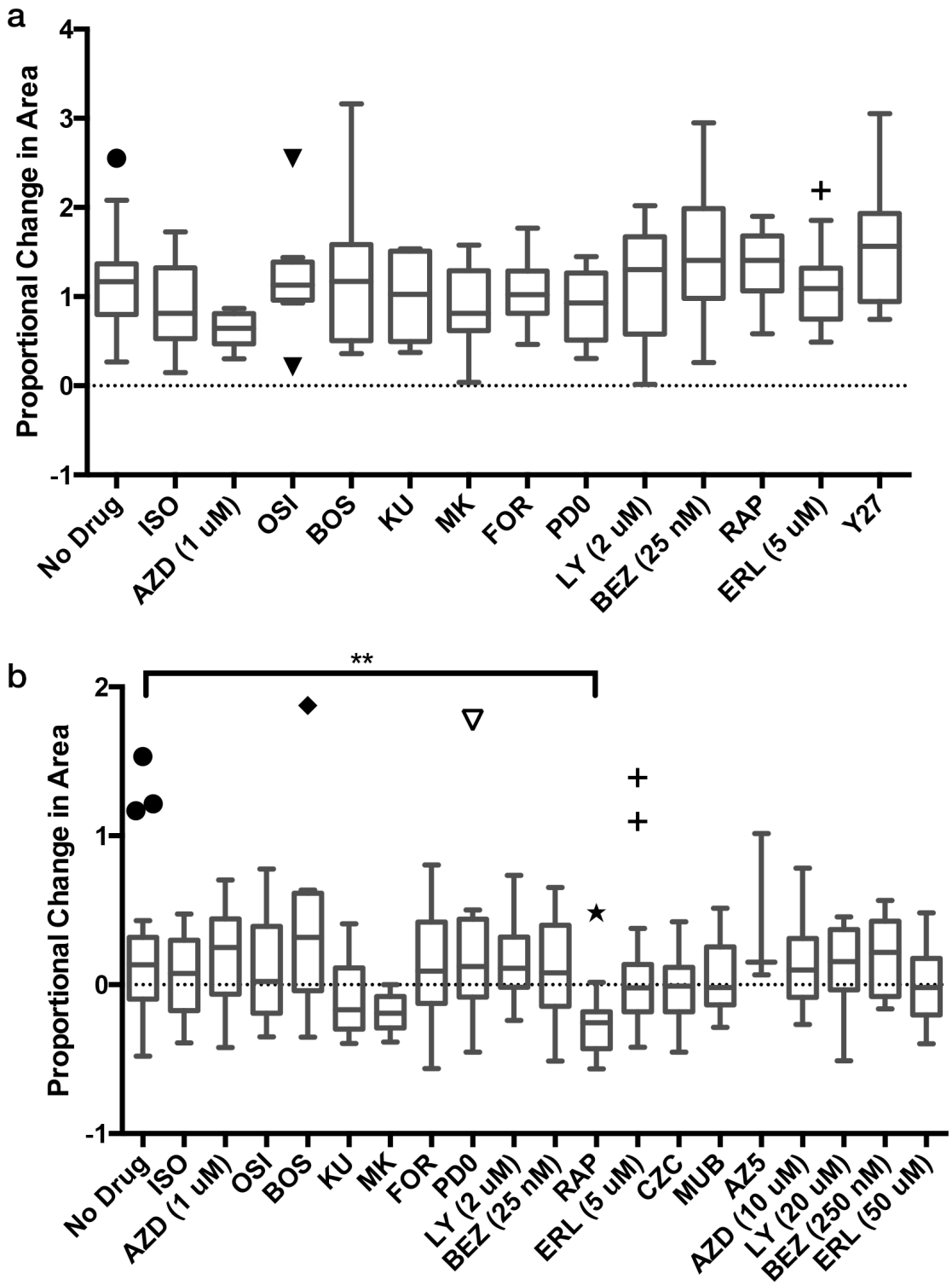

Figure 44. Proportional change in spheroid bounding box area after exposure to inhibitors. Samples without dcEF shown for (a) DAOY and (b) U87mg cells for the period 244 to 48h after exposure to inhibitor. First 2 or 3 letters of inhibitor compound are used as labels. **p=0.0039

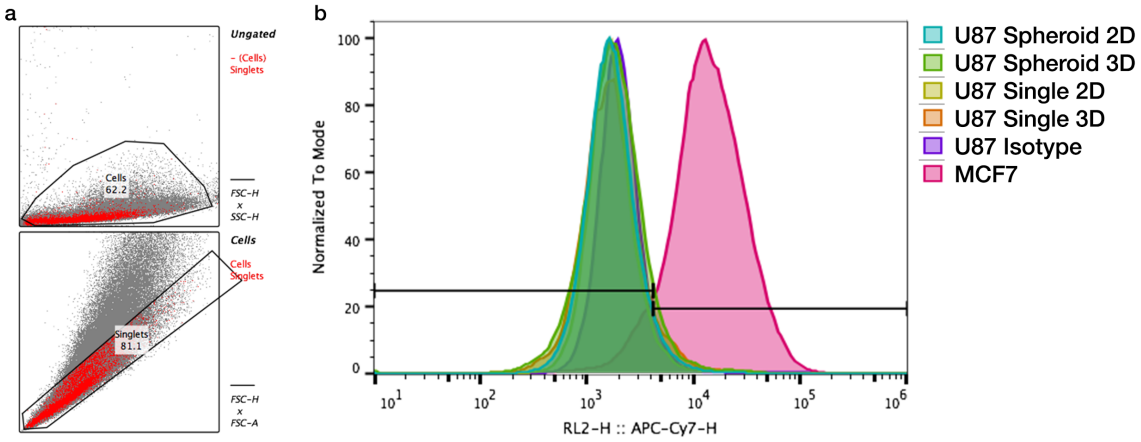

Figure 45. Flow cytometry data for ErbB2 expression for different plating confirmations of U87mg cells. U87mg cells were plated onto either 2D culture plastic or embedded in 3D matrigel as either single, dispersed cells, or as spheroidal aggregates. After 24h culture in those conditions, disassociated cells were stained for CD340 (ErbB2 marker) with APC/Fire 750 conjugated antibodies. (a) Gate history showing selection of cells and singlets. (b) Histogram of APC/Fire 750 intensity. ErbB2+ MCF7 cells serve as positive control.

REFERENCES

Adamczyk, L. A., Williams, H., Frankow, A., Ellis, H. P., Haynes, H. R., Perks, C., Holly, J. M. P. & Kurian, K. M. (2015). Current understanding of circulating tumor cells–potential value in malignancies of the central nervous system. *Frontiers in neurology*, *6*.

Anand, M., Van Meter, T. E., & Fillmore, H. L. (2011). Epidermal growth factor induces matrix metalloproteinase-1 (MMP-1) expression and invasion in glioma cell lines via the MAPK pathway. *Journal of neuro-oncology*, *104*(3), 679-687.

Babona-Pilipos, R., Pritchard-Oh, A., Popovic, M. R., & Morshead, C. M. (2015). Biphasic monopolar electrical stimulation induces rapid and directed galvanotaxis in adult subependymal neural precursors. *Stem cell research & therapy*, *6*(1), 67.

Bai, H., Forrester, J. V., & Zhao, M. (2011). DC electric stimulation upregulates angiogenic factors in endothelial cells through activation of VEGF receptors. *Cytokine*, *55*(1), 110-115.

Bellail, A. C., Hunter, S. B., Brat, D. J., Tan, C., & Van Meir, E. G. (2004). Microregional extracellular matrix heterogeneity in brain modulates glioma cell invasion. *The international journal of biochemistry & cell biology*, *36*(6), 1046-1069.

Bernstein, J. J., & Woodard, C. A. (1995). Glioblastoma cells do not intravasate into blood vessels. *Neurosurgery*, *36*(1), 124-132.

Blakeley, J. (2008). Drug delivery to brain tumors. *Current neurology and neuroscience reports*, *8*(3), 235-241.

Bray, N. L., Pimentel, H., Melsted, P., & Pachter, L. (2016). Near-optimal probabilistic RNA-seq quantification. *Nature biotechnology*, *34*(5), 525.

Brennan, P. J., Kumogai, T., Berezov, A., Ramachandran, M., & Greene, M. I. (2000). HER2/Neu: mechanisms of dimerization/oligomerization. *Oncogene*, 19(53), 6093-6101.

Borgens, R. B., Roederer, E., & Cohen, M. J. (1981). Enhanced spinal cord regeneration in lamprey by applied electric fields. *Science*, *213*(4508), 611-617.

Cardinal, J., Klune, J. R., Chory, E., Jeyabalan, G., Kanzius, J. S., Nalesnik, M., & Geller, D. A. (2008). Noninvasive radiofrequency ablation of cancer targeted by gold nanoparticles. *Surgery*, *144*(2), 125-132.

Carrasco-García, E., Saceda, M., Grasso, S., Rocamora-Reverte, L., Conde, M., Gómez-Martínez, A., García-Morales, P., Ferragut, J. A., & Martínez-Lacaci, I. (2011). Small tyrosine kinase inhbitors interrupt EGFR signaling by interacting with erbB3 and erbB4 in glioblastoma cell lines. *Experimental cell research*, 317(10), 1476-1489.

Chernet, B., & Levin, M. (2013). Endogenous voltage potentials and the microenvironment: bioelectric signals that reveal, induce and normalize cancer. *Journal of clinical & experimental oncology*.

Cohen, D. J., Nelson, W. J., & Maharbiz, M. M. (2014). Galvanotactic control of collective cell migration in epithelial monolayers. *Nature materials*, *13*(4), 409-417.

Coniglio, S. J., Zavarella, S., & Symons, M. H. (2008). Pak1 and Pak2 mediate tumor cell invasion through distinct signaling mechanisms. *Molecular and cellular biology*, *28*(12), 4162-4172.

Cortese, B., Palamà, I. E., D'Amone, S., & Gigli, G. (2014). Influence of electrotaxis on cell behaviour. *Integrative Biology*,*6*(9), 817-830.

Crawford, J. R., MacDonald, T. J., & Packer, R. J. (2007). Medulloblastoma in childhood: new biological advances. *The Lancet Neurology*, *6*(12), 1073-1085.

Cross, D. A., Ashton, S. E., Ghiorghiu, S., Eberlein, C., Nebhan, C. A., Spitzler, P. J., Orme, J. P., Finlay, M. R. V., Ward, R. A., Mellor, M. J. & Hughes, G. (2014). AZD9291, an irreversible EGFR TKI, overcomes T790M-mediated resistance to EGFR inhibitors in lung cancer. *Cancer discovery*, *4*(9), 1046-1061.

Cukjati, D., Batiuskaite, D., André, F., Miklavčič, D., & Mir, L. M. (2007). Real time electroporation control for accurate and safe in vivo non-viral gene therapy. *Bioelectrochemistry*, *70*(2), 501-507.

Davalos, R. V., Mir, L. M., & Rubinsky, B. (2005). Tissue ablation with irreversible electroporation. *Annals of biomedical engineering*, *33*(2), 223-231.

Del Fabbro, C., Scalabrin, S., Morgante, M., & Giorgi, F. M. (2013). An extensive evaluation of read trimming effects on Illumina NGS data analysis. *PloS one*, *8*(12), e85024.

Djamgoz, M. B., Mycielska, M., Madeja, Z., Fraser, S. P., & Korohoda, W. (2001). Directional movement of rat prostate cancer cells in direct-current electric field. *Journal of cell science*, *114*(14), 2697-2705.

Etienne-Manneville, S., & Hall, A. (2003). Cdc42 regulates GSK-3beta and adenomatous polyposis coli to control cell polarity. *Nature*, *421*(6924), 753.

Fan, Q. W., Cheng, C., Hackett, C., Feldman, M., Houseman, B. T., Nicolaides, T., ... & Shokat, K. M. (2010). Akt and autophagy cooperate to promote survival of drug-resistant glioma. *Science signaling*, *3*(147), ra81.

Fan, Q. W., Cheng, C. K., Nicolaides, T. P., Hackett, C. S., Knight, Z. A., Shokat, K. M., & Weiss, W. A. (2007). A dual phosphoinositide-3-kinase α/mTOR inhibitor cooperates with blockade of epidermal growth factor receptor in PTEN-mutant glioma. *Cancer research*, *67*(17), 7960-7965.

Faria, C. C., Golbourn, B. J., Dubuc, A. M., Remke, M., Diaz, R. J., Agnihotri, S., Luck, A., Sabha, N., Olsen, S., Wu, X. & Garzia, L. (2014). Foretinib is effective therapy for metastatic sonic hedgehog medulloblastoma. *Cancer research*.

Fraser, S. P., Diss, J. K., Chioni, A. M., Mycielska, M. E., Pan, H., Yamaci, R. F., Pani, F., Siwy, Z., Krasowska, M., Grzywna, Z. & Brackenbury, W. J. (2005). Voltage-gated sodium channel

expression and potentiation of human breast cancer metastasis. *Clinical Cancer Research*, *11*(15), 5381-5389.

Friedl, P., & Gilmour, D. (2009). Collective cell migration in morphogenesis, regeneration and cancer. *Nature reviews Molecular cell biology*, *10*(7), 445-457.

Funk, R. H., & Monsees, T. K. (2006). Effects of electromagnetic fields on cells: physiological and therapeutical approaches and molecular mechanisms of interaction. *Cells Tissues Organs*,*182*(2), 59-78.

Gao, R., Zhao, S., Jiang, X., Sun, Y., Zhao, S., Gao, J., Borleis, J., Willard, S., Tang, M. Cai, H. & Kamimura, Y. (2015). A large scale screen reveals genes that mediate electrotaxis in Dictyostelium discoideum. *Science signaling*, *8*(378), ra50.

Gehl, J. (2003). Electroporation: theory and methods, perspectives for drug delivery, gene therapy and research. *Acta Physiologica*, *177*(4), 437-447.

Gothelf, A., Mir, L. M., & Gehl, J. (2003). Electrochemotherapy: results of cancer treatment using enhanced delivery of bleomycin by electroporation. *Cancer treatment reviews*, *29*(5), 371-387.

Greuber, E. K., Smith-Pearson, P., Wang, J., & Pendergast, A. M. (2013). Role of ABL family kinases in cancer: from leukaemia to solid tumours. *Nature Reviews Cancer*, *13*(8), 559-571.

Han, X., Zhang, W., Yang, X., Wheeler, C. G., Langford, C. P., Wu, L., Filippova, N., Friedman, G. K., Ding, Q., Fathallah-Shaykh, H. M. & Gillespie, G. Y. (2014). The role of Src family kinases in growth and migration of glioma stem cells. *International journal of oncology*, *45*(1), 302-310.

Hansen, K. D., Brenner, S. E., & Dudoit, S. (2010). Biases in Illumina transcriptome sequencing caused by random hexamer priming. *Nucleic acids research*, *38*(12), e131-e131.

Harrow, J., Frankish, A., Gonzalez, J. M., Tapanari, E., Diekhans, M., Kokocinski, F., Aken, B. L., Barrell, D., Zadissa, A., Searle, S. & Barnes, I. (2012). GENCODE: the reference human genome annotation for The ENCODE Project. *Genome research*, *22*(9), 1760-1774.

Hart, F. X., Laird, M., Riding, A., & Pullar, C. E. (2013). Keratinocyte galvanotaxis in combined DC and AC electric fields supports an electromechanical transduction sensing mechanism. *Bioelectromagnetics*, *34*(2), 85-94.

Hart, F. X., & Palisano, J. R. (2017). Glycocalyx bending by an electric field increases cell motility. *Bioelectromagnetics*.

Hickinson, D. M., Klinowska, T., Speake, G., Vincent, J., Trigwell, C., Anderton, J., Beck, S., Marshall, G., Davenport, S., Callis, R. & Mills, E. (2010). AZD8931, an equipotent, reversible inhibitor of signaling by epidermal growth factor receptor, ERBB2 (HER2), and ERBB3: a unique agent for simultaneous ERBB receptor blockade in cancer. *Clinical Cancer Research*, *16*(4), 1159-1169.

Howlader, N., Noone, A.M., Krapcho, M., Miller, D., Bishop, K., Kosary, C. L., Yu, M., Ruhl, J., Tatalovich, Z., Mariotto, A., Lewis, D. R., Chen, H. S., Feuer, E. J., Cronin, K.A. (2016) NCI

SEER Cancer Statistics Review, 1975-2014. https://seer.cancer.gov/csr/1975_2014/, based on November 2016 SEER data submission, posted to the SEER web site, September 2017.

Huang, C. W., Cheng, J. Y., Yen, M. H., & Young, T. H. (2009). Electrotaxis of lung cancer cells in a multiple-electric-field chip. *Biosensors and Bioelectronics*, *24*(12), 3510-3516.

Huang, Y. J., Hoffmann, G., Wheeler, B., Schiapparelli, P., Quinones-Hinojosa, A., & Searson, P. (2016). Cellular microenvironment modulates the galvanotaxis of brain tumor initiating cells. *Scientific reports*, *6*.

Ishizawar, R. C., Miyake, T., & Parsons, S. J. (2007). c-Src modulates ErbB2 and ErbB3 heterocomplex formation and function. *Oncogene*, *26*(24), 3503.

Jain, A., Betancur, M., Patel, G. D., Valmikinathan, C. M., Mukhatyar, V. J., Vakharia, A., Pai, S. B., Brahma, B., MacDonald, T. J. & Bellamkonda, R. V. (2014). Guiding intracortical brain tumour cells to an extracortical cytotoxic hydrogel using aligned polymeric nanofibres. *Nature materials*,*13*(3), 308.

Jin, R., Nakada, M., Teng, L., Furuta, T., Sabit, H., Hayashi, Y., Demuth, T., Hirao, A., Sato, H., Zhao, G. & Hamada, J. I. (2013). Combination therapy using Notch and Akt inhibitors is effective for suppressing invasion but not proliferation in glioma cells. *Neuroscience letters*, *534*, 316-321.

Kanehisa, M., & Goto, S. (2000). KEGG: kyoto encyclopedia of genes and genomes. *Nucleic acids research*, *28*(1), 27-30.

Khanna, V., Achey, R. L., Ostrom, Q. T., Block-Beach, H., Kruchko, C., Barnholtz-Sloan, J. S., & de Blank, P. M. (2017). Incidence and survival trends for medulloblastomas in the United States from 2001 to 2013. *Journal of Neuro-Oncology*, 1-9.

Kirson, E. D., Dbalý, V., Tovaryš, F., Vymazal, J., Soustiel, J. F., Itzhaki, A., Mordechovich, D., Steinberg-Shapira, S., Gurvich, Z., Schneiderman, R. & Wasserman, Y. (2007). Alternating electric fields arrest cell proliferation in animal tumor models and human brain tumors. *Proceedings of the National Academy of Sciences*,*104*(24), 10152-10157.

Kranich, S., Hattermann, K., Specht, A., Lucius, R., & Mentlein, R. (2009). VEGFR-3/Flt-4 mediates proliferation and chemotaxis in glial precursor cells. *Neurochemistry international*, *55*(8), 747-753.

Kreth, S., Heyn, J., Grau, S., Kretzschmar, H. A., Egensperger, R., & Kreth, F. W. (2010). Identification of valid endogenous control genes for determining gene expression in human glioma. *Neuro-oncology*, *12*(6), 570-579.

Lalli, M. L., & Asthagiri, A. R. (2015). Collective migration exhibits greater sensitivity but slower dynamics of alignment to applied electric fields. *Cellular and molecular bioengineering*, *8*(2), 247-257.

Lang, F., & Shumilina, E. (2013). Regulation of ion channels by the serum-and glucocorticoid-inducible kinase SGK1. *The FASEB Journal*, *27*(1), 3-12.

Li, F., Chen, T., Hu, S., Lin, J., Hu, R., & Feng, H. (2013). Superoxide mediates direct current electric field-induced directional migration of glioma cells through the activation of AKT and ERK. *PLoS One*, *8*(4), e61195.

Li, L., El-Hayek, Y. H., Liu, B., Chen, Y., Gomez, E., Wu, X., Ning, K., Li, L., Chang, N., Zhang, L. & Wang, Z. (2008). Direct-Current Electrical Field Guides Neuronal Stem/Progenitor Cell Migration. *Stem cells*, *26*(8), 2193-2200.

Li, Y., Wang, X., & Yao, L. (2015). Directional migration and transcriptional analysis of oligodendrocyte precursors subjected to stimulation of electrical signal. *American Journal of Physiology-Cell Physiology*, *309*(8), C532-C540.

Lin, B. J., Tsao, S. H., Chen, A., Hu, S. K., Chao, L., & Chao, P. H. G. (2017). Lipid rafts sense and direct electric field-induced migration. *Proceedings of the National Academy of Sciences*,*114*(32), 8568-8573.

Liu, Q., & Song, B. (2014). Electric field regulated signaling pathways. *The international journal of biochemistry & cell biology*,*55*, 264-268.

Liu, T. J., Koul, D., LaFortune, T., Tiao, N., Shen, R. J., Maira, S. M., Garcia-Echevrria, C. & Yung, W. A. (2009). NVP-BEZ235, a novel dual phosphatidylinositol 3-kinase/mammalian target of rapamycin inhibitor, elicits multifaceted antitumor activities in human gliomas. *Molecular cancer therapeutics*, *8*(8), 2204-2210.

MacManes, M. D. (2014). On the optimal trimming of high-throughput mRNA sequence data. *Frontiers in Genetics*, *5*.

Mali, B., Jarm, T., Snoj, M., Sersa, G., & Miklavcic, D. (2013). Antitumor effectiveness of electrochemotherapy: a systematic review and meta-analysis. *European Journal of Surgical Oncology (EJSO)*, *39*(1), 4-16.

Marjanovič, I. & Miklavčič, D. (2011) Elektroporacija. *Življenje in tehnika*. 62(7): 34-43.

McCaig, C. D., Song, B., & Rajnicek, A. M. (2009). Electrical dimensions in cell science. *Journal of cell science*, *122*(23), 4267-4276.

Merrill, D. R., Bikson, M., & Jefferys, J. G. (2005). Electrical stimulation of excitable tissue: design of efficacious and safe protocols. *Journal of neuroscience methods*, *141*(2), 171-198.

Mili, S., Moissoglu, K., & Macara, I. G. (2008). Genome-wide screen reveals APC-associated RNAs enriched in cell protrusions. *Nature*, *453*(7191), 115-119.

Mineo, J. F., Bordron, A., Quintin-Roue, I., Loisel, S., Ster, K. L., Buhe, V., Lagarde, N. & Berthou, C. (2004). Recombinant humanised anti-HER2/neu antibody (Herceptin®) induces cellular death of glioblastomas. *British journal of cancer*, *91*(6), 1195.

Mulvihill, M. J., Cooke, A., Rosenfeld-Franklin, M., Buck, E., Foreman, K., Landfair, D., O'Connor, M., Pirritt, C., Sun, Y., Yao, Y. & Arnold, L. D. (2009). Discovery of OSI-906: a selective and orally efficacious dual inhibitor of the IGF-1 receptor and insulin receptor. *Future medicinal chemistry*,*1*(6), 1153-1171.

Mycielska, M. E., & Djamgoz, M. B. (2004). Cellular mechanisms of direct-current electric field effects: galvanotaxis and metastatic disease. *Journal of cell science*, *117*(9), 1631-1639.

Nabors, L. B., Portnow, J., Ammirati, M., Baehring, J., Brem, H., Brown, P., Butowski, N., Chamberlain, M. C., Fenstermaker, R. A., Friedman, A. & Gilbert, M. R. (2015). Central nervous system cancers, version 1.2015. *Journal of the National Comprehensive Cancer Network*, *13*(10), 1191-1202.

Meng, X., Arocena, M., Penninger, J., Gage, F. H., Zhao, M., & Song, B. (2011). PI3K mediated electrotaxis of embryonic and adult neural progenitor cells in the presence of growth factors. *Experimental neurology*, *227*(1), 210-217.

Nagashima, T., Shimodaira, H., Ide, K., Nakakuki, T., Tani, Y., Takahashi, K., Yumoto, N. & Hatakeyama, M. (2007). Quantitative transcriptional control of ErbB receptor signaling undergoes graded to biphasic response for cell differentiation. *Journal of biological chemistry*, *282*(6), 4045-4056.

Nakajima, K. I., Zhu, K., Sun, Y. H., Hegyi, B., Zeng, Q., Murphy, C. J., Small, J. V., Chen-Izu, Y., Izumiya, Y., Penninger, J. M. & Zhao, M. (2015). KCNJ15/Kir4. 2 couples with polyamines to sense weak extracellular electric fields in galvanotaxis. *Nature communications*, *6*, 8532.

Nayak, L., Lee, E. Q., & Wen, P. Y. (2012). Epidemiology of brain metastases. *Current oncology reports*, *14*(1), 48-54.

Nuccitelli, R., Pliquett, U., Chen, X., Ford, W., Swanson, R. J., Beebe, S. J., Kolb, J. F. & Schoenbach, K. H. (2006). Nanosecond pulsed electric fields cause melanomas to self-destruct. *Biochemical and biophysical research communications*, *343*(2), 351-360.

Nuccitelli, R. (2011). Measuring endogenous electric fields. *The Physiology of Bioelectricity in Development, Tissue Regeneration and Cancer*, *1*, 1-16.

O'Brien, K., Matlin, A. J., Lowell, A. M., & Moore, M. J. (2008). The biflavonoid isoginkgetin is a general inhibitor of Pre-mRNA splicing. *Journal of Biological Chemistry*, *283*(48), 33147-33154.

Ostrom, Q. T., Gittleman, H., Farah, P., Ondracek, A., Chen, Y., Wolinsky, Y., Stroup, N. E., Kruchko, C. & Barnholtz-Sloan, J. S. (2013). CBTRUS statistical report: Primary brain and central nervous system tumors diagnosed in the United States in 2006-2010. *Neuro-oncology*,*15*(suppl_2), ii1-ii56.

Özkucur, N., Perike, S., Sharma, P., & Funk, R. H. (2011). Persistent directional cell migration requires ion transport proteins as direction sensors and membrane potential differences in order to maintain directedness. *BMC cell biology*, *12*(1), 4.

Park, H. J., Rouabhia, M., Lavertu, D., & Zhang, Z. (2015). Electrical stimulation modulates the expression of multiple wound healing genes in primary human dermal fibroblasts. *Tissue Engineering Part A*, *21*(13-14), 1982-1990.

Pickl, M., & Ries, C. H. (2009). Comparison of 3D and 2D tumor models reveals enhanced HER2 activation in 3D associated with an increased response to trastuzumab. *oncogene*, *28*(3), 461.

Piddock, R. E., Loughran, N., Marlein, C. R., Robinson, S. D., Edwards, D. R., Yu, S., Pillinger, G. E., Zhou, Z., Zaitseva, L., Auger, M. J. & Rushworth, S. A. (2017). PI3Kδ and PI3Kγ isoforms have distinct functions in regulating pro-tumoural signalling in the multiple myeloma microenvironment. *Blood cancer journal*, *7*(3), e539.

Pimentel, H., Bray, N. L., Puente, S., Melsted, P., & Pachter, L. (2017). Differential analysis of RNA-seq incorporating quantification uncertainty. *Nature methods*.

Pu, J., McCaig, C. D., Cao, L., Zhao, Z., Segall, J. E., & Zhao, M. (2007). EGF receptor signalling is essential for electric-field-directed migration of breast cancer cells. *Journal of cell science*,*120*(19), 3395-3403.

Pullar, C. E., Baier, B. S., Kariya, Y., Russell, A. J., Horst, B. A., Marinkovich, M. P., & Isseroff, R. R. (2006). β4 integrin and epidermal growth factor coordinately regulate electric field-mediated directional migration via Rac1. *Molecular biology of the cell*, *17*(11), 4925-4935.

Pullar, C. E., & Isseroff, R. R. (2005). Cyclic AMP mediates keratinocyte directional migration in an electric field. *Journal of cell science*, *118*(9), 2023-2034.

Rajnicek, A. M., Foubister, L. E., & McCaig, C. D. (2006). Temporally and spatially coordinated roles for Rho, Rac, Cdc42 and their effectors in growth cone guidance by a physiological electric field. *Journal of Cell Science*, *119*(9), 1723-1735.

Reimand, J., Arak, T., Adler, P., Kolberg, L., Reisberg, S., Peterson, H., & Vilo, J. (2016). g: Profiler—a web server for functional interpretation of gene lists (2016 update). *Nucleic acids research*, *44*(W1), W83-W89.

Ricard, D., Idbaih, A., Ducray, F., Lahutte, M., Hoang-Xuan, K., & Delattre, J. Y. (2012). Primary brain tumours in adults. *The Lancet*,*379*(9830), 1984-1996.

Riding, A., & Pullar, C. E. (2016). ATP Release and P2Y receptor signaling are essential for keratinocyte galvanotaxis. *Journal of cellular physiology*, *231*(1), 181-191.

Rossi, S., Di Stasi, M., Buscarini, E., Quaretti, P., Garbagnati, F., Squassante, L., Paties, C. T., Silverman, D. E. & Buscarini, L. (1996). Percutaneous RF interstitial thermal ablation in the treatment of hepatic cancer.*AJR. American journal of roentgenology*, *167*(3), 759-768.

Sauer, H., Stanelle, R., Hescheler, J., & Wartenberg, M. (2002). The DC electrical-field-induced Ca2+ response and growth stimulation of multicellular tumor spheroids are mediated by ATP release and purinergic receptor stimulation. *Journal of Cell Science*, *115*(16), 3265-3273.

See, W. L., Tan, I. L., Mukherjee, J., Nicolaides, T., & Pieper, R. O. (2012). Sensitivity of glioblastomas to clinically available MEK inhibitors is defined by neurofibromin 1 deficiency. *Cancer research*, *72*(13), 3350-3359.

Seiden-Long, I. M., Brown, K. R., Shih, W., Wigle, D. A., Radulovich, N., Jurisica, I., & Tsao, M. S. (2006). Transcriptional targets of hepatocyte growth factor signaling and Ki-ras oncogene activation in colorectal cancer. *Oncogene*, *25*(1), 91.

Shestakova, E. A., Singer, R. H., & Condeelis, J. (2001). The physiological significance of β-actin mRNA localization in determining cell polarity and directional motility. *Proceedings of the National Academy of Sciences*, *98*(13), 7045-7050.

Shi, Q., Song, X., Wang, J., Gu, J., Zhang, W., Hu, J., Zhou, X. & Yu, R. (2015). FRK inhibits migration and invasion of human glioma cells by promoting N-cadherin/β-catenin complex formation. *Journal of molecular neuroscience*, *55*(1), 32-41.

Shields IV, C. W., Reyes, C. D., & López, G. P. (2015). Microfluidic cell sorting: a review of the advances in the separation of cells from debulking to rare cell isolation. *Lab on a Chip*, *15*(5), 1230-1249.

Song, B., Zhao, M., Forrester, J., & McCaig, C. (2004). Nerve regeneration and wound healing are stimulated and directed by an endogenous electrical field in vivo. *Journal of Cell Science*,*117*(20), 4681-4690.

Song, B., Gu, Y., Pu, J., Reid, B., Zhao, Z., & Zhao, M. (2007). Application of direct current electric fields to cells and tissues in vitro and modulation of wound electric field in vivo. *Nature protocols*, *2*(6), 1479.

Stupp, R., Wong, E. T., Kanner, A. A., Steinberg, D., Engelhard, H., Heidecke, V., Kirson, E. D., Taillibert, S., Liebermann, F., Dbalý, V. & Ram, Z. (2012). NovoTTF-100A versus physician's choice chemotherapy in recurrent glioblastoma: a randomised phase III trial of a novel treatment modality. *European journal of cancer*, *48*(14), 2192-2202.

Stupp, R., Taillibert, S., Kanner, A. A., Kesari, S., Steinberg, D. M., Toms, S. A., Taylor, L. P., Lieberman, F., Silvani, A., Fink, K. L. & Barnett, G. H. (2015). Maintenance therapy with tumor-treating fields plus temozolomide vs temozolomide alone for glioblastoma: a randomized clinical trial. *Jama*, *314*(23), 2535-2543.

Stupp, R., Hegi, M. E., Idbaih, A., Steinberg, D. M., Lhermitte, B., Read, W., Toms, S. A., Barnett, G. H., Nicholas, G., Kim, C. Y., Fink, K. Salmaggi, A., Lieberman, F. S., Zhu, J. J., Taylor, L., Stragliotto, G., Hottinger, A. F., Kirson, E. D., Weinberg, U., Palti, Y. & Ram, Z. (2017). Tumor treating fields added to standard chemotherapy in new diagnosed glioblastoma (GBM): Final results of a randomized, multi-center, phase III trial. *AACR Annual Meeting.*

Subramanian, A., Tamayo, P., Mootha, V. K., Mukherjee, S., Ebert, B. L., Gillette, M. A., Paulovich, A., Pomeroy, S. L., Golub, T. R. & Mesirov, J. P. (2005). Gene set enrichment analysis: a knowledge-based approach for interpreting genome-wide expression profiles. *Proceedings of the National Academy of Sciences*, *102*(43), 15545-15550.

Takeuchi, H., Kondo, Y., Fujiwara, K., Kanzawa, T., Aoki, H., Mills, G. B., & Kondo, S. (2005). Synergistic augmentation of rapamycin-induced autophagy in malignant glioma cells by phosphatidylinositol 3-kinase/protein kinase B inhibitors. *Cancer research*, *65*(8), 3336-3346.

Tsai, H. F., Huang, C. W., Chang, H. F., Chen, J. J., Lee, C. H., & Cheng, J. Y. (2013). Evaluation of EGFR and RTK signaling in the electrotaxis of lung adenocarcinoma cells under direct-current electric field stimulation. *PLoS One*, *8*(8), e73418.

Ufkin, M. L., Peterson, S., Yang, X., Driscoll, H., Duarte, C., & Sathyanarayana, P. (2014). miR-125a regulates cell cycle, proliferation, and apoptosis by targeting the ErbB pathway in acute myeloid leukemia. *Leukemia research*, *38*(3), 402-410.

Vinci, M., Box, C., & Eccles, S. A. (2015). Three-dimensional (3D) tumor spheroid invasion assay. *Journal of visualized experiments: JoVE*, (99).

Vultur, A., Buettner, R., Kowolik, C., Liang, W., Smith, D., Boschelli, F., & Jove, R. (2008). SKI-606 (bosutinib), a novel Src kinase inhibitor, suppresses migration and invasion of human breast cancer cells. *Molecular Cancer Therapeutics*, *7*(5), 1185-1194.

Wiesner, S. M., Freese, A., & Ohlfest, J. R. (2005). Emerging concepts in glioma biology: implications for clinical protocols and rational treatment strategies. *Neurosurgical focus*, *19*(4), 1-6.

Wu, D., Ma, X., & Lin, F. (2013). DC electric fields direct breast cancer cell migration, induce EGFR polarization, and increase the intracellular level of calcium ions. *Cell biochemistry and biophysics*, *67*(3), 1115-1125.

Yan, X., Han, J., Zhang, Z., Wang, J., Cheng, Q., Gao, K., Ni, Y. & Wang, Y. (2009). Lung cancer A549 cells migrate directionally in DC electric fields with polarized and activated EGFRs. *Bioelectromagnetics*, *30*(1), 29-35.

Yao, L., Li, Y., Knapp, J., & Smith, P. (2015). Exploration of molecular pathways mediating electric field-directed schwann cell migration by RNA-seq. *Journal of cellular physiology*, *230*(7), 1515-1524.

Yildirim, S., Altun, S., Gumushan, H., Patel, A., & Djamgoz, M. B. (2012). Voltage-gated sodium channel activity promotes prostate cancer metastasis in vivo. *Cancer letters*, *323*(1), 58-61.

Zhang, J., Calafiore, M., Zeng, Q., Zhang, X., Huang, Y., Li, R. A., Deng, W. & Zhao, M. (2011). Electrically guiding migration of human induced pluripotent stem cells. *Stem Cell Reviews and Reports*,*7*(4), 987-996.

Zhao, M., Pu, J., Forrester, J. V., & McCaig, C. D. (2002). Membrane lipids, EGF receptors, and intracellular signals colocalize and are polarized in epithelial cells moving directionally in a physiological electric field. *The FASEB Journal*, *16*(8), 857-859.

Zhao, M., Song, B., Pu, J., Wada, T., Reid, B., Tai, G., ... & Sasaki, T. (2006). Electrical signals control wound healing through phosphatidylinositol-3-OH kinase-[gamma] and PTEN. *Nature*,*442*(7101), 457.

Zhao, S., Gao, R., Devreotes, P. N., Mogilner, A., & Zhao, M. (2013). 3D arrays for high throughput assay of cell migration and electrotaxis. *Cell biology international*, *37*(9), 995-1002.